Electrodeposition and Characterisation of Thin Films and Nanostructures based on Bismuth, Silver and Iodine

by

Craig Alexander Jeffrey
B.Sc., University of Guelph

A Dissertation Submitted in Partial Fulfillment of the
Requirements for the Degree of
DOCTOR OF PHILOSOPHY
in the
Department of Chemistry.

University of Victoria

Supervisor: Dr. David A. Harrington

Abstract

Electrodeposition is used to produce thin film and nanostructured materials based on bismuth, silver and iodine. X-ray and probe microscopy techniques are employed to determine the structure of electrodeposited Bi films on Au(111) substrates. Analyses of multilayer films reveal that they are deposited epitaxially, with the Bi(012) plane parallel to the underlying Au(111) surface, and require no annealing to achieve single-crystal domains. The bulk film/substrate structure has been modelled and compared with in situ Scanning Tunneling Microscopy (STM) images of the growing epitaxial films. Models of the multilayer arrangement provide structural evidence for the proposed anisotropic growth mode.

Electrodeposition of silver and copper on iodine-covered and bare polycrystalline Pt electrodes is studied with the Electrochemical Quartz-Crystal Microbalance (EQCM). Voltammetry of silver on the iodine-covered surface shows single deposition and stripping peaks, with masses appropriate for silver. This is an ideal calibration system. A lower mass than the ideal silver mass for multilayer silver electrodeposition (in the absence of iodine) is attributed to increased smoothing of the electrode.

The EQCM and a Rotating Ring-Disk Electrode (RRDE) are used to study the behaviour of iodate interactions at Pt polycrystalline electrodes. Comparison of results between 0.2 and 1 mM iodate solutions point to significant contributions from solution-based reactions throughout the formation and dissolution of the iodine adlayer. Direct reduction from the iodate anion appears to be responsible for the formation of the adlayer.

Electrodeposition of silver iodide films and layered structures is investigated using coreduction of silver and iodate ions in a single bath onto platinum EQCM electrodes. Iodate concentration is shown to significantly affect the rate of film formation and plays a crucial role in determining film thickness. High relative concentrations of IO_3^-

result in significant solution-based charge transfer reactions that complicate analysis of the film structure using the microbalance. A simple model based on the EQCM response is employed to determine the structure of films formed in these solutions at more negative potentials. These films exhibit an AgI_x ($x < 1$) structure. A pulsed potential scheme is employed to create a layered material of the form AgI_x/AgI_y.

Table of Contents

List of Tables

List of Figures

Nomenclature

Symbol	Meaning	Units
a_{hex}, b_{hex}, c_{hex}	Hexagonal lattice unit cell lengths	m
a_{rh}, b_{rh}, c_{rh}	Rhombohedral lattice unit cell lengths	m
C_{f}	EQCM calibration factor	Hz ng^{-1} cm^2
E	Potential	V
E°	Standard potential	V
E_{bias}	STM tip bias potential	mV
E_{disk}	Rotating disk potential	V
E_{ring}	Rotating ring potential	V
f	Frequency	Hz
f°	Resonant frequency	MHz
f_{RRDE}	Rotating ring-disk rotation rate	RPM
G	Gibbs energy	kJ mol^{-1}
h, k, l	Miller indices	
I_{t}	STM tunneling current	nA
j	Current density	μA cm^{-2}
j_{Disk}	Rotating disk current density	μA cm^{-2}
j_{Ring}	Rotating ring current density	μA cm^{-2}
K_{sp}	Solubility product	

Symbol	Meaning	Units
m	Mass	g
n	Harmonic number of oscillation	
θ	Bragg angle	degrees
μ	Shear modulus	g cm^{-1} s^{-2}
ν	Sweep rate	V s^{-1}
ρ	Density	g cm^{-3}
σ_{Total}	Total charge density	μC cm^{-2}
φ	Azimuthal angle	degrees
χ	Tilt angle	degrees
ω	Rocking angle	degrees

Acknowledgements

First and foremost, I would like to thank my supervisor Dr. David Harrington. It has been an extremely rewarding experience to work in his research group. I thank him for his careful guidance, his enthusiasm, for pushing me to produce the best work that I could and for never seeming to get frustrated with the number of times I knocked on his office door. I will miss working through and discussing results at the blackboard in there and I will take away a great deal from my time at UVic. Thanks as well to Dr. Sylvie Morin, who was an enthusiastic co-supervisor for a large part of the work presented here. All of the experimental data in this dissertation pertaining to bismuth was acquired as part of a collaboration with her research group at York University. I very much enjoyed working with her and with her group.

I'd like to thank group members past and present: Miguel Labayen for helping me along, especially at the beginning, and Frode Seland, Jean-Marc Le Canut and Ruth Latham for interesting discussions along the way. Thanks also to 499 students Wendy Storr and Toby Astill who worked on projects related to the work presented in this dissertation, it was a great experience working with them.

For financial support throughout my graduate studies I'd like to thank the Natural Sciences and Engineering Research Council (NSERC) and the University of Victoria for the award of postgraduate scholarships.

Thanks to Dr. Jay Switzer and Dr. Eric Bohannan at the University of Missouri - Rolla, Center for Graduate Studies in Materials for providing the X-ray data presented and analysed in this dissertation.

Thanks to all the faculty members in the department. There is a real sense of community in the Chemistry department at UVic and it's very inspiring to a young researcher. Thanks especially to my committee members here at the University; my interactions and discussions with all of them have been very helpful.

The staff in the department and around the University have taken care of so much, which has allowed me to focus primarily on research and learning. Thanks

to the stores staff: Bev Scheurle, Troy Hasanen and Rob Iuvale. Thanks to Bob Dean for his help with the inevitable instrument and computer crises we encounter in our lab. Thanks to Sean Adams in the glass shop and Doug Stajduhar and Dick Robinson in the machine shop for all of their help and ideas. Thanks to the department secretaries: Carol Jenkins, Susanne Reiser, Shelley Henuset, Rosemary Pulez and Sandra Harris for keeping everything running smoothly. Thanks to Dave Berry, Alan Taylor and Monica Reimer for all of the teaching experiences I've gained through TA'ing. Thanks also to Carolyn Swayze and Jodi Lewis and the rest of the Graduate Studies staff who have always been great to deal with.

I've made many friends in the department along the way so thanks to every one of those people. Matt, Tamara, Gwen and Mike, thanks for all the fun times up to this point and here's to more down the road. Thanks also to everyone in the Ell 240 office *circa.* 1999 - 2003. Thanks to Ed, Mike, Jeff, Stone, Matt, Jack and Dave, for providing the best soundtrack I could imagine for the last 13 years.

For j and for my Mom and Dad. Thanks so much to each of you for everything.

Chapter 1

Introduction

This dissertation examines electrodeposition of nanostructured materials. Nanotechnology has received a great deal of attention in the scientific community due to both a fundamental interest in one end of the size spectrum and the potential for significant technological application and advancement. The work presented here focuses on understanding some fundamental properties of electrodeposited thin films. This dissertation also explores the use of interesting methods of characterisation of these materials and provides a careful examination of the strengths and weaknesses of one particular technique: the Electrochemical Quartz-Crystal Microbalance (EQCM). The dissertation has two larger sections, each containing separate chapters. Each chapter contains an introduction outlining the relevant literature pertaining to the details of the chapter. A general overview is provided here.

The first section pertains to studies of the electrodeposition of bismuth. Chapter 3 employs *in situ* Scanning Tunneling Microscopy (STM) to study both underpotentially deposited films of Bi on Au(111) and multilayer structures. The first atomic layer of Bi deposited is shown to affect the surface reconstruction of the gold surface. The multilayer deposition process is captured in a series of images and reveals the interesting growth mode of Bi needle structures on the surface. The study details

the process of growing well-ordered Bi films and probes this order using atomic resolution images. The results presented in this chapter have been published in *Surface Science* [1].

Chapter 4 delves more deeply into understanding these Bi thin films. X-ray pole figure analysis is utilised to model the structure and epitaxial arrangement of the electrodeposited bismuth on the gold substrate. An overview of the modelling process is outlined in Appendix A. The models provide a detailed picture of the film structure and evidence for a proposed growth mode.

The second section of the dissertation examines the electrochemical production of thin films of silver and iodide characterised with the EQCM. Chapter 5 examines the electrodeposition of silver onto bare and iodine-covered Pt electrodes. Coating the electrodes with iodine proves to be an excellent calibration method for the EQCM. The iodine adlayer acts to promote layer-by-layer growth in favour of three-dimensional growth. The iodine layer also maintains a constant interaction with electrolyte molecules in the presence or absence of silver. This greatly simplifies the analysis of silver deposition using the EQCM. With the instrument calibrated, the response in the absence of the iodine layer is examined and the marked deviations from ideal behaviour are explained in terms of surface smoothing accompanying film deposition. The results presented in this chapter were published in the *Journal of Electroanalytical Chemistry* [2].

Chapter 6 examines the behaviour of the halogen component of the electrodeposited films. This study of iodate electrochemistry on Pt electrodes reveals a mixture of surface- and solution-based processes. This mixture of processes complicates the analysis by EQCM and the implications are demonstrated and discussed. On a fundamental level the work shows an interesting relationship between the iodate adlayer and physisorbed solution species. These interactions would be difficult to discern using traditional electrochemical techniques alone.

Finally, Chapter 7 utilises information from both of the preceding chapters to examine the production of silver iodide films on the Pt surface. The study shows that films with a structure of AgI_x ($x < 1$) can be deposited over a wide range of potential and the relative amount of iodide incorporation can be varied. The application of a pulsed potential sequence is used to exploit this behaviour to produce layered materials of the form AgI_x/AgI_y in a single electrochemical bath. The work represents an unique application of the EQCM to monitor these potentiostatically-formed structures.

Chapter 2

Experimental Methods

2.1 Bismuth electrodeposition

2.1.1 Electrochemistry and *in situ* Scanning Tunneling Microscopy (STM)

All STM data reported in this dissertation were obtained by the author while working in the laboratory of Dr. Sylvie Morin at York University. Dr. Morin also served in a supervisory role for all of the work presented in this dissertation pertaining to studies of Bi electrodeposition.

Cyclic voltammetry data were obtained with an Autolab electrochemical analyser (PGSTAT30, Eco Chemie BV) using a three-electrode glass cell deoxygenated with argon. 1×10^{-3} M Bi^{3+} solutions used for *in situ* STM experiments and cyclic voltammetry were prepared by dissolving Bi_2O_3 (99.9995%) in 0.1 M $HClO_4$.

Perchloric acid electrolytes were prepared from suprapure $HClO_4$ and Milli-Q water. Gold (111) single crystals were purchased from Monocrystal Co. with a $\pm$ 3° miscut. The crystals were realigned along the (111) plane to $\pm$ 0.5° using Laue X-ray backscattering. This was followed by polishing with diamond paste down to 0.25 μm

and further electropolishing using electrooxidation in 0.1 M $HClO_4$ [3]. The gold electrode was flame annealed prior to each experiment [4]. Deposition experiments were performed with the STM tip in tunneling contact, with the tip bias (E_{bias}) usually kept 50-80 mV more positive than the sample potential. All electrode potentials, E, in Chapters 3 and 4 were controlled and are reported versus a saturated calomel electrode (SCE). The reference was housed in a separate compartment that was in electrical contact with the solution in the electrochemical cell. The cell used in the STM consisted of a metal base plate and a removable Teflon reservoir for the solution. The working electrode (Au(111) crystal) was situated on the base plate atop a thin insulating layer. The Teflon piece was secured on top of the crystal and formed a seal that allowed for the electrolyte to be introduced. The exposed geometric area of the working electrode was $\simeq 0.385$ cm^2. The cell accommodated an electrolyte volume of $\simeq 300$ μL. The counter electrode in the cell was a platinum wire curved around the inner circumference. The microscope was housed in a acoustically-isolated box and was suspended by cables to minimise vibrational effects. Experiments were performed at room temperature that was generally $22.0 \pm 0.5°$. STM images were acquired using a Molecular Imaging Picoscan STM equipped with a bipotentiostat (Picostat) to control the sample and tip potentials. Images were produced in constant-current mode (see I_t, tunneling current, listed in figure captions in Chapter 3) and are presented as top view images with brighter tones representing higher surface features.

2.1.2 X-ray characterisation

X-ray data on the electrodeposited Bi films were provided by Dr. Eric Bohannan at the Center for Graduate Studies in Materials, University of Missouri - Rolla. All analyses of the data were performed by the author.

X-ray diffraction (XRD) data were obtained using a Scintag 2000 diffractometer with Cu Kα radiation. Azimuthal and tilt scans (used to create x-ray pole figures)

were obtained through the attachment of a texture goniometer accessory for the Scintag diffractometer.

Theoretical bismuth and gold lattice structures and surfaces were modelled using the MAPLE software package (Version 9.00, Waterloo Maple Inc.). Fundamental crystallographic data were taken from data compiled by Wyckoff [5].

2.2 Electrochemical Quartz-Crystal Microbalance (EQCM) electrodeposition studies

2.2.1 Physical setup and data acquisition

EQCM experiments were carried out using a glass electrochemical cell fitted with a Teflon quartz crystal holder similar to the design of Jerkiewicz [6]. Both the electrode holder and the cell were designed and fabricated as part of the microbalance studies outlined in this dissertation. A schematic of the electrode housing is shown in Fig. 2.1.

The 9 MHz crystals were purchased from Princeton Applied Research and had platinum pads (0.5 cm diameter, geometric area = 0.196 cm^2) deposited onto a thin titanium layer on unpolished quartz substrates. A phase-locked oscillator (Maxtek PLO-10i) drove the oscillation of the crystal. Shifts in the resonant frequency of the crystal were recorded with a high-resolution programmable frequency counter (Fluke PM6681). All frequency data presented were obtained with a 20 ms gate time and have not been smoothed or filtered beyond the averaging inherent to the gate time. Experimental data were obtained using conventional analog instrumentation and were digitized with a 12-bit analog to digital converter (Pico Technologies ADC-212). A block diagram of the EQCM setup is given in Fig. 2.2.

Electrochemical and experimental data were gathered using an in-house program

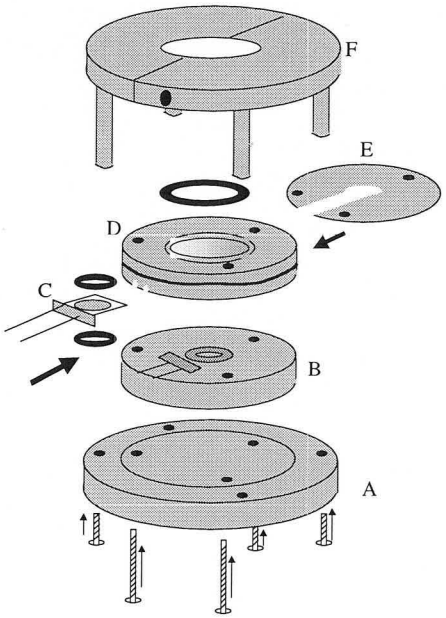

Figure 2.1: Schematic of the EQCM Teflon cell. a) Metal backing piece. b) Base Teflon piece. c) Quartz crystal and surrounding Viton o-rings. d) Teflon piece with solution port and Viton o-ring for seal with glass cell. e) Metal anchor piece that slides into 'd'. f) Two-piece metal post arrangement for attachment to the glass cell. Scale: radii of a and f = 2.5 cm. Assembled cell height is 3.5 cm.

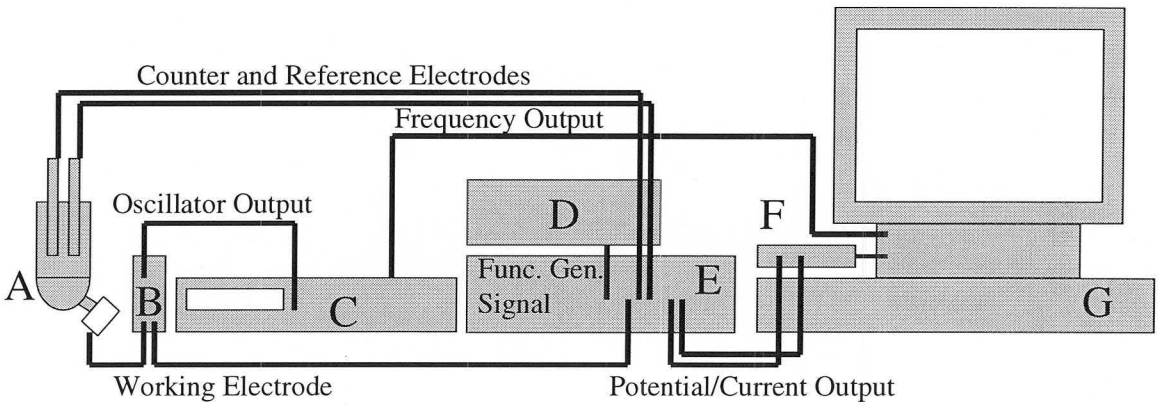

Figure 2.2: Basic layout and connection scheme for the EQCM set up. a) Electrochemical and EQCM cell. b) Oscillator circuit. c) Frequency counter. d) Function generator (sweep and/or arbitrary waveform generator). e) Potentiostat. f) Picoscope oscilloscope. g) Data acquisition computer.

('Acquire') written in Visual Basic by Dr. David Harrington. A module was written by the author to interface the EQCM with the acquisition program as part of this work.

2.2.2 Electrochemistry

All EQCM experiments were carried out at room temperature. Chemicals were analytical grade and used as received from Alfa Aesar (silver and copper perchlorates), Fisher (potassium iodate) and BDH (potassium iodide and perchloric acid). The quartz crystals were dipped in dilute nitric acid, rinsed with Millipore Milli-Q water and dried in an argon stream prior to the experiments. All potentials for the EQCM work (chapters 5, 6 and 7) were measured relative to a hydrogen electrode in the same solution (RHE). Electrolytes were purged of oxygen prior to and during experiments by passing a stream of argon through the solution. Platinum gauze was used as the counter electrode. All experiments began with only perchloric acid present in the cell. The potential was cycled between 0.04 and 1.60 V at 100 mV s^{-1} until the voltammogram and frequency response possessed only the features characteristic of clean polycrystalline platinum (Fig. 2.3). The roughness factors (actual area/projected area) of the electrodes used in this work were in the range $1.06 - 1.80$. The electrochemically-active area was estimated from the charge under the hydrogen adsorption peaks in base electrolyte (assuming 220 μC cm^{-2} for the ideal smooth surface), and was used to calculate the quoted current and charge densities. Although argon bubbling continued in the solution during EQCM measurements, there was no noticeable change in the current response with the gas outlet in or out of the solution due to its proximity to the working electrode. For this reason, convection due to this bubbling was considered to be absent and in all cases in the dissertation the solution was treated as effectively unstirred.

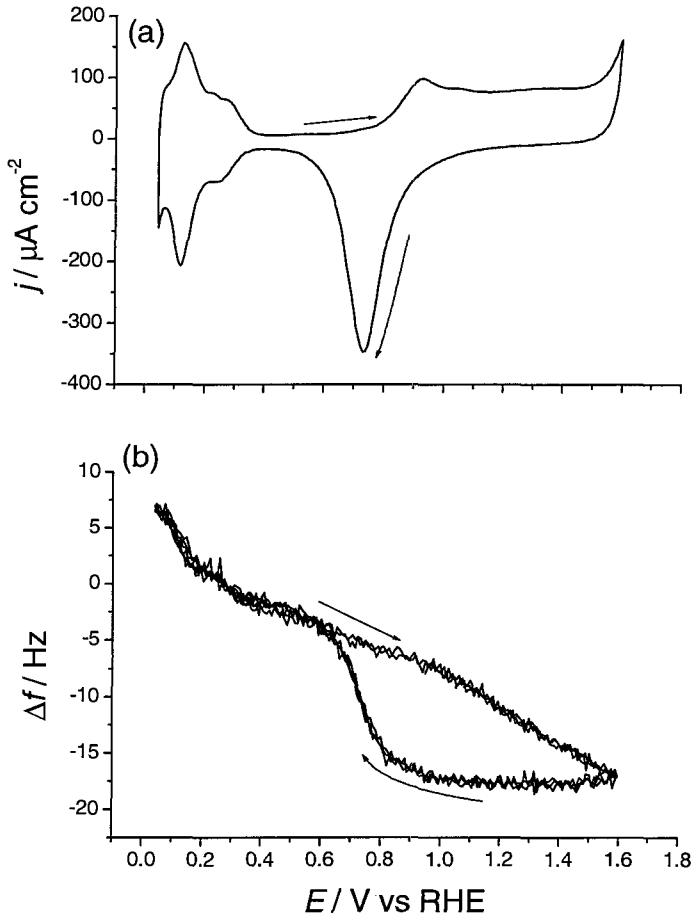

Figure 2.3: EQCM response in acidic electrolyte. a) Cyclic voltammogram of EQCM Pt electrode in 0.5 M $HClO_4$. Sweep rate 100 mV s^{-1}. b) Frequency change of electrode over 3 consecutive cycles.

2.2.3 Pretreatment of EQCM electrodes with iodine

For experiments involving iodine-covered surfaces (Chapter 5), the initial perchloric acid was removed and replaced with a small amount of KI dissolved in perchloric acid. This solution was then removed and the cell was rinsed with water. The open circuit potential (OCP, approximately 0.80 V) of the working electrode was monitored prior to reestablishing the cell potential via the potentiostat. A potential equal to the OCP was then applied to the cell while monitoring both the cell current and frequency response. No significant change in the frequency occurred during this step, indicating that the iodine layer on the surface was undisturbed. Aliquots of either silver or copper perchlorate in 0.5 M perchloric acid were introduced into the cell to bring the overall metal ion concentration to 1 mM.

2.2.4 Frequency analysis

The shift in the resonant frequency of an EQCM electrode accompanying a change in mass per unit surface area is governed by the well-known Sauerbrey equation [7],

$$\Delta f = -2f_0^2 \Delta m / n(\rho\mu)^{1/2} \text{ or } \Delta f = -C_f \Delta m \tag{2.1}$$

where f_0 is the resonant frequency ($\approx$ 9 MHz in air for all crystals used here), n is the harmonic number of the oscillation (1), ρ is the density of quartz (2.648 g cm^{-3}), and μ is the shear modulus of quartz (2.947×10^{11} g cm^{-1} s^{-2}). The C_f factor simply groups together the constants related to the crystal itself. This equation holds only under certain conditions such as the assumption that the mass gain occurs precisely at the interface between the crystal and the solution. This assumption has been determined to be reasonable if the resonant frequency shifts by no more than 2% of the fundamental [8]. This condition is easily met in most metal thin film deposition systems, and all frequency changes reported in this dissertation are well below this

limit. The calibration factor C_f was determined from silver deposition data on iodine-covered Pt. This calibration method is discussed in detail in Chapter 5. The value of C_f used for all mass determinations in the dissertation was 0.188 Hz ng^{-1} cm^2. A significant sweep rate dependence was not observed. Nevertheless, all mass determinations from cyclic voltammetry using the EQCM have been acquired at a consistent sweep rate (ν) of 0.020 V s^{-1} to minimise any possible errors. Mass/charge ratios were determined by plotting the change in frequency (Δf) vs. the change in charge density ($\Delta\sigma$) for a given process. All 'mass' values derived from EQCM data (quoted in g mol^{-1}) in the dissertation should be understood to refer to 'grams per mol of electrons'.

2.2.5 EQCM data treatment/fitting

Chapter 5, metal electrodeposition on bare and iodine-covered electrodes

The data analysis for assigning mass/charge ratios to peaks in the cyclic voltammograms (CVs) involved fitting the region corresponding to 50 points on either side of the peak in the CV (101 points fit, potential window of approximately 0.170 V). This was adhered to except for those cases where this number of points interfered with other features in the CV. In these cases, the number of points was reduced symmetrically about the peak point by as little as possible to avoid the response from neighbouring features.

Chapter 6, iodate electrochemistry

There existed considerable overlap between features in the CVs presented in this chapter. For this reason the data analysis method used to determine the mass/charge ratios for given features involved fitting the regions of constant slope in the frequency vs. charge density plots. The complete frequency vs. charge density traces have

been presented in all cases with the regions used for fitting emphasised. The lowest number of consecutive points fit for any mass/charge ratio presented was 36, while most fitting was done on sets of 70 points or higher.

Chapter 7, silver iodide films and superlattice structures

The number of data points used to determine the slope of the frequency vs. charge density traces varied depending on the type of experiment performed (CV or chronoamperometry) and are discussed in the main text.

Double layer charging

Charge densities are generally presented with no double layer charge correction. The presence of an adsorbate at the electrode interface can have a significant impact on the double layer capacitance. The majority of charge transfer processes in this work are of far greater magnitude than those that would be expected from double layer charging. In most cases the raw data are presented instead of making corrections of questionable significance. Double layer charging in the calibration system is discussed in more detail in Chapter 5. Additionally, the specific case of double layer charge correction for superlattice structure determination (Chapter 7) is discussed within the text.

2.2.6 EQCM measurement error

Where error estimates are provided in the main text, the data were obtained from several different electrodes in replicate experiments and are quoted as a 95% confidence level. In the case of Ag deposition on bare Pt (used for determination of the C_f value), the errors were determined from the standard deviations of seven replicate measurements. Where error estimates are not explicitly given (often for traces used

for comparison or that are part of a larger data set for different conditions), it is assumed that the measurement error is below 12%, the largest deviation that was observed in the calibration studies.

2.3 Rotating Ring-Disk Electrode (RRDE) studies

RRDE studies were carried out using a Pine AFMT28 electrode composed of a platinum disk and platinum ring. The electrode dimensions are: Disk outer diameter = 0.1800", ring inner diameter = 0.1940", ring outer diameter = 0.2120" and a shroud diameter of 0.531". These dimensions result in a nominal collection efficiency at the ring of 22.0 %. Prior to all experiments, both the disk and ring electrodes on the RRDE were cycled between 0.040 and 1.60 V in 0.5 M $HClO_4$ until the traces for both electrodes possessed the features of clean polycrystalline platinum. Potentials at the disk and ring were controlled independently vs. RHE using a Pine bipotentiostat.

Chapter 3

Bi electrodeposition

3.1 Introduction

This chapter examines the electrodeposition of bismuth thin films on Au(111) and provides details about the growth characteristics. Bismuth and oxides of bismuth have been well studied due to their interesting physical properties, including the very large magnetoresistance effects found in bismuth films [9–12] and their use in electrochromic devices [13]. The semiconductor aspects of the oxides of bismuth (the δ-phase of which possesses the highest known ion mobility for oxide structures [14]) has also attracted attention [15]. Additionally, bismuth has been utilised as a component in compound semiconducting electrodeposited materials such as $Bi_{1-x}Sb_x$ [16, 17] and BiTe [18].

The atomic structures of Bi UPD phases formed at well-defined surfaces have been determined using *in situ* STM, Atomic Force Microscopy (AFM) and x-ray diffraction [19–21]. While these investigations have concentrated on the structures of the different Bi UPD phases, other studies used various electrochemical methods to evaluate Bi coverage and characterise this adsorption process [22–27]. These studies have characterised irreversible Bi adsorption on Pt electrodes [28, 29] and its effect on

various electrooxidation [30–33] and electroreduction processes [19, 21, 34] at Pt and Au [35] electrodes. The effect of the presence of Bi on metal UPD [36] and the effects of anion adsorption [37] on the Bi adsorption were also studied. However, the growth mechanism of Bi during bulk deposition is little understood. Ziegler [13] investigated the morphology of Bi (and Bi-Cu) electrodeposition and dissolution at highly ordered pyrolytic graphite using *in situ* STM. The resulting Bi films appeared rough, while addition of Cu to the plating solution yielded smoother films [13].

This chapter presents an *in situ* STM study of Bi electrodeposition on Au(111) for both the underpotential deposition (UPD) and overpotential deposition (OPD) regions. It is observed that the adsorption of UPD bismuth leads to the formation of gold islands on the Au(111) terraces due to the lifting of the gold surface reconstruction. This process is observed well into the UPD region at potentials $E < 0.170$ V_{SCE}. Although it is known that many adsorbates are capable of lifting the gold reconstruction, these observations indicate that this process requires the larger Bi coverage reached only after the second UPD peak. In the overpotential region, STM images show that the initial and multilayer Bi deposits are anisotropic and follow a needle-like growth. This growth behavior is unusual given that the underlying gold surface is three-fold symmetric. Using *in situ* STM, the Bi surface unit cell has been determined and a growth mechanism for the needles is proposed. The results also indicate that the potential scheme applied to grow these films has a significant bearing on the overall surface morphology.

3.2 Underpotential deposition (UPD)

According to cyclic voltammogram (CV) experiments, shown in Fig. 3.1, the onset of Bi UPD on the gold (111) surface is observed near 0.350 V (see Fig. 3.1a). As the potential is swept to more negative values a broad peak with some fine features is visible around 0.190 V and a larger peak is observed at 0.170 V (c1). Another broad

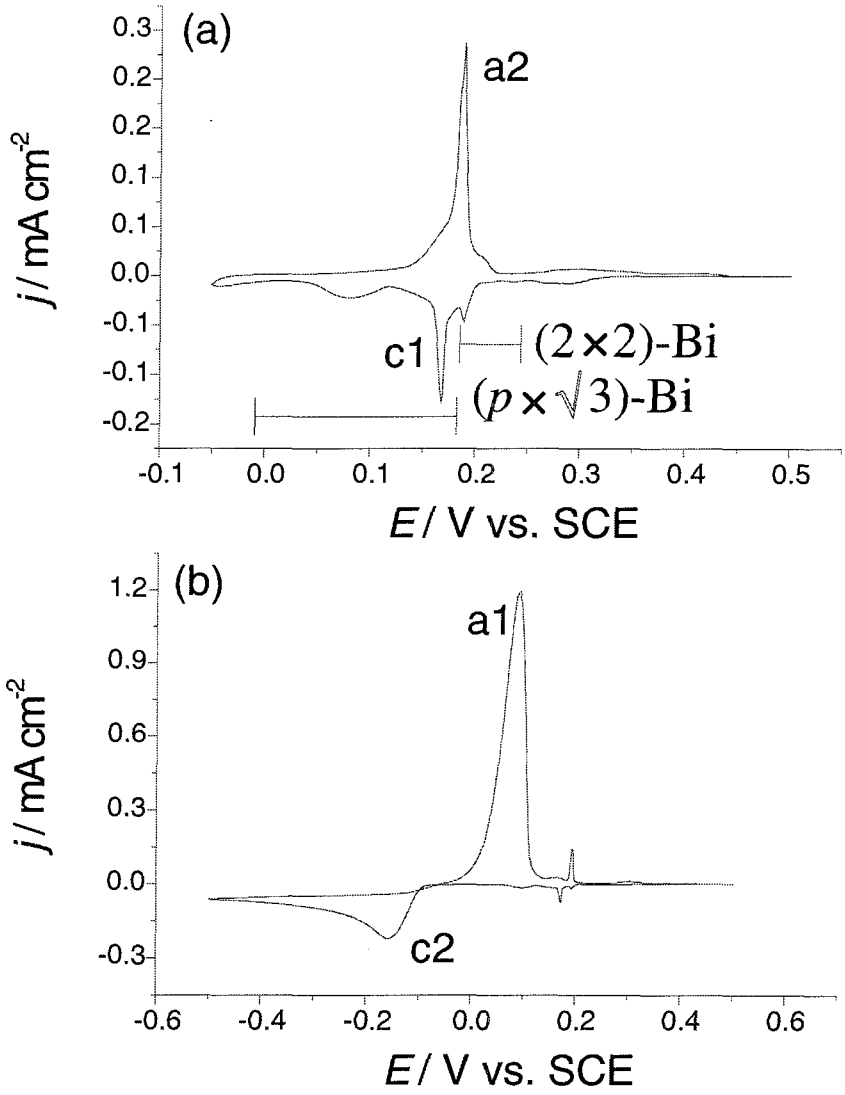

Figure 3.1: Bismuth electrochemistry on Au(111). a) Cyclic voltammetry restricted to the UPD region (1 mM Bi^{3+}, 0.1 M $HClO_4$, $\nu = 0.020$ V s^{-1}). UPD structures given as per ref. [20]. b) Bulk deposition and dissolution in the same solution ($\nu = 0.010$ V s^{-1}).

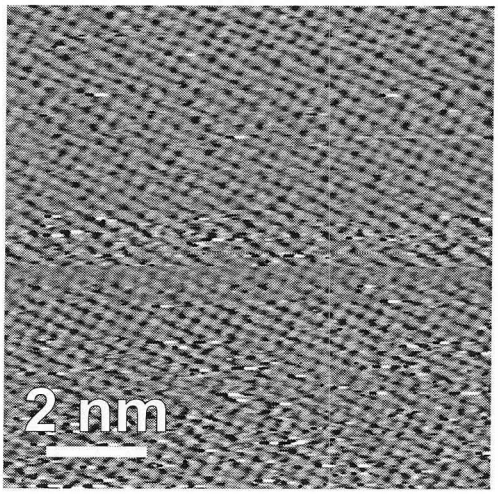

Figure 3.2: 10 nm × 10 nm image of UPD rectangular $(p \times \sqrt{3})$-2Bi phase. E = -0.050 V, E_{bias} = +0.080 V, I_{t} = 1.7 nA.

peak is also visible at 0.080 V. Using *in situ* STM, the Bi UPD atomic structure was resolved at -0.050 V. At this potential, a Moiré structure is observed, due to a uniaxial mismatch of the Bi UPD layer with the underlying hexagonal gold surface. In a direction perpendicular to the modulation rows the Bi-Bi spacing is 4.0 ± 0.2 Å (Fig. 3.2). This value is smaller than the one reported in Ref. [19]. However, smaller Bi-Bi spacings were also observed by surface X-ray scattering (SXS) when the potential was lowered from $\simeq$ 0.180 to 0 V [20]. The atomic spacing in the primitive unit cell for this Bi phase is 3.2 ± 0.2 Å, in agreement with previous AFM and STM studies [19, 20]. Using SXS, this phase of the Bi UPD was more accurately assigned to a $(p \times \sqrt{3})$-Bi phase [19,21]. Two more Bi phases are observed at potentials above $\simeq$ 0.180 V; at low coverage a disordered adlayer exists, and as the coverage increases a (2×2)-Bi commensurate structure forms [19–21]. In this work, bulk Bi nucleation occurs on top of the $(p \times \sqrt{3})$-Bi phase.

In this study of the Bi electrodeposition, the Au(111) surface was always covered by the electrolyte while under potential control. The initial potential for all experiments was around 0.350 ± 0.050 V, i.e. near the onset of Bi UPD. In this region of

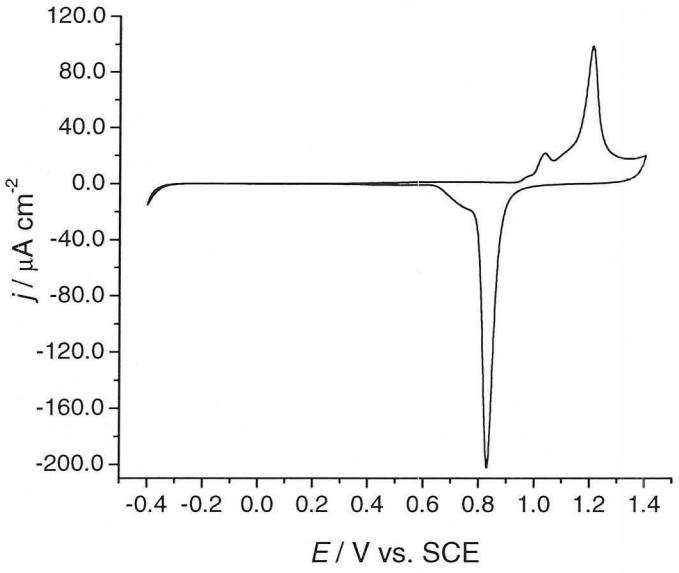

Figure 3.3: Electrochemistry of Au(111) in electrolyte alone. $HClO_4$ concentration = 0.1 M, $\nu = 0.020$ V s^{-1}.

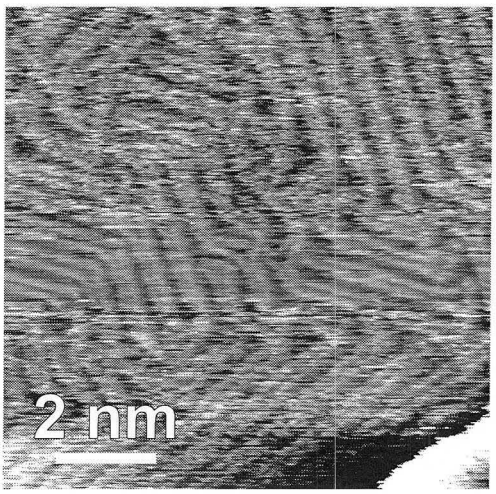

Figure 3.4: 10 nm × 10 nm image of the reconstructed Au(111) surface demonstrating the 'herringbone' structure. Lighter areas represent atoms slightly dislocated out of the surface. E = -0.200 V. Electrolyte was 0.1 mM H_2SO_4 + 10 mM Na_2SO_4.

potential the Au(111) surface reconstruction produced by the flame annealing is not lifted and a $(22 \times \sqrt{3})$ phase is present (no gold islands are formed on the terraces at this potential). It is well known that in acidic electrolyte alone, the Au(111)(1×1) surface transforms to a $(22 \times \sqrt{3})$ phase with a 4% compression at potentials below $\simeq$ 0.240 mV and that the reverse transition occurs for potentials above $\simeq$ 0.440 V in $HClO_4$ solutions [38]. A CV of the Au(111) electrode in perchloric acid alone is shown in Fig. 3.3. The surface reconstruction produces the so-called 'herringbone' pattern to alleviate surface stress. An STM image of this pattern is shown in Fig. 3.4. During a slow sweep from 0.300 V toward lower potential values in a solution containing bismuth, the Au(111) terraces become covered by small gold islands at potential values around 0.170 ± 0.020 V (Fig. 3.5). These islands are 2.6 Å high and are visible at all potentials negative of the second UPD peak ($E < 0.170$ V). The presence of these islands is consistent with moving the excess Au atoms from their locations in the $(22 \times \sqrt{3})$ phase to the Au surface when the 4% compression is removed (see caption, Fig. 3.5). The excess gold atoms from these islands can become incorporated into the nearby step edges, resulting in an island exclusion zone close to the step edges (also observed in Fig. 3.5). It is suggested that the significant change in Bi coverage over the second UPD peak ($E = 0.170$ V, see Fig. 3.1a) is sufficient to cause the lifting of the Au reconstruction. The lifting of the reconstruction is not expected to occur in this range of potential in the Bi free solution. It is difficult to assess from these observations if the lifting of the reconstruction is due solely to the presence of the fully or partially discharged adsorbates. Similar issues are discussed in detail in Ref [39].

3.3 Overpotential deposition (OPD)

Significant bulk Bi deposition starts at –0.075 V, 0.070 V more negative than the Nernst reversible potential (c2). Bulk bismuth deposition is reversible, i.e. all the

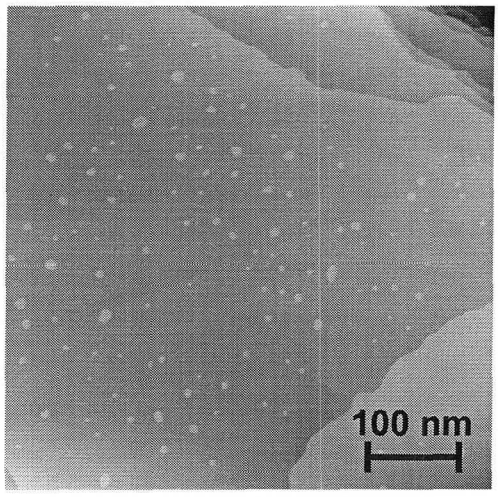

Figure 3.5: 500 nm × 500 nm STM image of gold island formation (in the presence of the $(p \times \sqrt{3})$-2Bi phase) observed at E = -0.060 V (E_{bias} = +0.080 V, I_{t} = 0.6 nA); island heights are 2.6 Å. The island coverage measured on several terraces varied from 3.2 - 3.7% and is consistent with the $\simeq$ 4% of the surface Au atoms being removed during the lifting of the Au reconstruction (the percentage of island coverage in this image is 3.2%).

electrodeposited Bi is removed from the surface in a single potential sweep (Fig. 3.1b). When studied using *in situ* STM, the OPD region of bismuth on gold shows very interesting growth behaviour. Fig. 3.6 displays a series of STM images obtained during the *in situ* growth of several Bi layers on Au(111). Fig. 3.6a was obtained at -0.040 V after applying a potential step from –0.040 V to –0.120 V for 4 seconds. At the former potential, the Bi deposited during the pulse (at –0.120 V) began to dissolve and only residual Bi was observed along the gold step edges (see black arrows in Fig. 3.6a).

An additional 4s pulse to –0.120 V was applied, and the final potential was set at –0.070 V; this allowed slow Bi growth so that STM images could capture images of the dynamic film growth. This decrease from –0.040 V to –0.070 V for the acquisition of the image prevented Bi redissolution. The image in Fig. 3.6b shows Bi needle growth along step edges in regions where the step density is high. This anisotropic growth

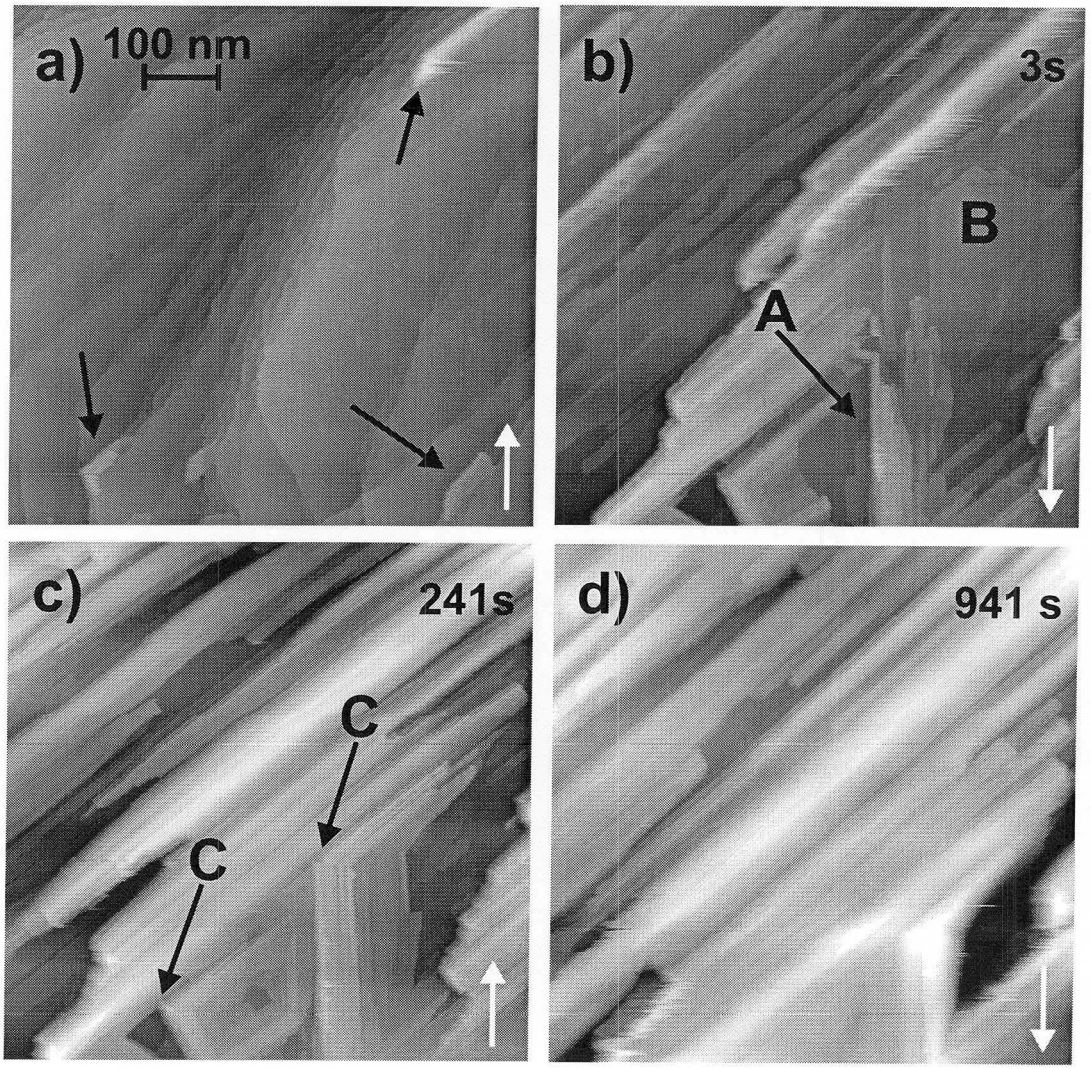

Figure 3.6: Deposition of Bi on Au(111) captured over 941 s using in situ STM. All images are 700 nm × 700 nm. Scan direction indicated by white arrows. a) Au(111) covered by Bi UPD and Bi islands at step edges after an initial 4 s pulse to -0.120 V (image recorded at -0.040 V). b) Initiated growth of Bi film after a second 4 s pulse to -0.120 V applied (image recorded at -0.070 V). Number of layers in this image varies widely due to the stage of growth (1 layer $\simeq 3.5 \pm 0.2$ Å). c) continued Bi film growth (image recorded at -0.070 V, average number of layers $\simeq$ 17). d) Lateral growth of the Bi film (image recorded at -0.070 V, average number of layers $\simeq$ 50). ($E_{\text{bias}} =$ +80 mV, $I_{\text{t}} = 0.398$ nA for all images, height (z) scale for images a) and b) is 100 Å, 150 Å for c) and 200 Å for d)).

is sustained during the initial deposition stages. In areas where the step density is moderate (A in Fig. 3.6b), the needle structures nucleate at the low portion of the step edges, grow perpendicular to step edges and proceed across the next lower terrace. These structures easily change direction when they encounter the next terrace edge or an area where the growth direction is already determined (see areas marked as C Fig. 3.6c). During the early stages of deposition, it is clear that deposition onto larger terraces can also lead to wide monatomic-height areas ca. 3.5 Å tall (B in Fig. 3.6b). These surfaces are free from nucleated islands, suggesting a slower nucleation rate on the Bi covered terraces. The difference in morphology between the large monatomic islands and the Bi needles also suggests that the transport of Bi atoms across the terrace is limited or that the structure of the two features is slightly different, one of which favours the anisotropic needle growth.

Because growth was relatively slow at –0.070 V, a good estimation of the Bi coverage can be made (see caption Fig. 3.6). Fig. 3.6b and c show that further Bi growth proceeds laterally resulting in a relatively uniform film (Fig. 3.6d). Image (d) shows the gold surface covered with bismuth, where the general direction of the surface features still corresponds to the growth direction of the bismuth needles in Fig. 3.6b. Films deposited through the application of cathodic pulses always demonstrated the growth characteristics described in Fig. 3.6, and they appeared smooth, bright and metallic gray in colour. The needle morphology of the film is regular and strikingly similar to the structures observed on macroscopic samples of bismuth. However, a very different surface morphology was observed when the potential was slowly swept cathodically into the OPD region. In this case, the growth was initially slow, followed by faster 3-D growth that created an amorphous film. These films appeared dull and uneven upon visual inspection.

Further understanding of the growth behaviour can be obtained from atomic resolution images of the Bi needle structures for various scan sizes (Fig. 3.7a-c). Note that height maxima (i.e., electron density maxima) associated with Bi atoms are vis-

ible in all of the images presented in Fig. 3.7. In Fig. 3.7b, a nearly rectangular unit cell is visible (vectors 1 and 2 each span five unit cell lengths) with an angle of 85 ± 2° between the vectors. This figure also reveals that the spacing between the atoms is 4.3 ± 0.2 Å along the width (vector 2) of the needle and 3.9 ± 0.2 Å along the length (vector 1). Fig. 3.7a shows several interesting characteristics regarding the edges of the needles. The upper portion of the image shows needle edges that are remarkably straight while the central region of the image shows more irregularly shaped edges. The tip of one of the needles is shown in the top left of Fig. 3.7a. The anisotropic spacing of the atoms can explain the preferential Bi growth direction. The atoms along the length of the needle are more closely packed (vector 1 in Fig. 3.7b), therefore atoms diffusing along this edge are less likely to become attached; the tip of the needle allows easier incorporation of additional Bi atoms, and extension of the needle. While the needles do slowly grow laterally over time as well, this process is initiated near the ends of the needle, at kink sites or at defects in the needle edge structure (Fig. 3.7a). Further structural aspects of these films are discussed in detail in Chapter 4.

3.4 Conclusions

The deposition of Bi on Au(111) has been imaged with STM in both the UPD and OPD potential regions. The UPD Bi lattice spacings agree with those previously reported. Evidence has been provided suggesting that the reconstruction of Au(111) is lifted by the adsorbed bismuth. This leads to the formation of gold islands when the Bi UPD coverage is close to its maximum value. The growth of the bismuth layers in the OPD region has been monitored in situ and exhibits very interesting needle growth behaviour. An explanation of the growth mode has been proposed based on atomic resolution images of the surface Bi layer.

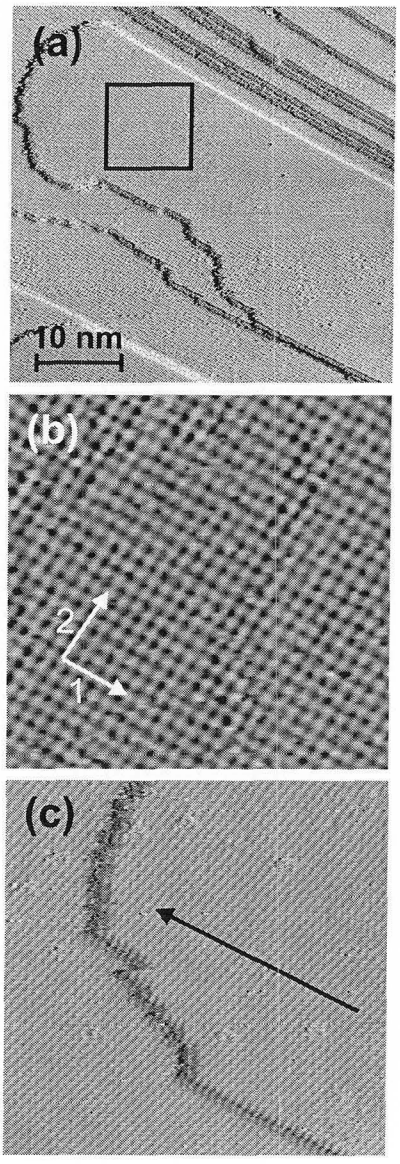

Figure 3.7: Atomic resolution images of Bi needle structures for thicker films. a) Atomic resolution image of the end of a bismuth needle and the edges of several other needle structures (45 nm × 45 nm). b) enlarged view of 100 nm^2 area outlined in a), showing atomic spacing of 3.9 ± 0.2 Å and 4.3 ± 0.2 Å along vectors 1 and 2 respectively. The angle between these vectors is 85 ± 2°. (For a) and b): E_{bias} = +50 mV, I_t = 3.0 nA.) c) Expanded view of the compact step edge of one of the Bi needles, the growth direction of the needle is indicated by the arrow (15 nm × 15 nm, E_{bias} = +50 mV, I_{t} = 1.0 nA).

Chapter 4

X-ray analysis of electrodeposited Bi films

4.1 Introduction

This chapter examines the structural details of multilayer Bi films electrodeposited onto Au(111) substrates. Chapter 3 discussed results concerning both the UPD and OPD behaviour of this system. The OPD films exhibit an interesting growth mode which involves the formation of Bi needle structures across the surface. Similar needle structures have been observed in other electrochemical systems [40]. A growth mode was proposed that accounts for the anisotropic needle growth across the three-fold symmetric substrate. This was based on scanning tunneling microscopy (STM) images of the films. For Bi on Au(111), the needles are evident from the very earliest stages of film growth up to films many hundreds of layers thick where they appear as surface features.

There has been much careful work carried out on characterising the properties of Bi thin films and nanostructures [11, 41], however, in all cases to the authors knowledge, electrodeposited Bi thin films have required suitable annealing to achieve single-

crystallinity [42, 43]. In the latter study, Bi was electrodeposited onto Si(100) (with a thin Au overlayer). After annealing, the films exhibited only the (003) and higher order reflections. In a study of Bi nanowires, the single crystal structure of the wires was achieved via deposition into porous alumina channels [44]. Deposition into these channels resulted in preferential (110) and (220) peaks in the XRD analysis. Elmorsi and Juettner deposited Bi onto CdS(0001) surfaces and observed three-dimensional growth of the Bi films [45]. This chapter outlines the characterisation of as-deposited Bi(012) films on Au(111). X-ray techniques are employed to examine the structure of the electrodeposited Bi films. This allows for detailed determination of the structure of the Bi films with respect to the underlying substrate. These results further support the growth mode proposed in Chapter 3. The results presented here outline the characterisation of Bi(012) films from the first few monolayers up to bulk structures. These findings have significance as the films themselves are of intrinsic interest and owe their unique characteristics to the detailed atomic structure of Bi. Furthermore, the as-deposited films may serve as the basis to fabricate high quality bismuth oxide materials.

4.2 X-ray pole figures of electrodeposited Bi films

All results discussed here pertain to Bi films grown in the manner discussed in Chapter 3, employing a potential step well into the OPD potential region. The needle-like surface morphology of the electrodeposited Bi films is maintained for all OPD film thicknesses studied. The crystal structure and epitaxial orientation of the film was determined using two X-ray techniques. Fig. 4.1 shows the 2θ X-ray spectrum for an electrodeposited film. The results clearly indicate that the film is crystalline. The Bi(012) (hexagonal) plane (and its second and third order reflections) are the only signals present due to the Bi film. The Bi(012) plane has been observed before (after annealing) on substrates such as p-GaAs [16, 46]. The spectrum also shows a strong

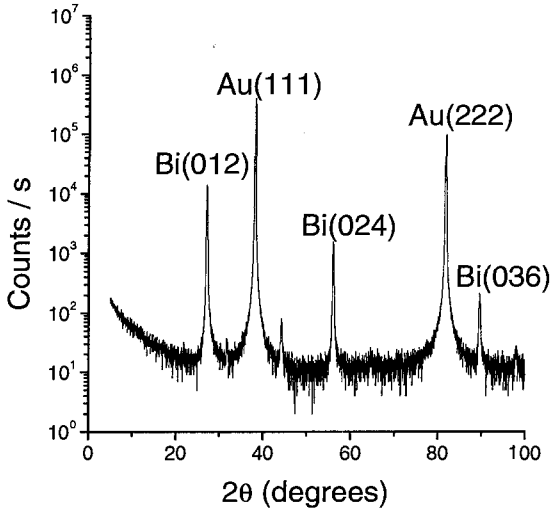

Figure 4.1: 2θ X-ray scan of a bulk deposited Bi film on Au(111).

contribution from the underlying Au(111) indicating a relatively thin film of Bi atop the gold substrate.

4.2.1 Pole figure acquisition

The azimuthal orientation of the Bi(012) film on the Au(111) substrate was determined using X-ray pole figure analysis. A schematic of the pole figure setup is given in Fig. 4.2. The schematic shows the angles of interest in this experiment. These include the Bragg angle (θ), the tilt angle (χ), the rocking angle (ω) and the azimuthal angle (ϕ). A number of different epitaxial electrodeposition systems have been characterised with this technique [47–49] including Bi deposition onto Si(100) [43]. To determine the in-plane orientation of a film (or substrate) with the index (h,k,l), another plane (h',k',l') is chosen that is located at some known angle to (h,k,l). The θ angle is set corresponding to the Bragg reflection (2θ) angle for the (h',k',l') plane. The tilt angle χ is then adjusted to bring the substrate into a position in which the Bragg condition is satisfied for the (h',k',l') planes. With these two angles set,

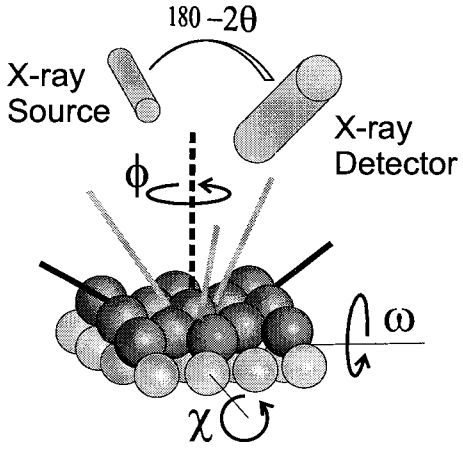

Figure 4.2: Schematic of the experimental setup for obtaining an X-ray pole figure. Angles pictured: θ (Bragg condition), ω (rocking), χ (tilt) and ϕ (azimuthal). Substrate pictured is representative of Bi deposited on Au(111). Gray lines represent the surface normals of the Au(220), (202) and (022) planes, black lines represent the surface normals of the Bi(202) and ($\bar{2}$22) planes (see text).

the sample is rotated through 360 ° about the perpendicular (with respect to the film and substrate) ϕ axis. This produces an azimuthal scan. The tilt angle (χ) can be varied over a range of 0-90 °. At each tilt angle, an azimuthal scan is produced (360° rotation in 3 degree steps). Combining all of these azimuthal scans results in an X-ray pole figure. A completely epitaxial film is evidenced by zero intensity at all values of χ except that corresponding to the angle between (h,k,l) and (h',k',l') [50].

4.2.2 Pole figures of Au(111) and Bi(012)

The results from the pole figure scans are shown in Fig. 4.3 for both the Au(111) substrate (a) and the electrodeposited Bi(012) (b). The radial grid spacing on each pole figure is 30 °. The radial distance measures the value of the tilt angle. The θ angle for the Au pole figure was set corresponding to the spacing between the Au(220) planes. The figure shows three peaks located at a tilt angle of 38.6 ± 0.6 ° (average

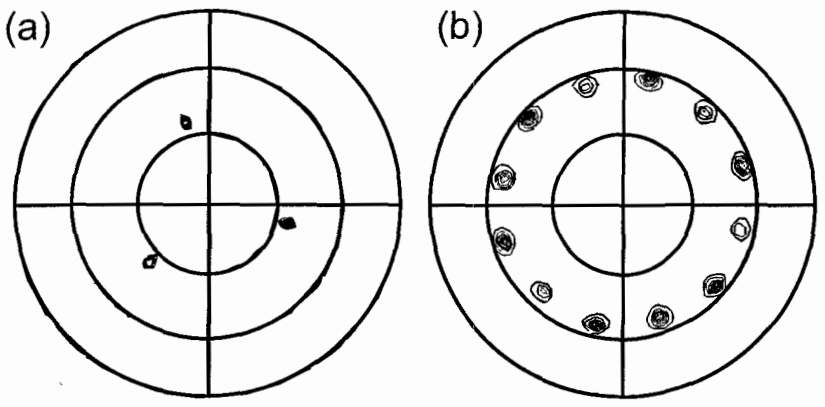

Figure 4.3: X-ray pole figures (contour plots) of Bi film electrodeposited on Au(111). a) Pole figure corresponding to the underlying Au(111) substrate showing 3 peaks at a tilt angle (χ) of 38.6 $\pm$ 0.6°. θ was set to correspond to the interplanar spacing between the (220) (and equivalent) planes. b) Pole figure corresponding to the Bi film showing 12 peaks at 54.5 $\pm$ 1.8°. θ was set to correspond to the interplanar spacing between the (202) (and equivalent) planes.

$\pm$ standard deviation). The azimuthal angle between these peaks is 119.7 $\pm$ 3.1°. The θ angle for (b) corresponds to the Bi(202) interplanar spacing. The figure shows 12 distinct peaks each corresponding to a tilt angle of 54.5 $\pm$ 1.8° . The azimuthal angle between the peaks is 30.1 $\pm$ 1.2°. The tilt angle was varied from 0 - 80° in 3 degree increments to generate each pole figure. No other peaks were observed. The peak intensities on the Bi pole figure are not constant. Fig. 4.4 is a 3-D rendering of the pole figure shown as a contour plot in Fig. 4.3b. In this view it is clear that the pole figure consists of 6 relatively strong peaks and 6 weaker peaks that alternate at 30.1 $\pm$ 1.2° azimuthal angles.

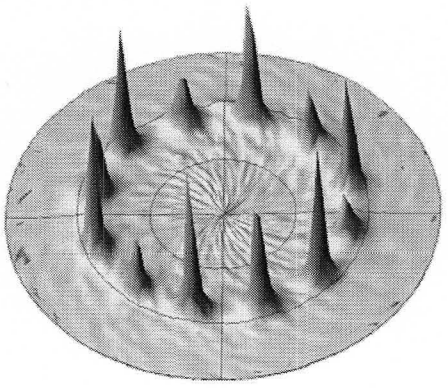

Figure 4.4: 3-D rendering of the pole figure shown as a contour plot in Fig. 4.3b. Six peaks of relatively strong intensity are separated by 60°. Six more peaks of relatively weaker intensity are interspersed between the stronger peaks, and are also separated by 60°.

4.3 Structural details of the Bi(012) films

4.3.1 Coordinate systems

The X-ray experiments allow for a detailed analysis of the bulk structure of the electrodeposited Bi films and their epitaxial relationship to the substrate. Bismuth has a rhombohedral lattice and belongs to the $R\bar{3}m$ space group (symmetry group D_{3d}). The rhombohedral lattice can be superimposed onto a hexagonal lattice structure as shown in Fig. 4.5a. This figure shows the pertinent lattice vectors for both systems and the figure caption lists the lengths and angular relations between the vectors. Each rhombohedral lattice cell contains 2 Bi atoms, with radii of 1.55 Å. In the representation shown in Fig. 4.5a, the two atoms would be located directly along the c_{hex} axis, one at 2.81 Å and another at 9.05 Å [5]. The length of the c_{hex} axis (the body diagonal of the rhombohedral cell) is 11.86 Å, indicating that the Bi atoms are spaced unevenly through the rhombohedral unit cell. Each lattice point of the rhombohedron has one Bi atom 2.81 Å directly above it and one 2.81 Å directly below it in the orientation shown. The atoms above the lattice points are referred to here as 'up'

atoms while the ones below are referred to as 'down' atoms. All of the down atoms are translationally-equivalent to each other in the rhombohedral structure (likewise for the up atoms).

Fig. 4.5b displays the Bi(012) plane in the hexagonal system. The results from the 2θ X-ray diffraction experiment indicate that this plane is electrodeposited parallel to the underlying Au(111) substrate. The positions of the atoms within the bulk Bi structure were modelled based on the crystallographic Bi data [5]. Fig. 4.5b also shows the positions of the five atoms that form a 2D unit cell in the Bi(012) plane. The centres of atoms 1, 2, 4 and 5 are equidistant from the (012) plane. Each of these atoms is a down atom in a rhombohedral cell. Atom 3 lies 0.17 Å below the plane created by the surrounding atoms. This atom is an up atom (see Appendix A for exact coordinates). The arrangement of the atoms leads to a slightly puckered structure of the Bi(012) plane that has been shown previously [46]. Atom 3 is also not located evenly amidst the other atoms. The centre-to-centre distance between atoms 1 and 3 and atoms 2 and 3 is 3.11 Å while the $3-4$ and $3-5$ distances are 3.48 Å (see also Fig. 4.7a). The Bi(012) surface unit cell is rectangular. The $1-4$ distance is 4.75 Å and the $1-2$ distance is 4.55 Å. Fig. 4.5c shows a view of the arrangement of the atoms looking directly down the (012) surface normal. A side view to illustrate the parallel between the atoms and the (012) plane is given in Fig. 4.5d.

4.3.2 Epitaxy determined from pole figures

The x-ray pole figure data can be used to determine the epitaxial arrangement of the Bi(012) plane on the Au(111) substrate. The pole figure for the Au(111) is relatively uncomplicated. The Au(220) plane lies at an angle of 35.3° from the Au(111) plane. Fig. 4.3a shows three peaks at a tilt angle of $38.6 \pm 0.6\,°$, reasonably close to that

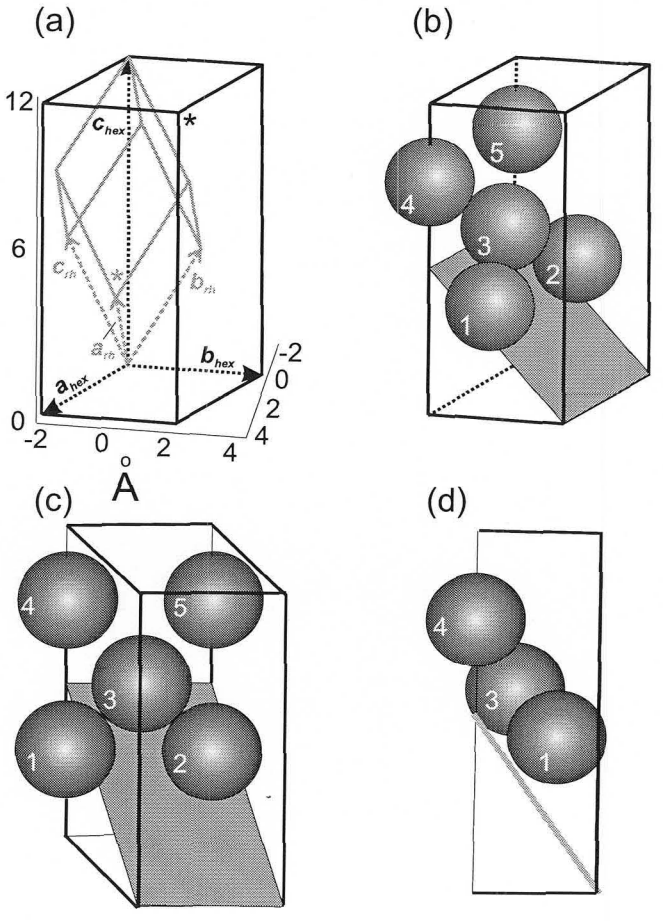

Figure 4.5: Coordinate systems and pertinent relations used for modelling of Bi structures. a) Rhombohedral coordinate system (gray), $|a_{\mathrm{rh}}| = |b_{\mathrm{rh}}| = |c_{\mathrm{rh}}| = 4.75$ Å. Hexagonal coordinate system (α=β=90°, γ=120°, black), $|a_{\mathrm{hex}}| = |b_{\mathrm{hex}}| = 4.55$ Å, $|c_{\mathrm{hex}}| = 11.86$ Å. In both systems, the vertex marked with an asterisk is closest to the reader. The relation between the rhombohedral and hexagonal systems follows the 'obverse' orientation [51]. b) (012) plane of the hexagonal coordinate system (shaded) along with atoms that form a unit cell on the Bi(012) plane. The centres of atoms 1, 2, 4 and 5 lie in the same plane. The centre of atom 3 lies 0.17 Å out of this plane. c) View of the Bi surface unit cell atoms from directly along the (012) surface normal. d) Side-view of the hexagonal unit cell and bismuth atoms.

of the Au(220) plane. The slight discrepancy likely arises from the estimation of the peak centres The other two peaks are the result of reflections from the Au(202) and the Au(022) planes which are symmetrically equivalent to the (220) plane in the cubic system. The 120° azimuthal angle between each of the peaks demonstrates the 3-fold symmetry of the Au(111) surface.

Fig. 4.3b shows 12 distinct peaks in the Bi pole figure each located at a tilt angle of 54.5 ± 1.8°. The Bi(202) plane is located at an angle of 55.3° from the Bi(012) plane. Additionally, the Bi($\bar{2}$22) plane has the same interplanar spacing as the Bi(202) and is symmetrically equivalent to it. The normals to these two planes (202 and $\bar{2}$22) lie at an azimuthal angle (ϕ) of 180° from each other and are illustrated in Fig. 4.2. The pole figures allow for a conclusive assignment of the relationship between the unit cell of the Bi(012) film and the Au(111) substrate. The key factors that result in the observed numbers of spots in the pole figures are outlined in Fig. 4.6. Fig. 4.6a shows one arrangement of the Bi(012) surface unit cell that results in two spots in the Bi(012) pole figure. One vector (shown as an arrow in the figure) represents the Bi(202) surface normal and accounts for one spot on the pole figure. The Bi($\bar{2}$22) normal (shown by the a vector pointing in the opposite direction) accounts for another spot. The arrangement of the Bi and Au surface unit cells was determined by comparing the relationship between the Bi(202) and Bi($\bar{2}$22) spots with the positions of the Au(220), (022) and (202) spots on the pole figure (the exact positions of these vectors with respect the Au(111) unit cell are given in Fig. 4.6c).

Four additional spots on the pole figure can be accounted for by considering the 3-fold symmetry of the underlying Au(111) surface. The Bi(012) electrodeposited on the surface is equally likely to be formed in three orientations, one corresponding to 'no rotation', another rotated 120° from this arrangement and a third rotated by 240°. These three arrangements are equivalent in terms of the relationship with the Au(111) and result in six pole figure spots that are represented by solid black arrows in Fig. 4.6d.

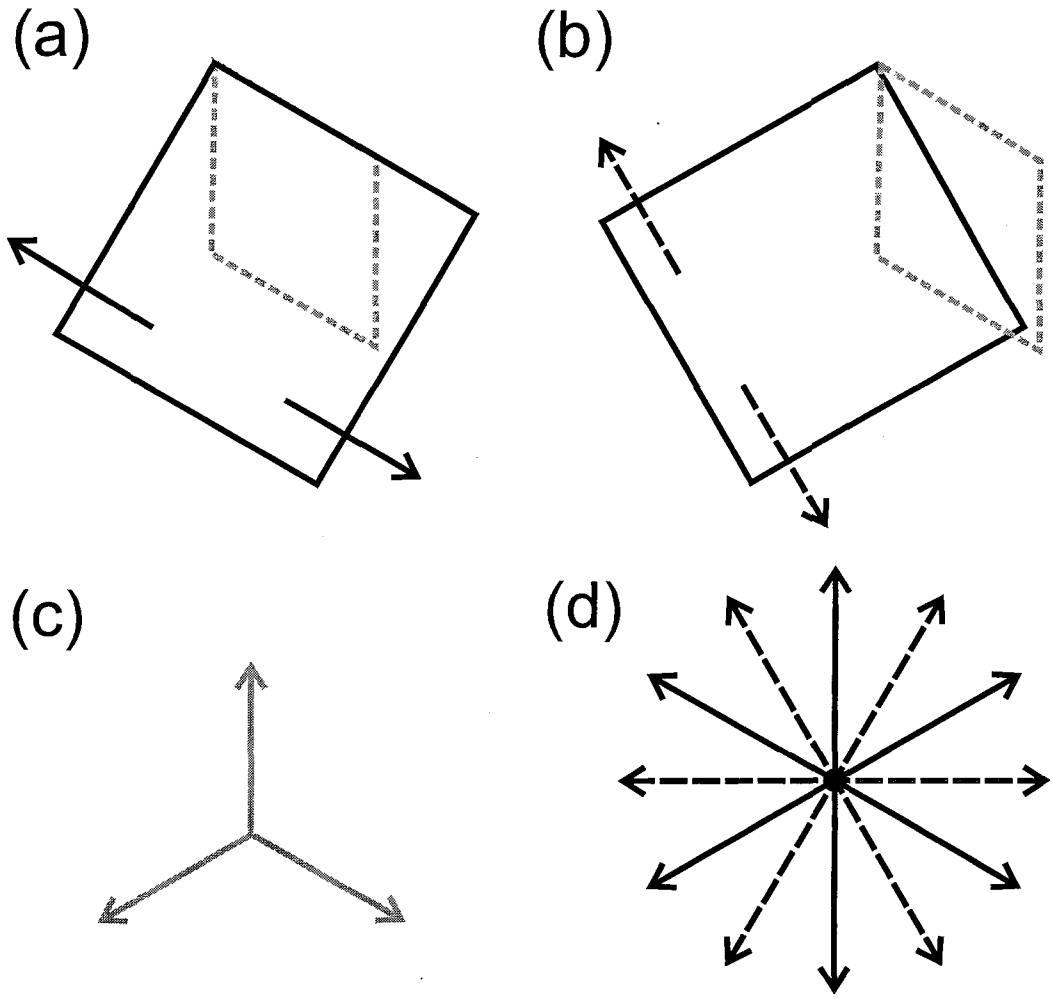

Figure 4.6: Arrangement of Bi(012) unit cells with respect to the Au(111) unit cell as determined by pole figure analysis. a) One arrangement of the Bi(012) unit cell that accounts for two spots on the bismuth pole figure. The dashed gray line corresponds to the Au(111) unit cell. The black arrows correspond to projections (in the (012) plane) of the Bi(202) and $(\bar{2}22)$ surface normals. b) 30 degree (cw) rotation of Bi(012) unit cell that accounts for two more spots on the pole figure. c) Projections (in the Bi(012) plane) of the Au(220), (022) and (202) surface normals for the orientation of Au(111) shown in both a) and b) (compare with Fig. 4.3a). d) 120 and 240° rotations of the Bi(202) and $(\bar{2}22)$ surface normals that account for the 12 spots observed in Fig. 4.3b).

The six additional spots in the pole figure indicate the presence of another arrangement of the Bi(012) on the surface. The symmetry of the Bi crystal alone cannot account for the additional spots. Recall that the instrument has been set specifically to probe for the interplanar spacing of the Bi(202) (or($\bar{2}$22)) planes. Because of this fact, the presence of a spot located at a 30° azimuthal angle to another spot at this tilt angle (χ) indicates a second orientational domain of the Bi film. This additional arrangement of the Bi(012) surface unit cell with respect to the Au(111) surface unit cell is given in Fig. 4.6b. Identical arguments to those already discussed lead to the conclusion that this arrangement accounts for the additional six spots in the pole figure that are illustrated schematically as dashed arrows in Fig. 4.6d.

4.3.3 Models of atomic arrangements

The pole figures allow a model to be built to demonstrate the epitaxy of the electrodeposited film on the gold substrate. An overview of the calculations performed to produce this model is given in Appendix A (page 139). In the representation shown in Fig. 4.3, the normals to the Bi(012) and Au(111) planes are on the same axis (coming directly out of the page, in the centres of the pole figures). The epitaxy is determined by the appropriate rotation of one modelled plane with respect to the other such that the crystal arrangements mimic those found in the pole figures. One of these arrangements, showing the three normals for the Au(220), (202) and (022) planes and normals for the Bi(012) and ($\bar{2}$22) planes, is shown as a side view in Fig. 4.2. Fig. 4.7 shows top views of two arrangements of the Bi(012) plane on the Au(111) substrate. It is stressed that the models demonstrate the relative arrangements of the bulk film and substrate structures. Structural differences may exist at the solid/solid and solid/electrolyte interfaces or solid/air interfaces that are not probed with this X-ray experiment. Each unique arrangement accounts for one

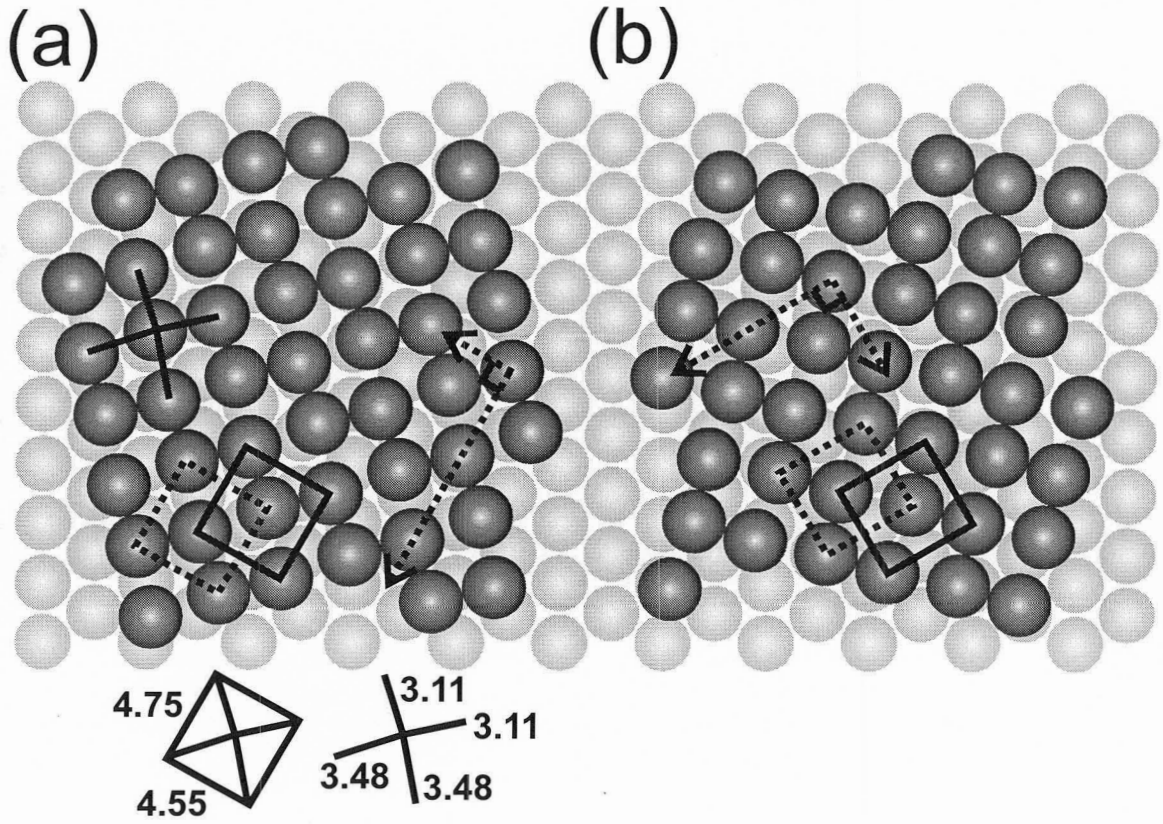

Figure 4.7: Epitaxy of the Bi(012) plane on the Au(111) substrate. Two unique arrangements a) and b) account for the two sets of six peaks in the pole figure (Figure 4.4). Note that the arrangements are not mirror images. Unit cells are outlined on each surface. The spacing corresponding to the interatomic distances (centre-to-centre in Å) are shown by the line diagrams below a). The dotted line vectors in both images represent one corner of a coincidence lattice with the lengths of the arrows indicative of the relative lengths of the sides (both coincidence lattices are much larger than the figure). The coincidence lattice in a) is 89.6 Å $\times$ 268.0 Å and in b) is 141.1 Å $\times$ 227.8 Å.

set of six peaks in the Bi pole figure as discussed previously (each arrangement shown in the figure accounts for two peaks and 120° and 240° rotations of these structures account for the additional four peaks). An outline of the 2D unit cell is shown for both unique orientations (solid line). The dotted line outline connects those atoms that are modulated slightly out of the plane, lying 0.17 Å out of plane from the other atoms. Each layer of the film is comprised of interspersed rectangles of higher and lower atoms. The modulation is discussed in more detail below.

The pertinent distances between the atoms are given below Fig. 4.7a. The vectors corresponding to the edges of the coincidence lattice for the film and substrate are shown in each figure. The vector arrows have been shown approximately to scale with respect to each other. However, for both arrangements the coincidence lattice is much larger than can easily be shown on the figure (the details are given in the figure caption). The size of the coincidence lattices indicates that the structure of the gold surface plays a relatively small role in templating the overall structure of the deposited film. This supports the findings in other studies and demonstrates that the deposition of the Bi(012) plane is largely substrate independent [16, 46]. The relation between the pole figures for the Bi and Au structures (Fig. 4.3) indicates that the arrangement shown in Fig. 4.7a is responsible for the more intense peaks observed in the pole figure (Fig. 4.4). The set of 6 peaks showing reduced intensity are represented by the arrangement shown in Fig. 4.7b.

The presence of 12 distinct peaks in the pole figure has interesting implications regarding the preference of one arrangement over another. If the rotational orientation of the Bi(012) film had no dependence on the Au(111) surface structure, the pole figure would show a ring of intensity instead of distinct spots. This follows because all possible rotational arrangements of the Bi would be equally likely. The 12 spots have been shown to be the result of two distinct arrangements on the surface. The relationship between these two arrangements is of interest. The modelled surface unit cell of the Bi(012) is rectangular, with sides of 4.55 Å and 4.75 Å. For a

square unit cell on a three-fold symmetric surface (such as Au(111)), if one edge lies along an atomic row of Au(111), the adjacent edge lies along the $\sqrt{3}$ direction. A rotation of 30° for a square structure on Au(111) would still result in one side lying along an atomic row and the other lying along the $\sqrt{3}$ direction. Since the edges are equivalent for a square, the 30° rotations of the unit cell are equivalent as well. The result is different for a rectangular unit cell. Since the sides are inequivalent by definition, a rotation of 30° on the surface results in an inequivalent structure. If the shorter side is in registry with an atomic row before the rotation, it comes to rest along the $\sqrt{3}$ direction after the operation, and the converse happens with the longer side. This difference is very subtle for a structure that is close to being square as is the case for the Bi(012) cell. However, this may point to the fact that for very early stages of the film growth, the structure is square, and the dimensions of the unit cell relax to those of the (012) plane with continued growth. The UPD structure of Bi on Au(111) exhibits a rectangular unit cell (see Chapter 3 and [19]) and has been shown to exhibit contraction of one side of the nonprimitive unit cell with changes in potential [19]. This could account for a square arrangement in very early film development that leads to the structures responsible for the distinct peaks observed in the pole figure for the bulk film.

The possibility also exists that the two arrangements shown in Fig. 4.7 are energetically equivalent. If the atoms along the 'short' side of the surface unit cell interacted with the surface in the same way as those along the longer edge (in terms of atoms located in sites such as bridging or atop arrangements), another explanation for the spots could be provided. However, it has been shown that the alignment of the unit cells of Bi and Au results in very large coincidence lattices (Fig. 4.7). This reflects the fact that the Bi(012) atoms and Au(111) substrate are quite incommensurate and possess numerous bonding arrangements within the surface unit cell. For this reason it is difficult to rationalise a specific arrangement that would lead to distinct spots in the pole figure as opposed to a ring that would signify the presence

of all rotational arrangements.

4.3.4 Multilayer and needle structure

Most of the electrodeposited Bi(012) films consist of tens to hundreds of layers so an understanding of the three-dimensional structure of the films is desirable. Fig. 4.8 shows the arrangement of three consecutive layers of the Bi(012) film in both top view (a) and side view orientations (b). The film shown corresponds to arrangement 'a' in Fig. 4.7. The 'edges' of the film have been assigned based on the anisotropy in the atomic spacing of the film. The 'open edge' corresponds to the edge of the 2D unit cell with Bi atoms evenly spaced at 4.75 Å intervals. The 'compact edge' is comprised of atoms lying along the 4.55 Å side of the unit cell (this determination has been made based on the structure of the Bi surface observed via STM, discussed shortly). STM imaging has revealed (Fig. 3.7a and b, page 24) that the needle growth occurs perpendicular to the more open edge. The top view shows that consecutive layers lie almost directly over the underlying layers. However the most closely-packed atoms (separated by 3.11 Å) are shifted by one atomic row with each layer. This structure results in offset atoms at the edges of the growing needles. An example of this relationship is outlined near the bottom of Fig. 4.8a. This structure is evident at the compact edges of the needles observed via STM (see Fig. 3.7c). This slight offset of the adjacent planes of Bi(012) also accounts for the highly-stepped appearance of some of the larger needle structures.

A similar but more openly spaced example of this type of stepped structure can be seen along the more open edge. From the observations obtained via STM, it appears that kink or defect sites developing along this edge play an important role in the morphology of the film. Needles broaden predominantly due to needle expansion at the tip (along this open edge) and the progressive filling-in down the long axis of the needle (Fig. 3.7a). If the front (open) edge of the needle extends in width by one or

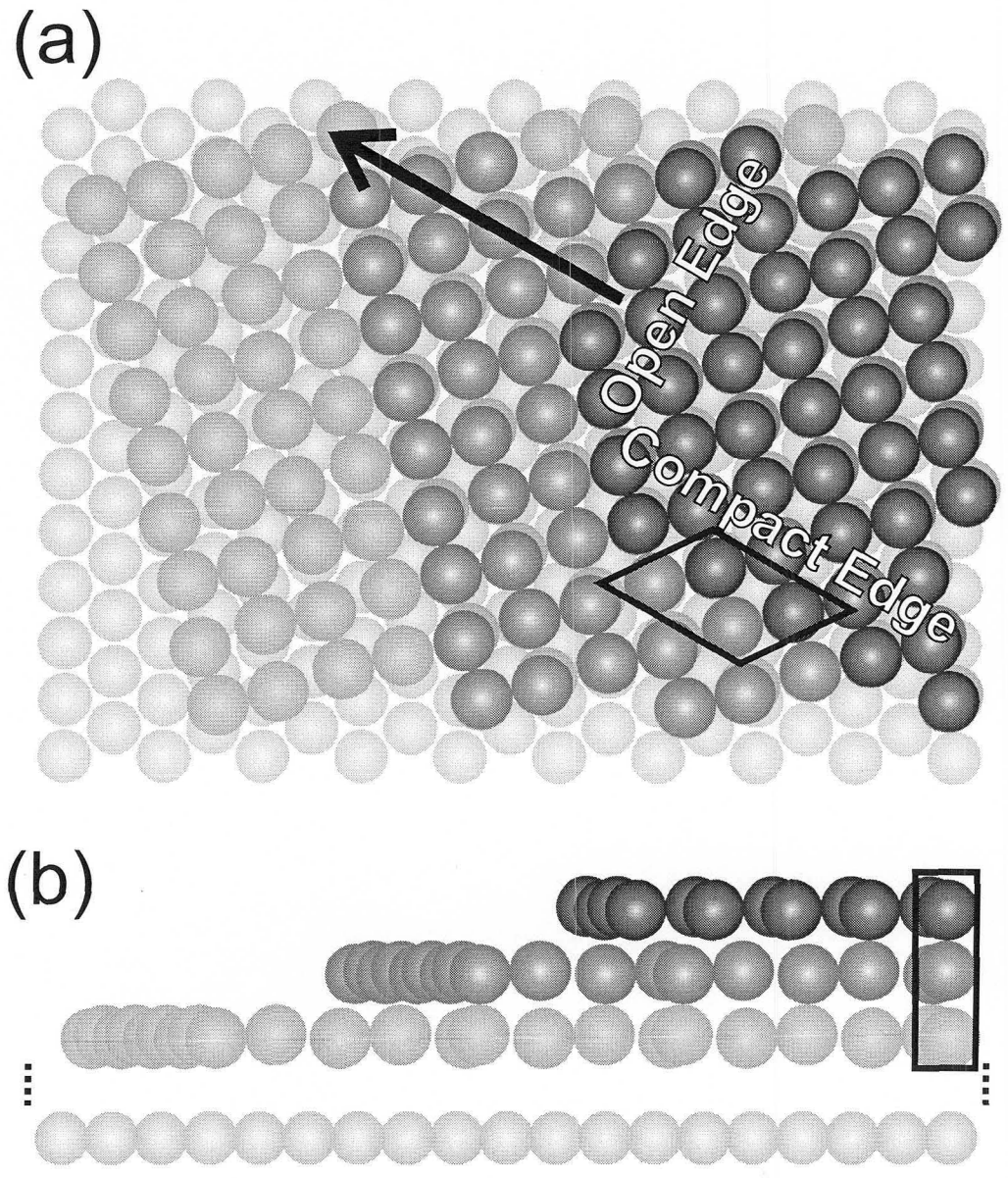

Figure 4.8: Arrangement of atoms in multilayer deposits of Bi on Au(111). a) Top view of up to 3 layers (darker atoms are higher in this view). The labels correspond to the STM findings of the needle morphology. The arrow indicates the predominant direction of needle growth. The outlined area in a) illustrates the relation between layered atomic rows at the edge of a needle structure. b) Side view of the arrangement shown in a), demonstrating the height modulation per layer (bulk) of the Bi(012) deposit. The outlined area to the right shows the uneven spacing between successive layers (see text). The dotted line separation indicates that the interface region may have slightly different structure.

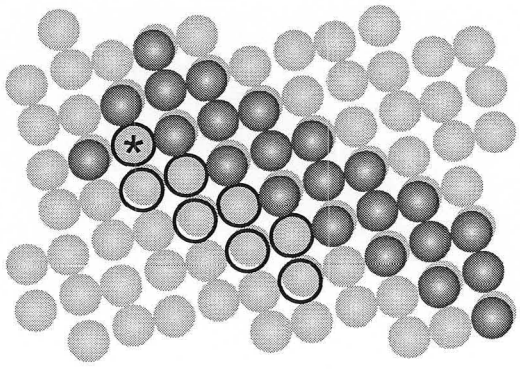

Figure 4.9: Closeup view of a Bi needle edge. The open circles denote the positions of Bi deposition as the edge fills in due to the presence of a defect site created at the tip. The process begins with the position marked with an asterisk and proceeds left-to-right.

two Bi atoms, a very favourable deposition site is created in the Bi(012) plane. An example of this is shown in Fig. 4.9. Once the tip of the needle extends laterally, a site (marked with an asterisk) is created which can be filled in with a diffusing surface Bi atom. This sequence produces another favourable deposition site and the process continues down the side of the needle. This provides structural detail to support the previous assertion that the needles broaden due to defect formation at the tip. This also serves to validate the observation that incorporation of surface diffusing Bi atoms occurs much more readily at the more openly-spaced needle tip as opposed to directly along the compact sides, giving rise to the observed growth anisotropy. It is possible that the incorporation of atoms down the length of the needle occurs through pairs of Bi atoms depositing (one right after the other) to create a bilayer structure (maintaining the close proximity between adjacent layers outlined in Fig. 4.8a). This type of structure seems evident along the edges of the growing needles (see Fig. 3.7a and c). However, the STM images are not highly enough resolved in space or time to confirm this.

The Bi(012) planes (bulk) are not perfectly flat. Fig. 4.8b shows the side view of the layered film shown in (a). Note that the figure indicates an area at the interface

between the bulk structures that may exhibit a slightly different arrangement. Here the very small (0.17 Å) corrugation of the planes is clearer. The modulation over several layers leads to an interesting structure in the z direction of the film. An example of this arrangement is outlined to the far right in Fig. 4.8b. The atom on the lowest layer lies 3.48 Å below the atom almost directly above it. This atom in turn lies only 3.11 Å below the next level. The next spacing would be 3.48 Å and the pattern would continue. The entire Bi film is therefore made up of atoms paired at 3.11 Å and 3.48 Å that are almost evenly distributed throughout the film (they are not quite even due to the uneven spacing of the 2 atoms in the 2D surface unit cell).

4.3.5 Surface structure

Fig. 4.10 attempts to reconcile the observed surfaces in the experiment with models of bulk Bi(012). In general the surfaces in the STM images appear characteristically different from the modelled bulk surfaces. The surfaces in the STM image appear uniform in terms of the interatomic spacing along surface vectors 1 and 2 (Fig. 3.7b, this structure is also shown to scale in Fig. 4.10c). The surface appears to be less closely-packed than the bulk surface model suggests (see Fig. 4.10a). STM images are sometimes subject to 'drift'. It is possible that a slight drift of the slow scan axis over the course of the image acquisition could account for the small deviation in angle from the predicted 90° structure. This minimal drift wouldn't appreciably obscure the appearance of the needle edge structure, which has been shown to closely resemble the modelled surface. However, it seems unlikely that the possible drift of the microscope could account for the more dramatic difference observed in the spacing of surface atoms when comparing the experimental and modelled surfaces. Fig. 4.10b shows the bulk surface model with the out-of-plane atoms shown faintly. A comparison of the spacing between the atoms in (a) and (b) shows that the second structure agrees much more closely with the STM images. It is proposed that the anisotropic

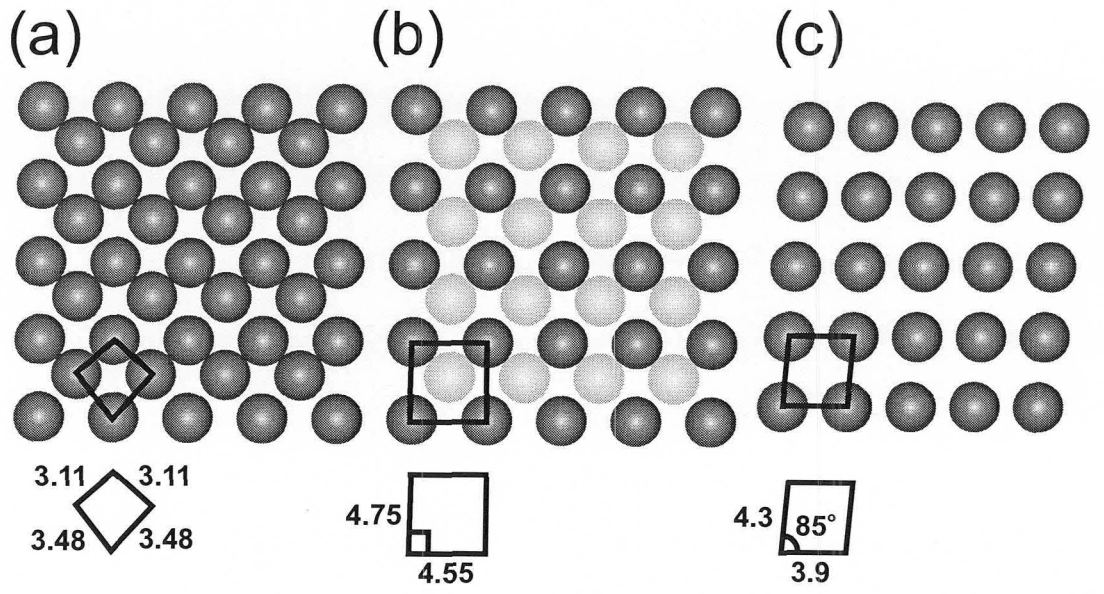

Figure 4.10: Comparison of modelled and experimental Bi surface structures. Measurements of structures are shown below images. a) Bulk surface model. b) Bulk model with the out-of-plane atoms shown in a lighter tone. c) Experimentally observed arrangement of surface.

environment of the solid/solution interface enhances the surface corrugation. In this scheme, the faint atoms in (b) are not seen in the STM images. Furthermore, this enhanced corrugation could allow for the small amount of surface compression required to transpose structure (b) to (c). As well, the interaction of ions in the electrolyte (H^+ and ClO_4^-) with the surface atoms could contribute to this effect. It is possible that the surfaces imaged with STM represent uncompleted layers (with the out-of-plane atoms actually missing). However, a noticeable change in density of surface atoms has never been observed during imaging that one might expect to accompany this process.

4.4 Conclusions

X-ray analysis of electrodeposited Bi films has revealed the epitaxial growth of (012) surfaces of Bi atop the underlying structure of the Au(111) substrate. Pole figure analysis of the electrodeposited films has enabled modelling of the detailed atomic structure and rotational orientation of these films. Two unique epitaxial arrangements have been identified. Analysis of the two arrangements suggests that the structure may be slightly different (from bulk Bi(012)) during early stages of film growth The large coincidence lattices observed for both unique arrangements support previous findings of the predominance of the Bi(012) plane in electrodeposition systems on a variety of substrates. The three-dimensional structure of the films has also been modelled and provides structural evidence for the anisotropic growth observed experimentally. The differences between the surface structures and the modelled structures have been discussed and explained in terms of enhanced surface corrugation and concomitant compression.

Chapter 5

EQCM studies of Ag and Cu electrodeposition

5.1 Introduction

The electrochemical quartz-crystal microbalance (EQCM) has made a significant impact in recent years as an *in situ* technique capable of measuring the mass increase or decrease at the electrode surface as a function of potential [8,52]. The mass response should ideally be due only to the surface reactions; however studies have been made on the effects of solution viscosity and temperature [53], electrode orientation [6], solvent molecules at the interface [54–57], mass location on the electrode [58] and surface morphology/roughness [59,60]. Metal deposition systems have been popular targets of EQCM study, including both underpotential and overpotential deposition [27,61,62] with a wide variety of substrates, metals and electrolytes. These apparently simple systems can give masses that deviate from those expected based on the stoichiometry of the known deposition reaction. These deviations call into question the utility of the EQCM if they are due to effects such as those above, but if they are not due to such artifacts, then they may be a source of useful information on the deposition process

itself. It is important therefore to find some systems or conditions under which artifacts are absent to use as reference points. This chapter addresses these issues for silver and copper electrodeposition on iodine-covered and bare Pt electrodes.

In the case of silver electrodeposition, Vatankhah *et al.* [63] have recently undertaken a careful study of the conditions under which silver deposition can be used as a calibration system. They showed that reliable and consistent results can be obtained from chronopotentiometry, chronoamperometry, and CV measurements extrapolated to zero sweep rate, but that deviations occur in CV measurements at higher sweep rates, e.g., 20 $\mathrm{mV\,s^{-1}}$. Thicker films (7-15 monolayers (ML)) were required for reliable calibration. Since their objective was to find a reliable calibration procedure, they did not investigate in detail the reasons for deviations at higher sweep rates, other than to suggest that diffusion may be playing a role. It is shown here that if the deposition occurs instead on an iodine-covered surface, deviations from the ideal mass do not occur at the same sweep rates. This result means that the deposition of silver on iodine-covered Pt is a good system for calibrating the EQCM. It also means that the deviations from ideal mass in the absence of iodine have an origin in the growth mode of the film itself, since the effects of artifacts would be similar in the two systems. It is suggested that the ideal mass for deposition in the presence of iodine is due to a consistent interaction of the iodine with the electrolyte in the presence or absence of silver, and to a layer-by-layer growth mode (constant roughness) for thicker films. In contrast, a reduction in roughness occurs as silver is deposited in the absence of iodine, which leads to a deviation from the ideal mass.

The deposition of silver on the iodine-covered surface was chosen as a comparative system because the silver is known to deposit underneath the iodine layer in the archetypal system: Ag deposition onto Pt(111)$(\sqrt{7} \times \sqrt{7})R19.1°$-I to give the "silver iodide" surface compound Pt(111)(3×3)AgI. This system was first discovered by Hubbard [64, 65], and has since been well investigated by others (see refs. in [66]). Available evidence suggests that introducing steps [67], changing the close-packed

iodine layer to (3×3) [68], or changing the crystal face to Pt(100) [69] do not alter the fact that the silver deposits underneath the iodine, so this would also be expected for deposition on the polycrystalline electrodes used here. The iodine layer before and after deposition should be a nearly close-packed layer exposed to the solution, so that the interactions with the electrolyte may be expected to be similar. Furthermore, the iodine layer on Pt acts as a van der Waals surface that may be used as a substrate for non-dissociative adsorption of large organic molecules [68]. In the present case, the interactions with the electrolyte are expected to be weak and non-directional.

Similar studies have been carried out for copper deposition onto iodine-covered electrodes [70–73]. On single crystal surfaces, LEED indicates that the CuI structures are well ordered [70], but scanning tunneling microscopy studies performed by Baltruschat *et al.* [74] revealed the formation of three-dimensional islands of copper as the deposition proceeded.

5.2 Silver electrodeposition onto iodine-covered polycrystalline platinum

The current and frequency responses as a function of potential for the system with and without silver present are shown in Fig. 5.1. It is evident that in the absence of silver, both the current and frequency responses are small over the $0.4-1.0$ V potential range, indicating little or no change in the iodine layer. There is a 5 Hz change in frequency over this potential range that is due to anion desorption as the electrode potential is made more negative. This reproducible change is small compared to the changes for the silver reactions discussed below. Here it is noted only that it is large compared to the instrumental drift, which is estimated as less than 0.2 Hz min^{-1} (See Fig. 2.3, page 9).

The addition of silver leads to large changes in both current and frequency re-

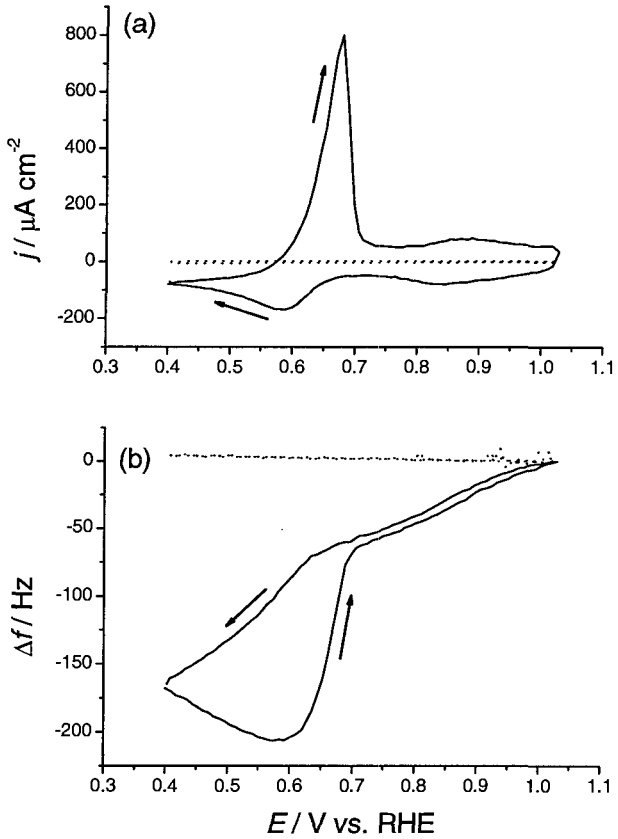

Figure 5.1: Comparison of EQCM response to silver deposition with and without iodine coating. a) Current response of the iodine-covered EQCM Pt electrode with (solid) and without (dotted) 1 mM Ag^+ present during potential cycling in 0.5 M $HClO_4$, 100 mV s^{-1}. b) Corresponding microbalance frequency response.

sponse. Fig. 5.1a shows two features in both the negative- and positive-going sweeps. The negative-going sweep shows a very broad peak centered around 0.84 V and a less broad peak around 0.58 V. In the positive-going sweep, a large peak appears at 0.66 V and a broad peak develops around 0.87 V. Previous studies [68] of silver deposition on iodine-covered Pt(111) showed that the first peak corresponding to the formation of a (3×3)AgI monolayer occurred at 1.06 V vs. RHE (converted from the original $Ag|Ag^+$ reference scale). The charge measured under this peak from 1.03 V to 0.69 V is 195 μC cm^{-2}, close to the expected monolayer charge of ca. 205 μC cm^{-2} calculated as the average of the first UPD layers of Ag on Pt(100) and Pt(111). (For subsequent layers a charge of 205 μC cm^{-2} is also assumed, a value within 20% of known charges for Ag layers in bulk Ag or UPD on Pt(100) or Pt(111).) Fig. 5.1b shows the shift in frequency produced during the potential cycle. A steady decrease in frequency takes place from the beginning of the negative sweep. A larger reduction in frequency begins concurrently with the second, larger reduction peak. During the positive sweep, the frequency continues to decrease until the current becomes positive at 0.57 V, indicating that deposition is still taking place up to this potential in the positive scan. The frequency increases dramatically at the potential corresponding to the large anodic voltammetry peak and continues to increase through the broad peak at the end of the cycle.

The mass/charge ratio (in grams per mole of electrons) of the species deposited or stripped from the surface is calculated by dividing the measured mass change by the charge passed in the same process, the charge being determined by integration of the current. This ratio is occasionally referred to loosely as the 'mass'. Figs. 5.2b and c show the mass/charge relation for the deposition and stripping over a potential range the same as in the voltammogram in 5.1a. The instrument was calibrated from the mass/charge response for the deposition, assuming that only silver was deposited on the surface. Vatankhah *et al.* [63] have recently demonstrated that the value of the calibration constant (C_f) derived from silver deposition in the absence of iodine is

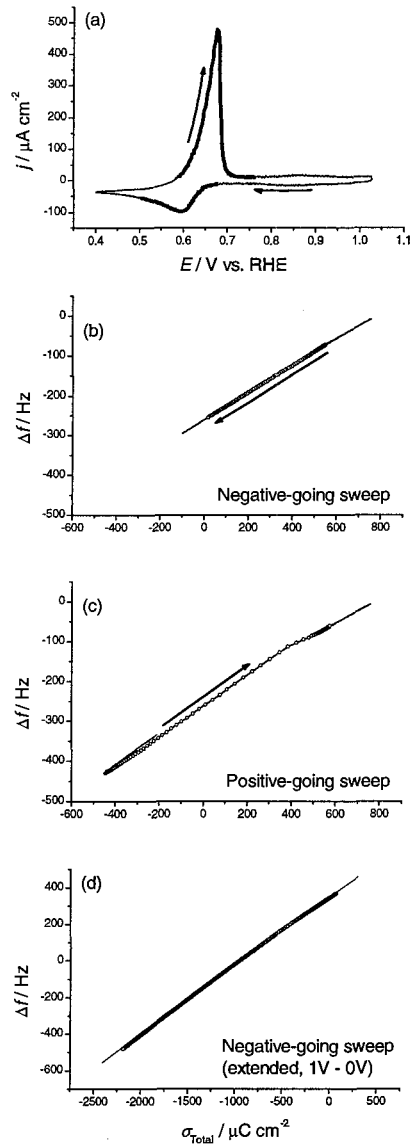

Figure 5.2: Frequency vs. charge density analysis for silver deposition onto iodine-coated Pt. a) Cyclic voltammogram for the iodine-covered EQCM electrode in 0.5 M $HClO_4$ + 1 mM Ag^+, 20 mV s^{-1}. b) Frequency vs. charge for the negative- going potential sweep. Emphasised points correspond to the highlighted region in a). c) Frequency vs. charge for the positive-going potential sweep. d) Frequency vs. charge for the negative-going sweep using extended potential limits (1 V to 0 V).

dependent upon the scan rate applied in cycling experiments. (Note that C_f in [63] is defined differently from here.) Within the error limits stated, no evidence was found here for a trend with sweep rate for deposition on the iodine-covered surface over the range $0.002 - 0.100$ V s^{-1}. This difference in scan-rate dependence between the iodine-covered and iodine-free systems is likely due to the morphological differences in the deposition of the two systems, as discussed below. Nonetheless, a standardised scan rate of 0.020 V s^{-1} was used for all calibration and mass data reported here.

The value for C_f from Eq. 2.1, (page 10) was determined experimentally to be 0.188 Hz ng^{-1} cm^2 with a standard deviation of 0.004. The theoretical value for C_f using the physical properties of the crystals employed is 0.183 Hz ng^{-1} cm^2. The correspondence between the experimentally-determined and theoretical values of C_f provides strong evidence that the assumed mass change (that of silver being deposited, with a molar mass of 107.87 g mol^{-1}) is correct and silver alone is being deposited beneath the iodine layer as expected. The results of these experiments indicate a deposited mass of 108 ± 6 g mol^{-1} for the process of silver deposition onto an iodine-coated electrode:

$$\mathrm{PtI(ads)} + \mathrm{Ag^+} + \mathrm{e^-} \rightarrow \mathrm{PtAgI(ads)} \tag{5.1}$$

Reaction 5.1 implies the deposition of the initial monolayer of silver at the iodine-covered surface. However, as shown below, the mass response corresponds to silver deposition alone after many monolayers have been deposited.

The mass corresponding to the stripping process taking place during the positive sweep (Figure 5.2c) is 111 g mol^{-1}, indicating the simple reversal of Eq. 5.1 within the stated confidence interval. The small deviation from linearity in the fit to this plot is attributed to a small artifact, discussed further below.

The linearity of the frequency/charge relation in Fig. 5.2 indicates that the mass change at the electrode surface is constant over the whole range of potential shown in the voltammogram. Both deposition peaks therefore correspond to reaction 5.1

(UPD and bulk deposition), and this is the only reaction occurring at the surface over this potential interval. This remains true, and the same mass is found, if the potential range is extended to $0 - 1$ V (Fig. 5.2d), so that the amounts of silver deposited are now at least 11 layers. (The positive limit was maintained at less than 1.05 V in order to avoid oxidation of the iodine layer. Oxidation of the iodine layer coincides with platinum oxide formation and occurs around 1.15 V.) Note that the values calculated here and elsewhere have used the total charge density (σ_{total}), i.e., without baseline correction. Baseline estimation and subtraction are discussed in a subsequent section. This system provides a reliable calibration of the EQCM and a point of comparison for further studies of silver deposition onto a bare platinum surface. Some deviation from ideal masses was observed if large amounts of silver were repeatedly deposited and stripped, e.g., cycling for 1 hour at 2 mV s^{-1}, which is attributed to some damage of the iodine layer.

5.3 Silver electrodeposition onto polycrystalline platinum

Deposition from a 1 mM silver solution onto polycrystalline platinum alone exhibits much more complicated current and frequency responses compared to the iodine-covered surface (Fig. 5.3). There are four regions of interest in the negative-going sweep. The first feature is a small peak (c1) that occurs at 0.70 V; this is followed by a relatively sharp peak (c2) at 0.55 V. A shoulder is found on the tail of this peak around 0.38 V (c3) and finally, a relatively flat section exists negative of 0.25 V that has significant current, indicating a diffusion-limited deposition process (c4). Features c1-c4 were also observed using a platinum wire electrode in the same solution and therefore are not due to edge effects associated with the geometry of the EQCM electrode. Martins *et al.* [75] described similar features (with somewhat different rela-

tive peak magnitudes) using roughened polycrystalline platinum electrodes in sulfuric acid solution.

Fig. 5.3b shows the charge/frequency relation for the same negative-going sweep. The labeled regions correspond to the features emphasised in the voltammogram. The mass change corresponding to peak c1 is only 39 ± 4 g mol^{-1}. The potential at which this peak occurs overlaps considerably with the Pt oxide stripping peak shown in Fig. 2.3 (page 9). The mass change indicates a process different from the simple reduction of Pt oxide by the following mechanism

$$PtO(s) + 2e^- + 2H^+ \rightarrow Pt + H_2O \tag{5.2}$$

which would result in a mass change of 8 g mol^{-1} in the absence of anion effects [76]. The mechanism responsible for peak c1 must therefore involve the heavier silver or perchlorate species (107.87 and 99.45 g mol^{-1} respectively). Silver deposition occurs on unoxidised metal surfaces and is likely to form immediately after the oxide reduction produces free Pt sites. This process is represented by the following equation:

$$Pt + Ag^+ + e^- \rightarrow PtAg(ads) \tag{5.3}$$

The overall process of reaction 5.2 followed rapidly by reaction 5.3 (in a 1:1 ratio) would result in a mass change of 30 g mol^{-1}, which is reasonably close to the mass change observed throughout the central region of this peak. Experiments varying the upper potential limit were carried out in an attempt to decouple Ag deposition from oxide reduction. It was apparent that removal of the UPD layer was not complete before oxidation of the surface began, which led to ongoing silver deposition on the surface with successive cycles. Completion of the underpotential deposition of the one monolayer (ML) of silver implied by reactions 5.2 and 5.3 requires passage of 891 μC cm^{-2}. This value corresponds to the sum of the assumed charge for the first ML of Ag (205 μC cm^{-2}) and the experimentally determined charge required for oxide

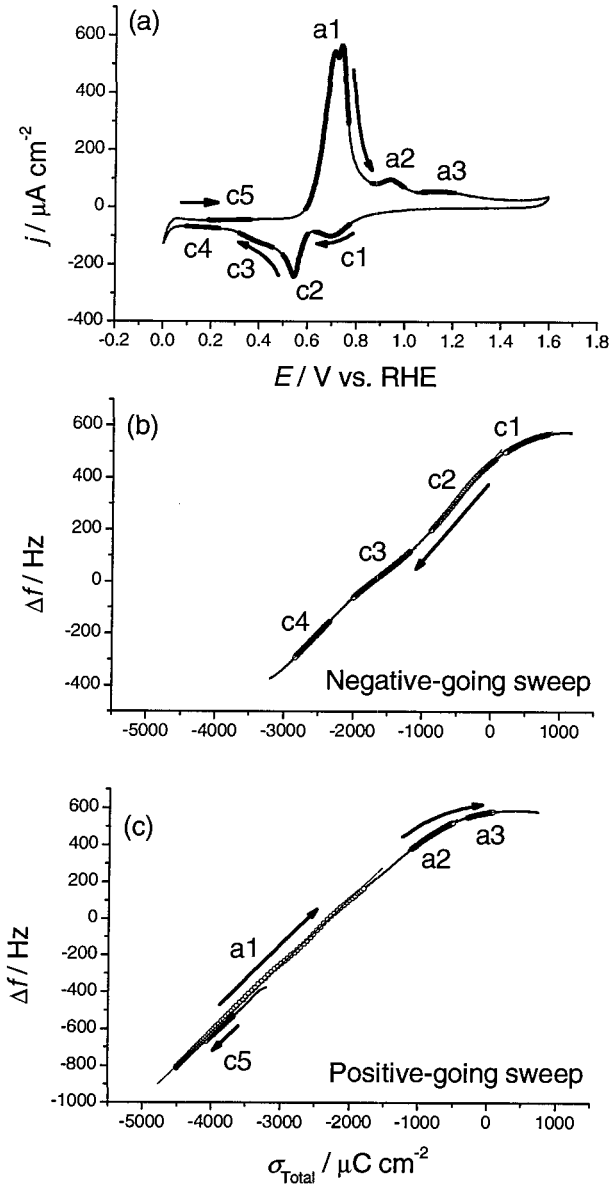

Figure 5.3: Frequency vs. charge density analysis for silver deposition onto bare Pt. a) Cyclic voltammogram for the bare EQCM Pt electrode in 0.5 M $HClO_4$ + 1 mM Ag^+, 20 mV s^{-1}. b) Frequency vs. charge for the negative-going potential sweep. Emphasised sections correspond to the highlighted regions in a). c) Frequency vs. charge for the positive-going potential sweep.

reduction (686 μC cm^{-2}). This amount of charge is passed by 0.65 V, late in peak c1. The subsequent charge in peak c1 (150 μC cm^{-2}) amounts approximately to addition of a second monolayer of UPD silver.

Peak c2 shows a mass change corresponding to 90 ± 7 g mol^{-1}. The location of this peak on the potential scale corresponds to the onset of multilayer silver deposition atop the UPD layers that are formed in feature c1. The reversible potential for multilayer deposition is 0.605 V vs. RHE in this solution, close to the onset of the c2 peak. At the peak of feature c2, an amount of silver equivalent to 2.6 ML has been deposited beyond the UPD layers. It is proposed that the mass value observed arises from the onset of surface smoothing.

There have been several studies performed to elucidate the effect of surface roughness on the response of the EQCM. While the exact origin of frequency shifts in various media is still under debate, there is significant experimental [77, 78] and theoretical [59, 60] evidence that interaction of the surface with the surrounding solution results in an apparent 'mass loading'. This mass loading depends upon the microstructure of the surface, with rougher surfaces exhibiting larger downward shifts of the oscillator frequency. Yang *et al.* [77] have presented images of the surface of an unpolished oscillator that indicate significant surface roughness. Urbakh and Daikhin [59, 60] have shown that the resonant frequency of the EQCM shifts to lower values in the presence of both 'slight' and 'strong' surface roughness. Furthermore, in their theoretical treatment they have shown that the resonant frequency can increase if the adsorption of surface species leads to a decrease in surface roughness. In the case shown here, the initial deposition of multilayer silver in small depressions in the surface could lead to a smoother surface and an increase of the resonant frequency, i.e., an apparent mass smaller than the ideal silver mass. A discussion of the type of surface roughness that would be affected by the amounts of silver discussed here will be presented shortly.

Peak c3 is a shoulder on the tail of peak c2. The mass change observed during this

portion of the sweep is 66 ± 5 g mol^{-1}. This marked reduction in mass is attributed to further smoothing of the surface as the silver fills in larger depressions in the surface. Feature c4 is the diffusion-limited deposition of bulk silver. The mass response observed for this feature is 85 ± 4 g mol^{-1}, still well below what might be expected for silver deposition (108 g mol^{-1}) but greater than the value observed for feature c3. The increase in observed mass compared to feature c3 indicates a decrease in the relative change in surface roughness at this point in the deposition. It should be noted that in this system, an absolute determination of the level of surface roughness is not possible. Increases (or decreases) in the resonant frequency of the oscillator can only serve to reflect a change in surface roughness. With this in mind, further evidence for this rougher-to-smoother transition is provided by the mass change observed in the early stages of the positive-going sweep. Continued reduction in feature c5 shows a mass change of 105 ± 12 g mol^{-1}, corresponding within the error limit to silver deposition alone onto an electrode with a constant roughness. By feature c5, the charge passed corresponds to $\sim$ 20 ML of silver over the UPD layers. This is almost twice the amount of silver deposited at feature c3. As a further test of the smoothing hypothesis, the observed mass was monitored while holding at a potential in the c3 feature. Fig. 5.4 shows that the mass determined by analysing 20 s intervals of the constant potential trace indicates a continuous change that asymptotically approaches a value close to that of silver. The mass value reached after 120 s (115 g mol^{-1}) is within the error observed for the thicker films formed on the surface, such as that observed for c5. This indicates a transition of the electrode surface to one of constant roughness, reached after the deposition of $18 - 24$ ML.

The silver stripping features a1, a2 and a3 have mass changes of -103 ± 8, -72 ± 3 and -22 ± 2 g mol^{-1} respectively. The stripping process begins abruptly in the a1 region. There is some structure evident in the peak that may indicate more than one process. This feature was not further resolved at slower scan rates and appears to be dependent upon the number of potential cycles applied to the electrode. This

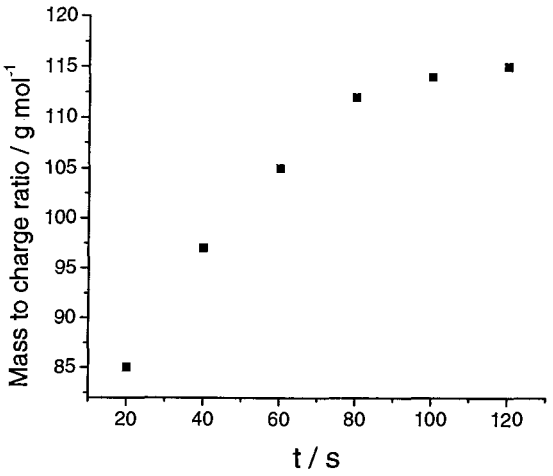

Figure 5.4: Measured mass/charge ratio at 20 s intervals while the the potential was held at the c3 potential (0.417 V). The experiment began with 5.7 ML Ag present (beyond UPD layers). After the first 20 s interval (first point), 11.2 ML were present. After 120 s of holding (last point), 26.2 ML had been deposited.

behavior was not observed when an iodine layer was present (see Fig. 5.1), although the stripping peak observed in the presence of iodine on the surface did tend to broaden over time, perhaps owing to degradation of the iodine layer with repeated cycling. The value of the mass change indicates the stripping of silver from the smoothed film produced by the processes in c2-c5.

Feature a2 indicates that the process of stripping the film from the EQCM electrode significantly roughens the deposit, resulting in a period of increased interaction with the electrolyte and a depression of the resonance frequency. Comparison of the measured masses at points a2 and c3 indicates a comparable surface roughness present at these points in the deposition/stripping process. Finally, region a3 has a mass change corresponding to an oxide transition, coupled with the loss of the last remaining silver from the surface (the reverse of reactions 5.3 and 5.2). The different masses for a3 (-22 ± 2 g mol^{-1}) and c1 (39 ± 4) from the ideal 30 g mol^{-1} may be because the ratio of the oxide to silver reactions differs in the different scan directions.

5.4 Copper electrodeposition onto iodine-covered polycrystalline platinum

In single-crystal studies, copper deposition onto an iodine-covered platinum surface exhibits very similar electrochemical behavior to that of silver [70, 71]. This fact provides an opportunity to study the generality of the effect of an iodine layer on the interactions between metal adatoms and the surrounding electrolyte. Fig. 5.5a shows the cyclic voltammogram of an iodine-covered EQCM platinum electrode in the presence of 1 mM Cu^{2+} and 0.5 M $HClO_4$ supporting electrolyte. One very broad feature (c1) is observed in the negative-going sweep (centered around 0.28 V) prior to the onset of a second feature beginning at 0.18 V (c2) that leads into the hydrogen evolution region. The reverse sweep shows a peak at 0.29 V (a1) followed by a broader peak (a2) that begins around 0.38 V. Evidently the interactions taking place at the iodine-covered surface in the copper-iodine system are more complicated than those found in the silver-iodine system.

Fig. 5.5b shows the charge/frequency changes corresponding to features c1 and c2. The calculated mass change for both of these features is 24 g mol^{-1}. This is lower than the 32 g mol^{-1} mass response expected from the deposition of copper alone according to

$$PtI(ads) + Cu^{2+} + 2e^{-} \rightarrow PtCuI(ads) \tag{5.4}$$

The similar mass responses of peaks c1 and c2 suggest similar surface processes. The charge under peak c1 corresponds to the deposition of the equivalent of 1.6 ML of copper (more than a full UPD layer) [70]. However, integration of the entire potential cycle shows an imbalance of 187 $\mu C\ cm^{-2}$ (10% of the cathodic charge), with the anodic charge being less than the cathodic charge. The frequency response over several cycles does not show the effects of gradual accumulation of material at the electrode. It appears that a solution-based process likely takes place concomitantly

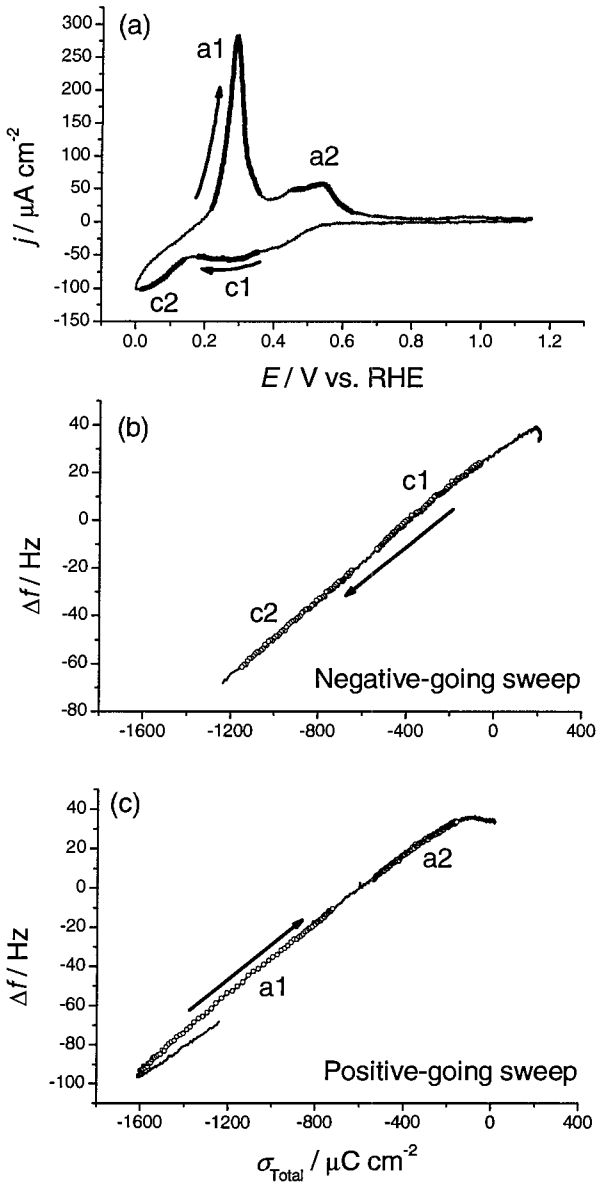

Figure 5.5: Frequency vs. charge density analysis for copper deposition onto iodine-coated Pt. a) Cyclic voltammogram for the iodine-covered EQCM Pt electrode in 0.5 M $HClO_4$ + 1 mM Cu^{2+}, 20 mV s^{-1}. b) Frequency vs. charge for the negative-going potential sweep. Emphasised sections correspond to the highlighted regions in a). c) Frequency vs. charge for the positive-going potential sweep.

with the deposition of the initial copper layer and accounts for the charge imbalance. This leads to an elevated estimate of the c1 copper coverage, and a depressed mass to charge ratio. Assuming the correct UPD charge for c1, the recalculated mass is $24 \times 1.6 = 38$ g mol^{-1}, closer to the expected mass. Note, however, that the corresponding stripping feature a2 also has a depressed mass, for which an analogous explanation in terms of an accompanying solution process is not viable. Feature c2 accounts for overpotential deposition of a further 1 ML (uncorrected) of copper (the reversible potential in this solution is 0.147 V, which lies just positive of the c2 current wave, confirming the UPD nature of c1).

Complications related to reactivity of the iodine layer are also likely. Previous studies using scanning tunneling microscopy [74] have revealed the formation of three-dimensional copper islands during both single monolayer (atop UPD) and multilayer deposition onto iodine-coated platinum single crystals. It is likely that this also occurs on the polycrystalline surfaces studied here. In the analogous copper/chlorine system studied by Marković *et al.* [79], the loss of 0.1 ML of chlorine was observed. In the present case, displacement of one iodine atom into solution (as iodide) for every seven deposited copper atoms would result in a measured mass change of 21 g mol^{-1}, providing an alternative explanation for the depressed mass. However, this should also lead to a fairly rapid degradation of the iodine coating over many cycles, which was not observed. Probably, the 3-D Cu islands formed interact in a complicated way with the electrolyte. The production of Cu^{+}(aq) was also observed during UPD of Cu^{2+} in the presence of Cl [79], and may be a contributor to the excess cathodic charge observed here. However, the higher mass to charge ratio accompanying deposition from Cu^{+} (63.55 g mol^{-1}) was not observed in the EQCM response. Evidently, the disruption of the iodine layer and the presence of a superimposed cathodic solution reaction make copper deposition on iodine-covered Pt far from an ideal system.

Feature a1 corresponds to a mass of 30 g mol^{-1}, very close to the value expected for the stripping of copper from beneath the iodine layer (the reverse of reaction

5.4). The sharpness of feature a1 in this system and the correspondence to a simple stripping process bears the closest resemblance to the behavior observed in the AgI system. The charge passed during the a1 peak in Fig. 5.5a corresponds to the stripping of 2 ML of copper. This indicates that an amount equivalent to 2 ML of copper are 'protected' from electrolyte interaction as was observed in the silver case. The remaining deposited copper (1.5 ML) is stripped from the electrode over the course of feature a2. This feature corresponds to an observed mass change of 24 g mol^{-1}, equivalent to the response observed in features c1 and c2.

5.5 Copper electrodeposition onto polycrystalline platinum

Fig. 5.6a is the cyclic voltammogram for 1 mM Cu^{2+} in 0.5 M $HClO_4$ in the absence of iodine. The negative-going sweep shows little structure, but there is significant reduction current over most of the sweep, including well positive of the reversible potential. This indicates the slow deposition of UPD copper prior to the onset of bulk deposition negative of the reversible potential. This featureless, slow deposition has been observed for copper deposition onto Pt(111) in $HClO_4$ [79]. Fig. 5.6b shows the charge/frequency shift for this region and for the remainder of the trace (here a sample region has been chosen for analysis, as a 'peak' is difficult to define). The mass response is constant over the entire deposition region bounded by the removal of a small amount of oxide and the evolution of hydrogen). The mass change corresponding to c1 is 26 g mol^{-1}, similar to that observed for deposition of copper in the system with iodine present. Here the slightly depressed mass is attributed to smoothing of the surface brought about by the slow deposition of small amounts of copper. Fig. 5.6b shows that as the potential moves into the hydrogen evolution region, the mass/charge slope decreases noticeably. This feature is attributed to the

fact that the presence of adsorbed hydrogen adds significantly to the charge yet adds very little to the mass change at the surface. This makes accurate determination of the mass per electron difficult in this region of potential.

The positive sweep shows three features labeled a1, a2 and a3. Features a1 and a2 both show mass changes of 26 g mol^{-1} (Fig. 5.6c). This indicates that the removal of the film deposited in the negative-going sweep begins to slightly roughen the film deposited in the negative-going sweep. It is interesting to observe that feature a1 in this system occurs at a similar potential to feature a1 in the CuI system. However both the current density and the peak sharpness are noticeably reduced in the bare platinum system. As well, for this particular feature, the mass change corresponds to a simple stripping process only in the presence of the iodine 'blocking' layer, as observed in the silver iodide system as well. The final peak (a3) in the positive sweep shows a mass change of 31 g mol^{-1} as shown in Fig. 5.6c. This indicates that the removal of the last remaining copper on the surface contributes negligibly to a change in surface roughness, as might be expected for removal of a UPD layer.

5.6 Further discussion of mass responses

The electrodeposition of silver on iodine-covered Pt gives a frequency change that agrees with the prediction of the Sauerbrey equation within the measurement error. It can therefore be used as a calibration system for a Pt-covered quartz crystal. The ideal mass for silver is measured over a large coverage range, from a fraction of a monolayer to more than eleven monolayers. This ideal behavior is attributed to the fact that the deposition gives a smooth deposit with the iodine layer constantly exposed to the electrolyte, i.e., the iodine interactions with the electrolyte are substantially the same whether the underlayer is Pt, submonolayer Ag or multilayer Ag.

The same ideal behavior is not found when silver is deposited in the absence of the iodine monolayer. The UPD monolayer deposition is concerted with oxide

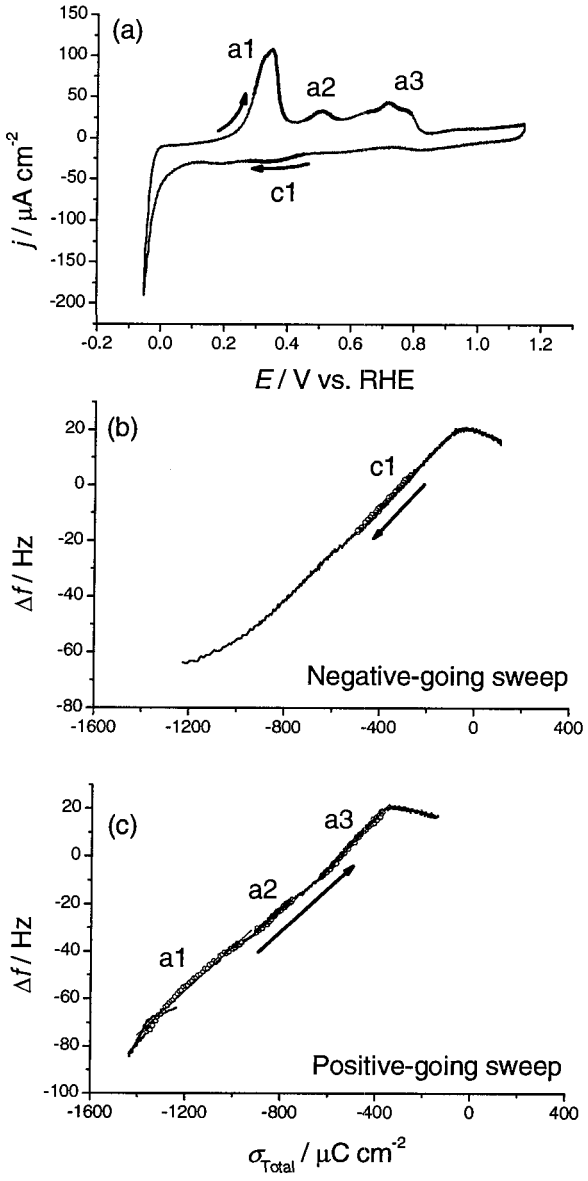

Figure 5.6: Frequency vs. charge density analysis for copper deposition onto bare Pt. a) Cyclic voltammogram for the bare EQCM Pt electrode in 0.5 M $HClO_4$ + 1 mM Cu^{2+}, 20 mV s^{-1}. b) Frequency vs. charge for the negative-going potential sweep. Emphasised sections correspond to the highlighted regions in a). c) Frequency vs. charge for the positive-going potential sweep.

reduction (which is suppressed in the iodine system), and the measured mass can be explained as a combination of these two processes. For the early stages of multilayer deposition, the apparent mass is less than the silver mass. After deposition of 20 ML, the apparent mass is again equal to the ideal silver mass. This region of apparently low mass is attributed to a rougher-to-smoother transition, as shown theoretically by Urbakh and Daikhin [59]. This is suggestive of a 'filling-in' mechanism, with the initial deposits of silver occupying depressions on the initially rough electrode. As the amount of silver increases, the deposit reaches a uniform roughness. In the iodine system, 3-D growth is suppressed in favor of layer-by-layer growth: the iodine acts as a surfactant that promotes layer-by-layer (van der Merwe) growth. Such use of surfactants to promote epitaxial growth is known for other systems, e.g., [80].

The changes in the EQCM response with relatively small amounts of silver deposited bring into question the scale of surface roughness that would be affected by the amounts of deposition presented here (in the absence of iodine). It is clear that for relatively large scale features on the surface (hundreds of nanometres in height and breadth), the equivalent of 20 ML of silver would be insufficient to completely fill the valleys between these features. The fact that the CVs (e.g. Fig. 5.3a) show signs of hydrogen reduction points to the fact that areas of the surface may still contain exposed platinum. However, smaller-scale roughness on these larger features may be significantly affected by monolayer amounts of deposited metal. Each of the electrodes was cycled repeatedly in electrolyte alone prior to introduction of metal ions into the solution. This process of repeated cycling through several oxidation and oxide reduction cycles has been shown to significantly roughen Pt(111) surfaces [81,82]. The surface roughness evolved through this process shows features on the order of nanometres. Similar features are likely created on the polycrystalline electrodes used here. It is reasonable then that several scales of surface roughness are likely present on the electrode surface and the deposited silver results in an appreciable smoothing of the smaller-scale features. Additionally, smoothing of small scale roughness may

also take place at such features as dislocations and grain boundaries that would be numerous on the polycrystalline surface.

The results for the deposition of silver on bare Pt agree with those reported by Vatankhah *et al.* [63]. They showed that the mass response for silver on platinum under cycling conditions did not correspond to that of silver alone until a film thickness of 7 ML was achieved. They also found non-ideal behavior for other deposition conditions, e.g., by potential step experiments. Although they do not correlate all their data in terms of thickness, an examination of their data suggests that ideal behavior is consistently found for thicker deposits, as shown here.

The data presented here have not been corrected for double-layer charging. This correction will reduce the charge and therefore increase the mass to charge ratio. Some component of the less-than-ideal masses might therefore be due to omission of this correction. This correction is easily made for the case of the silver-iodine system. Fig. 5.1a shows the current response for an iodine-covered electrode with and without silver present. Subtraction of the current measured with the iodine layer alone (the dotted line in 5.1a), which is similar to the subtraction of a double layer current, results in a difference of 1% or lower in the calculated mass for both the deposition and stripping processes, much less than the error in replicate measurements.

Subtraction of a baseline current for the iodine-free systems is more problematic, since the double-layer charging currents are typically larger, e.g., for the electrolyte alone on the bare platinum electrode (Fig. 5.3). However, estimation of the magnitude of this current is difficult outside of the 'double layer region' ($0.25 - 0.7$ V). As well, the presence of the metal cation alone changes the structure of the metal/solution interface, even without considering the change caused by the metal deposit. The data were analysed using various assumptions about the double layer current baseline. Generally the corrections are small, but in many cases a different assumption about the baseline location leads to a change in the measured double-layer charge of the same order of the double-layer charge itself. Rather than making corrections of questionable

significance, the raw, uncorrected data has been presented. Methods exist that could perhaps resolve this issue, e.g., impedance measurements, but this goes beyond the scope of the present work, which simply seeks to demonstrate significant interactions between the depositing metal atoms, the electrode surface and the solution.

Another corruption of the numerical value of the mass can occur in sharper peaks, such as the stripping peak in Fig. 5.2a (frequency response shown in 5.2c), which shows a slight deviation from linearity that was not observed for the deposition step. This is likely an artifact from insufficient data sampling for accurate charge integration or from slow time response of the frequency; it appears for all the sharper peaks, and is a small effect, leading to a mass error of only about 2 g mol^{-1}.

Adsorption of water on platinum [83–86] and silver [87, 88] surfaces has been studied and could also lead to masses smaller than the silver mass. If water is adsorbed on the two monolayers of UPD silver, but not on the multilayer silver, then the first multilayer deposition will have less than the silver mass, e.g.,

$$PtAg_2(H_2O)_y + xAg^+(aq) + xe^- \rightarrow PtAg_{2+x} + yH_2O \tag{5.5}$$

has a mass/charge ratio of $(xM_{Ag} - yM_{H_2O})/x$. For deposition of one layer of silver on a surface precovered with one water molecule per silver atom (an unrealistically high coverage) the mass change reduces from 108 g mol^{-1} to 90 g mol^{-1}. More silver deposition increases the mass, in contrast to the experimental situation, where smaller masses are seen well into multilayer deposition. Furthermore, this explanation cannot reasonably explain a mass change as low as the 66 g mol^{-1} observed for peak c3.

Similarly, the desorption of adsorbed perchlorate anions was examined as a possible explanation for the reduced mass observed in the absence of iodine on the surface. A 2:1 ratio of silver deposition to perchlorate desorption would result in a mass change of 58 g mol^{-1}. While this is similar to the lowest masses observed, it is also represents a significant coverage of perchlorate, which is generally believed to be weakly

interacting with the platinum surface. It cannot be ruled out that differential desorption of water and adsorbed anions may be occurring in addition to smoothing effects; however, considering the nanostructure of the surface and the amounts of adsorbed species required to solely explain the mass deviations, the conclusion is that roughness is essential to explain the data.

For the Cu system, masses less than the Cu mass occur even for the iodine-covered surface. While one stripping peak (a1) indicates the ideal situation observed in the silver case, the exact cause of the depressed mass in other regions is more difficult to explain. These findings apparently reflect the more complex interactions between the copper and the iodine film, as have been observed in previous electrochemical [79] and probe microscopy [74] studies.

5.7 Conclusions

Electrodeposition of metal cations is significantly affected by interactions between the surface and the solution brought about by changes in surface roughness accompanying the film deposition. This has been demonstrated through a comparison of silver and copper deposition onto both bare and iodine-coated electrodes. For silver, the cyclic voltammogram of the coated electrode in supporting electrolyte is very simple, showing one deposition and one stripping process in the negative- and positive-going sweeps respectively. In addition, the mass change observed corresponds very well to the mass of silver in both cases. In contrast, in the absence of the iodine layer, four distinct features are observed in both sweep directions. The mass changes observed for the bare electrode indicate significant smoothing (apparently at the microstructure level) during the negative-going sweep, giving way to a more uniform deposit as the film grows. This indicates that the presence of the iodine layer dramatically simplifies the interactions at the platinum surface, promoting layer-by-layer growth and maintaining a constant level of surface roughness. This system is therefore an

excellent system for *in-situ* calibration of the quartz-crystal microbalance. The generality of this behavior was probed by comparing it with the analogous copper system. For copper, the presence of the iodine layer mediates interactions between the analyte and the electrolyte to a lesser extent due to both the formation of copper islands on the surface and the interaction between the copper and the halogen film. Results for copper deposition onto bare platinum show the effects of slight surface smoothing for early monolayer coverages.

Chapter 6

Iodate electrochemistry at Pt electrodes

6.1 Introduction

The interaction of halide species with metal surfaces has attracted considerable attention in the electrochemical community with investigators using a suite of theoretical [89, 90] and experimental techniques [91]. Interest in halide adsorption has focused both on understanding the fundamental aspects of the structure of adsorbed films and on the effect these films can have on other surface reactions. A large number of studies have examined iodide interaction on Au surfaces with methods including STM [92, 93], laser beam deflection [94], chronocoulometry [95], specular reflection [96], Raman spectroscopy [97], Rotating Ring-Disk Electrodes (RRDE) [98], Low Energy Electron Diffraction (LEED), Auger Electron Spectroscopy (AES) and X-ray Photoelectron Spectroscopy (XPS) [99,100]. The EQCM has also been utilised by a number of groups using polycrystalline gold [101–103], single crystal gold [104], silver [105] and platinum [106].

Regardless of the technique used, the majority of studies have focused on the

interaction of the iodide ion (I^-) with the metal surface. There have been relatively few studies devoted to the interaction of the iodate anion (IO_3^-). Anson [107] studied the electrochemistry of iodate on platinum electrodes to elucidate the role of the surface oxide on iodate reduction. Wels *et al.* performed a comprehensive set of RRDE experiments that proposed several intermediate and solution-based species produced during iodate reduction in acid solution [108]. This study in particular demonstrated the very complicated nature of iodate reduction at platinum surfaces. Gu and coworkers used oxidation of an adsorbed adlayer of iodine to iodate in an effort to simultaneously determine the active area and calibration factor of an EQCM electrode [109]. Additionally, Luo *et al.* [110] studied the effect of iodate on copper dissolution. The EQCM has also been used to examine oscillating reactions that occur for iodate reduction in alkaline solutions [101, 111]. However, an EQCM study to complement the available electrochemical data of iodate on platinum electrodes in acid solution is not evident in the current literature.

Interest in this particular ion came from other studies described in this dissertation that examine the codeposition of silver and iodate to create AgI films (Chapter 7). While the K_{sp} of $AgIO_3$ is quite small (3.17×10^{-8}), it is many orders of magnitude larger than that for AgI (8.52×10^{-17}) [112]. For this reason iodate anions have been employed in experiments involving codeposition. However, during these experiments it has been noted that the interaction of iodate with the EQCM electrode is interesting in its own right. A discussion of these findings is presented in this chapter.

6.2 Iodine adlayer formation

The interaction of the IO_3^- ion with the polycrystalline Pt surface was monitored using CV and the EQCM. Fig. 6.1 shows the cyclic voltammetry traces for IO_3^- at 2 concentrations (0.2 mM and 1 mM) on polycrystalline Pt in 0.5 M $HClO_4$ supporting electrolyte. All of the features of the CV increase in magnitude with increased

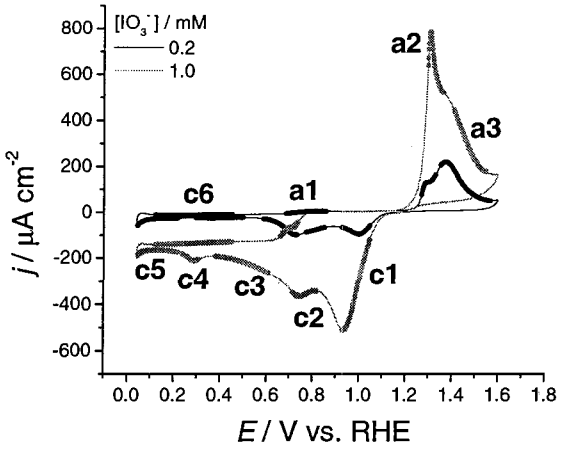

Figure 6.1: Cyclic voltammograms of IO_3^- on Pt EQCM crystals (supporting electrolyte 0.5 M $HClO_4$). Emphasised areas on the traces correspond to features analysed in the frequency vs.charge plots

iodate concentration. The labels and emphasised sections of the traces correspond to analysed areas of the charge/frequency plots for each of the voltammograms.

The charge/frequency plots for the negative- and positive-going sweeps for the 0.2 mM concentration are shown in Fig. 6.2. The negative- and positive-going frequency vs. charge density traces are shown separately because a charge imbalance exists over each potential cycle, resulting in f vs. σ traces that are shifted with respect to each other from cycle to cycle. This charge imbalance indicates the presence of solution-based charge transfer processes during the full potential sweep. These events complicate the analysis of frequency/charge density relationships. Two examples serve to illustrate this point. A completely surface-based process (such as metallic multilayer film deposition) would exhibit the same frequency (or 'mass') to charge ratio regardless of the concentration of the film material (in the absence of other complicating effects such as viscosity or roughness factors). This is true because for every atom or molecule of the film deposited, the frequency shifts by an amount determined by the sensitivity of the microbalance and this is accompanied

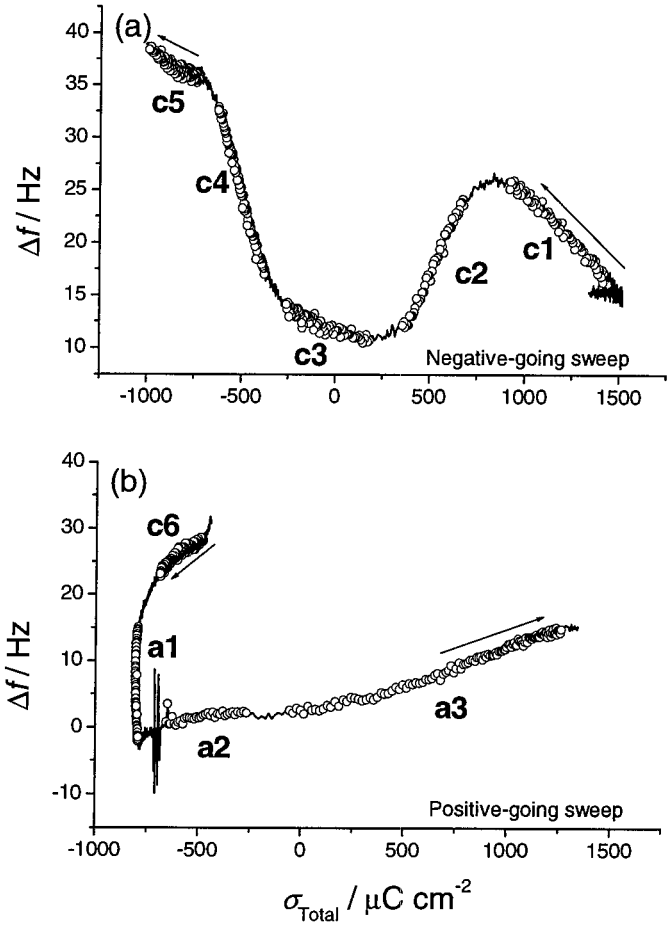

Figure 6.2: Frequency vs. charge density for the negative and positive-going potential sweeps for 0.2 mM IO_3^-. Emphasised sections correspond to the highlighted regions in Figure 6.1.

by a known charge transfer. The ratio of mass to charge is constant under changing concentrations or rates for the particular surface reaction. This case results in a region of constant (non-zero) slope on the frequency vs. charge density plot. In the other extreme, the frequency change is constant (at zero) for a completely solution-based reaction as the mass loading does not change at all during the reaction although charge transfer takes place. This type of reaction produces a flat region in the frequency vs. charge density plot. The intermediate case (a surface-based reaction concomitant with a solution-based reaction) results in a depressed value of the expected mass to charge ratio if both of the processes are similar in nature (both reduction or both oxidation). It should be noted that without a calibration in which the exact ratio of the surface to solution-based reaction rates are known, it is difficult to be quantitative in assigning a ratio to different features in the CV. However, in a qualitative sense a significant amount of information can be deduced using the EQCM that could not be assessed from cyclic voltammetry alone.

A charge imbalance exists at both concentrations of iodate shown in Fig. 6.1. Integration over the entire cycle reveals an imbalance of -573 μC cm^{-2} for the 0.2 mM case (this is 20% of the total charge passed) and -11000 μC cm^{-2} for the 1 mM case (59% of the total charge passed). This indicates a significant amount of solution-based reaction occurring in both systems. The situation is further complicated due to overlapping features. Fig. 6.1 clearly shows several peaks running into one another (quite pronounced at higher concentrations). The use of the EQCM is advantageous here as the frequency vs. charge density plot is capable of indicating changes in the reactions taking place much more easily than can be done using CV. For this reason, locations of the features of the iodate and electrolyte interactions with the Pt electrode (c1 etc.) have been determined from the frequency vs. charge density plots (see Figs. 6.2 and 6.3). Fig. 6.3 shows the frequency vs. charge density relations for the negative and positive-going sweeps for the 1 mM iodate case.

In this higher concentration case it is easier to see the distinct portion of the

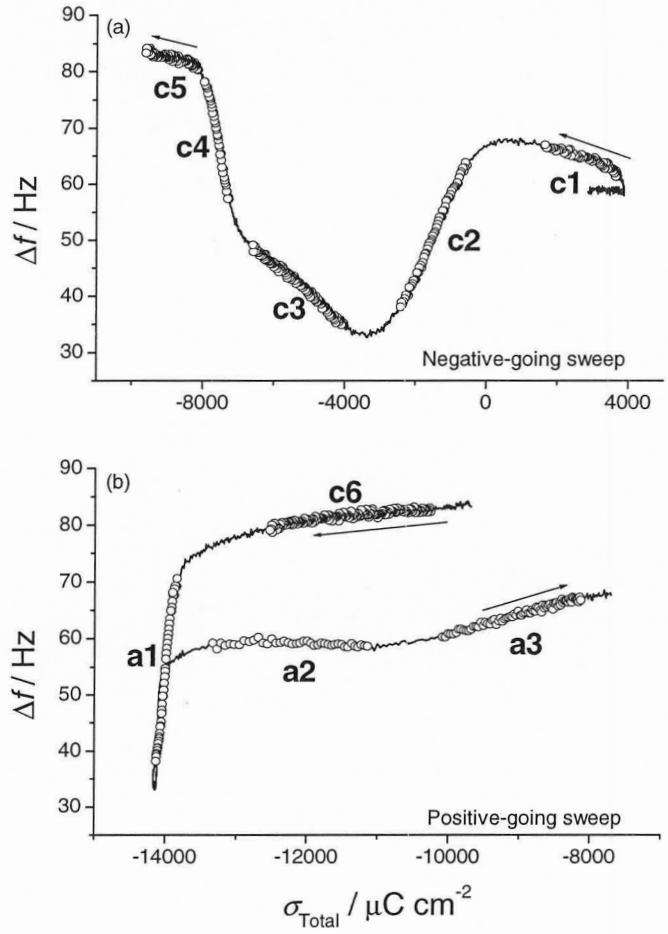

Figure 6.3: Frequency vs. charge density for the negative and positive-going potential sweeps for 1 mM IO_3^-. Emphasised sections correspond to the highlighted regions in Figure 6.1.

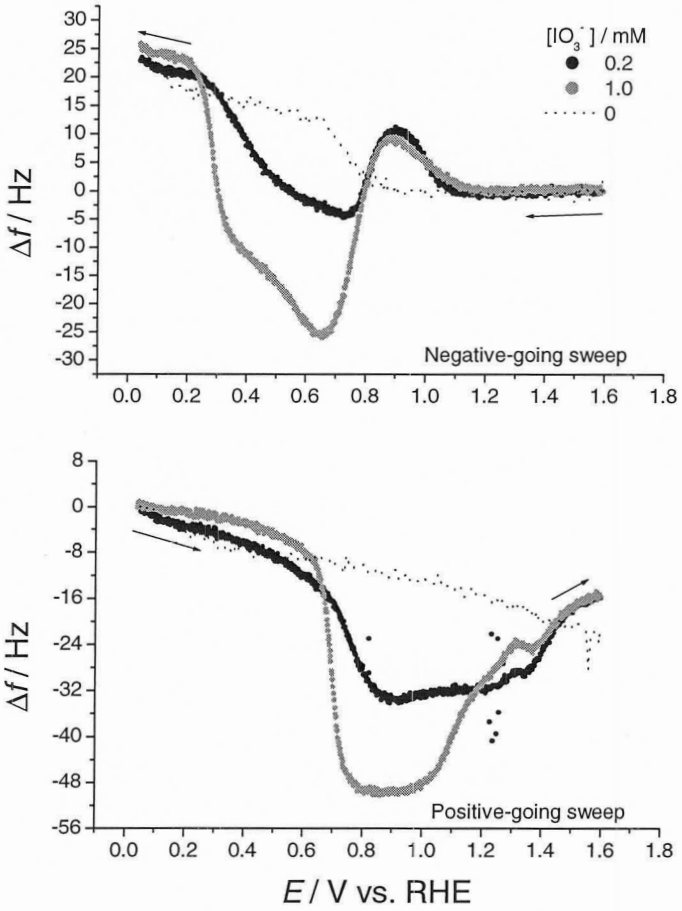

Figure 6.4: Frequency vs. potential traces for 0.2 and 1 mM iodate on polycrystalline Pt. The dotted line is a typical frequency vs. potential trace for polycrystalline Pt in supporting electrolyte (0.5 M $HClO_4$) alone.

trace corresponding to region c3. The proposed origins of the features labeled in Figs. 6.1, 6.2 and 6.3 will be discussed shortly. Another measure of the behaviour in the system is given by the absolute frequency shift that occurs over an entire cycle of the potential. For a reversible surface process, the frequency should return to its initial value over one complete cycle. The absolute shifts in frequency as a function of potential are shown for the negative- and positive-going sweeps for both concentrations in Fig. 6.4.

Fig. 6.4 shows that the absolute frequency change over both the negative and positive-going sweeps are independent of the concentration of iodate. Furthermore, comparison with the typical frequency vs. potential trace for the Pt electrode in electrolyte alone reveals that the frequency changes by almost exactly the same amount with or without iodate present. The relative differences mid-sweep in both frequency and charge density for the two different concentrations point to different reaction rates and/or types.

In the negative-going sweep, Fig. 6.4 shows that the frequency remains steady (no mass change takes place) until $\simeq$ 1.05 V when the frequency increases. This indicates a mass reduction at the electrode surface. The figure shows that the mass response is similar in magnitude to the response observed during oxide reduction on a Pt electrode in electrolyte alone. This process is represented in equation 6.1.

$$PtO(s) + 2e^- + 2H^+ \rightarrow Pt + H_2O \qquad (6.1)$$

The mass/charge density ratio (or 'mass') for this process is -8 g mol^{-1} in the absence of anion effects [76]. The potential at which this process occurs corresponds to c1 in Fig. 6.1. Table 6.1 summarises the observed mass/charge ratios (Figs. 6.2 and 6.3) and potential regions (Fig. 6.1) corresponding to features c1 through a3 for both concentrations of iodate. At an iodate concentration of 0.2 mM (Fig. 6.2), the observed mass change for this process is -5.1 $\pm$ 1.1 g mol^{-1}. At 1 mM, the mass

Feature	E range (0.2 mM) (V)	Mass/charge (g mol^{-1})	E range (1 mM) (V)	Mass/charge (g mol^{-1})
c1	1.05 - 0.926	-5.1 ± 1.1	1.05 - 0.927	-1.1
c2	0.851 - 0.771	12.2 ± 1.0	0.820 - 0.715	7.0
c3	0.733 - 0.588	-5.2 ± 2.7	0.609 - 0.377	-2.6
c4	0.500 - 0.296	-22.0 ± 3.0	0.308 - 0.238	-15.6
c5	0.219 - 0.046	-4.3 ± 2.0	0.218 - 0.046	-1.0
c6	0.120 - 0.452	6.4 ± 1.0	0.119 - 0.451	1.0
a1	0.685 - 0.859	NA	0.659 - 0.736	NA
a2	1.27 - 1.33	1.2 ± 0.2	1.30 - 1.36	0
a3	1.35 - 1.57	3.2 ± 1.7	1.41 - 1.55	1.7

Table 6.1: Potential ranges and measured mass to charge ratios for features observed in the cyclic voltammograms of 0.2 and 1 mM iodate solutions.

drops to -1.1 g mol^{-1}. The absolute frequency change at both concentrations is very similar (Fig. 6.4). This points to a surface-limited process being responsible for the frequency shift. It is reasonable that the process occurring in both instances (near 1.0 V in the negative-going sweep) is the reduction of the Pt oxide. It has been shown [76,107,108] that oxide formation is hindered in the presence of halogen atoms and that the halogen atoms can become incorporated into the growing oxide film. In this case, the onset of oxide formation is shifted considerably at both concentrations of iodate (above 1.2 V in both cases compared to the onset at $\simeq$ 0.8 V in electrolyte alone). The onset of reduction of the Pt oxide is likewise observed to be shifted positive from the electrolyte alone value of $\simeq$ 0.7 V to $\simeq$ 1.1 V in the presence of iodate at both concentrations.

There are several possible reactions that could be taking place in this range of potential involving iodate species. One or more of these processes could be responsible for the deviation of the expected mass from that corresponding to the simple reduction of the Pt oxide The adsorption of I produced in the reduction of iodate follows reaction 6.2.

$$Pt + IO_3^- + 5e^- + 6H^+ \rightarrow PtI(ads) + 3H_2O \qquad (6.2)$$

This reaction occurs at 1.13 V and 1.14 V for 0.2 mM and 1 mM iodate concentration respectively in this solution. These quoted potentials have been calculated from the standard reduction potentials and account for the activities of the ions in solution and the use of an RHE reference electrode. The mass change expected for this process alone is 25.4 g mol^{-1}. The reduction of iodate to form iodine is given by the following reaction:

$$2IO_3^- + 10e^- + 12H^+ \rightarrow I_2 + 6H_2O \tag{6.3}$$

The reduction potential for this process is 1.10 V and 1.11 V for 0.2 mM and 1 mM iodate concentrations respectively in this solution. This process would contribute to the charge passed at the electrode but would not affect the frequency without specific adsorption of the I_2 molecule. Previous work [107, 108] has suggested that $I_2(aq)$ is formed in the double layer region as an intermediate in the reduction of iodate to iodide. The I_2 formed in this process is thought to be further reduced at potentials negative of 0.75 V.

The reduction of iodate can generate both the adsorbed and solvated forms of iodine. The reaction for the solvated species is given by:

$$Pt + IO_3^- + 6e^- + 6H^+ \rightarrow Pt + I^- + 3H_2O \tag{6.4}$$

The standard reduction potential for this reaction is 1.07 V. By definition, this process only contributes to charge passed (adsorbed I is accounted for in reaction 6.2) and should not affect the frequency of the electrode. The depressed mass observed in the c1 feature for both iodate concentrations appears to involve reaction 6.4, which may in turn result in the formation of $I_2(aq)$ after reaction with IO_3^-. There has been a considerable amount of attention focused on the role of the platinum oxide in iodate reduction [107, 108], with the consensus being that iodate reduction is catalysed in the region corresponding to oxide reduction.

Neither reaction 6.4 nor 6.2 can occur before a Pt site is opened up via reaction

6.1. Reactions 6.1 and 6.4 occurring in a 1:2 ratio would produce an observed mass change of -1.1 g mol^{-1}. This value is in good agreement with the mass change observed in the 1 mM solution for feature c1. The mass closer to that of oxide reduction alone observed in the 0.2 mM solution (-5.1 ± 1.1 g mol^{-1}) indicates that reaction 6.4 is involved to a lesser extent. Reactions 6.1 and 6.4 occurring in a 5:1 ratio would produce a -5 g mol^{-1} observed change in mass, very close to the mass found in the 0.2 mM solution. Wels *et al.* [108] estimated a 3:1 ratio for 0.5 mM IO_3^- in 0.5 M H_2SO_4.

It is instructive to consider what mass changes would occur in the absence of I^- production. If a newly formed Pt site was immediately occupied by an adsorbed I atom (reactions 6.1 and 6.2 in a 1:1 ratio), the observed mass change would be $\simeq 16$ g mol^{-1} (mass *increasing*). This is quite different than the mass observed at either concentration. Reaction 6.1 serves to drive the mass change down due to the loss of surface oxide. Reaction 6.2 occurring in a 1:10 ratio with reaction 6.1 would produce the observed mass of -1 g mol^{-1} for the 1 mM case and a 1:25 ratio would be required to produce the observed mass in the 0.2 mM case. Note that these would require the complete absence of the production of the solvated iodide ion. This hypothesis also requires strict adherence to the stated ratios of reaction. If two open Pt sites accommodate I adsorption (i.e., reaction 6.2 occurring in a 2:10 ratio with reaction 6.1), the observed mass would jump quickly to 7.8 g mol^{-1}. A 2:25 ratio results in a mass of -2.4 g mol^{-1}. These calculations demonstrate that production of I^- must play a role in the observed mass changes. Without I^- production, a large amount of PtO must apparently be reduced to account for the mass loss. For this scheme to work, the open Pt sites must then remain largely inactive. This seems unlikely at potentials suitable for reactions 6.4 and 6.2 to occur.

The final possibility to examine involves all three processes occurring in sequence (reaction 6.1 followed by 6.4 and followed by 6.2). This process would generate a mass change of 8.5 g mol^{-1} and the site would be blocked following reaction 6.2. The

first hypothesis seems most logical: at potentials down to $\simeq$ 0.92 V (the end of the c1 feature), the oxide is being reduced and the open sites serve as reaction centres for the production of solvated iodide species. This agrees well with previous findings that found a direct correlation between iodate and oxide reduction on platinum [107]. As the concentration of iodate increases in the solution, the rate of production of iodide solution species appears to increase. It should be noted that another mechanism for iodate reduction has been proposed [108, 113] that involves faradaic charge transfer to produce IO_2^-, which could affect the response of the EQCM. The production of I^- seems straightforward; however, the findings presented show no mass or electrochemical evidence that would support direct I^- adsorption at the electrode surface.

Feature c2 marks a change in both the absolute frequency shift and the mass/charge ratio at both concentrations. This change reflects the formation of an iodine adlayer on the Pt surface that has been exposed after the reduction of the oxide has occurred (c1). The mass changes calculated for feature c2 in the presence of 0.2 mM and 1 mM iodate are 12.2 ± 1 g mol^{-1} and 7.0 g mol^{-1} respectively. The potentials of feature c2 at both concentrations are similar. The absolute frequency change indicates that the surface process involving mass loading on the electrode reaches a maximum in the lower concentration system compared with a continued mass loading observed at 1 mM (Fig. 6.4). Therefore the formation of the iodine layer in the 0.2 mM solution is not limited by surface area at the potential corresponding to the end of c2. In the more concentrated solution the mass loading continues, indicating the formation of a more complete layer. This point will be discussed further.

While multilayer iodine films have been reported [92, 97, 114], they have generally been developed under higher concentrations using KI solutions. Figure 6.5 shows that at both concentrations of iodate discussed here, holding the potential at 0.4 V during addition of iodate to the electrolyte solution results in equivalent and stabilised absolute mass changes over time at both concentrations. This demonstrates that the

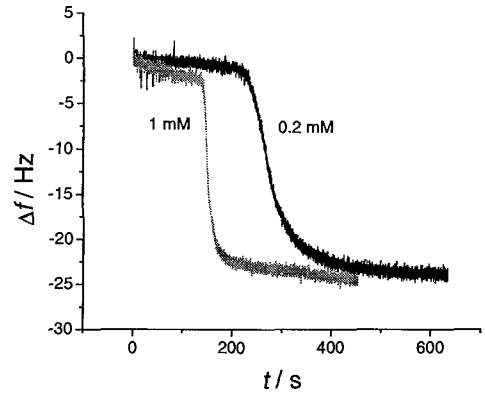

Figure 6.5: Frequency response for iodine adlayer formation on Pt in 0.2 and 1.0 mM concentrations of iodate. An aliquot of iodate solution was introduced far from the electrode to bring the solution concentration to the desired value. The working electrode potential was held at 0.4 V during the addition and throughout adlayer formation.

extent of the iodine adlayer is surface limited. The mass change accompanying the c2 feature in the 0.2 mM case does not correspond to the simple process of iodate reduction given in reaction 6.2 as the mass is approximately half of that expected for this process alone. There are two possibilities that could account for the observed mass. One involves the 1:1 ratio of reactions 6.2 and 6.4. The expected mass would be 11.5 g mol^{-1} in this case, very close to that observed. Another possibility involves the displacement of adsorbed water from the Pt surface upon formation of the PtI bond outlined in reaction 6.5.

$$Pt(H_2O)_x + IO_3^- + 5e^- + 6H^+ \rightarrow PtI(ads) + (3+x)H_2O \qquad (6.5)$$

This however seems unlikely due to the fact that in order to account for the observed mass change, one iodate would have to displace four water molecules ($x = 4$, 11 g mol^{-1} mass change). It has been suggested [115] that the EQCM is capable of sensing changes in water structure up to several layers from the electrode surface.

However, the results for the higher concentration system preclude this process alone based on the fact that for a surface-based process the mass/charge ratios should be the same given the assumption that on average, one iodine atom should displace the same number of water molecules. The 1 mM case shows a decreased mass/charge ratio (7.0 g mol^{-1}, Fig. 6.3) and a much greater current density over the c2 feature. For this reason it is proposed that the main process of c2 is the formation of an iodine layer on the platinum and continued solution-based reactions producing I^- or an iodine oxyanion.

Feature c3 represents another distinct change in the surface process occurring in both systems. With 0.2 mM iodate present, the mass/charge ratio is -5.2 ± 2.7 g mol^{-1} and this is reduced to -2.6 g mol^{-1} at 1 mM. This clearly indicates that the electrode experiences a net loss of mass over this potential range. Interestingly, feature c3 appears to begin at a more positive potential in the less concentrated solution although it is also much less pronounced than it is at higher concentrations. For both systems the frequency continues to increase as the potential decreases. This points to a dynamic process at the surface and likely indicates the continued formation of the iodine layer in both cases.

The adlayer appears to be displacing significant amounts of surface species. The obvious surface species would be adsorbed ClO_4^- anions and water molecules. However, it has been suggested [116] that I_2(aq) near the electrode surface can adsorb to I(ads) species to produce Pt(I^0-I_2). This I_2 is reduced to I^- below 0.70 V, reasonably close to the onset of the c3 feature. Other explanations are also possible. The effect of the iodine adlayer on the point of zero total charge (PZTC) of a platinized Pt plate electrode has been studied by Podlovchenko and Kolyadko [117]. Their findings indicate that the iodine adlayer shifts the PZTC from 0.3 V (vs. RHE in 0.5 M H_2SO_4) to greater than 1.2 V. Similar values should be expected in the system discussed here. As the iodine layer forms on the surface, the PZTC shifts in the positive direction. As this occurs, adsorbed anions on the surface experience a greater driving force away

from the electrode, coupled with the competition for surface sites from the incoming I layer. Reaction 6.6 outlines the displacement of the perchlorate anion from the surface.

$$Pt(ClO_4^-) + IO_3^- + 5e^- + 6H^+ \rightarrow PtI(ads) + 3H_2O + ClO_4^- \qquad (6.6)$$

As written, reaction 6.6 would result in a mass change of 5.5 g mol^{-1} so it is clear that the ratio of ClO_4^- desorption to I adsorption would have to be greater than 1:1 to account for the observed mass loss. Given the high masses of each of the species, the mass change is quite sensitive to the change in ratio. In a 2:1 ratio of perchlorate desorption to iodine adsorption, the measured mass would be -14 g mol^{-1} in the absence of other contributors, much greater than that observed with both concentrations. The perchlorate anion is known to significantly affect the structure of the layers of water close to the electrode surface [115] and the interaction of water and I adlayer films formed by KI on Au(111) has been examined by Lei *et al.* [104]. However, the perchlorate anion is also not expected to be strongly interacting with the surface. It is likely then that the mass loss observed involves a combination of water, anion and I_2 displacement as the iodine adlayer continues to form. The loss of even a very small fraction of a high mass molecule such as I_2 could easily account for the magnitudes of mass changes observed here. As well, the larger shift and more defined c3 region at the higher concentration can be explained by the greater numbers of adsorbed I_2 species that result from a more complete iodine adlayer. Both the increased charge density and decreased mass/charge ratio for the 1 mM system indicate significant contributions from solution-based processes at higher concentrations. The 1 mM case also exhibits the onset of a diffusion-limited current underlying the c3 feature (Fig. 6.1).

Feature c4 exhibits yet another distinct shift in the mass/charge ratios in both systems. The mass loss from the surface is -22.0 ± 3.0 and -15.6 g mol^{-1} at 0.2 mM

and 1 mM iodate respectively. I_2 would be very unstable at this potential and so likely doesn't contribute to the mass change. This feature may point to the further (or enhanced) loss of adsorbed perchlorate anion likely still driven by the shift in the PZTC and competition with the formation of the iodine layer. In both concentrations the current densities appear to be diffusion limited. In the 0.2 mM system the current is low (-25 μA cm^{-2}) during the c4 feature and is considerably higher (-190 μA cm^{-2}) at 1 mM. In this region of potential, the driving force for reduction of several iodine species is strong. Reduction of iodate to I^- is favoured, the I_2(aq) existing in the double layer is unstable here and any remaining adsorbed I_2 is reduced as well. A small, broad peak is also evident near the beginning of the c4 feature in the 1 mM solution. This feature is barely evident in the 0.2 mM CV shown, but was slightly more predominant in other experiments at that concentration.

Features c5 and c6 show relatively minimal activity at the electrode surface with measured mass/charge ratios of -4.3 ± 2.0 and 6.4 ± 1.0 g mol^{-1} for 0.2 mM respectively and -1.0 and 1.0 g mol^{-1} for 1 mM iodate. These features each lie well within the potential region corresponding to hydrogen adsorption and evolution on Pt. Al-Faqeer *et al.* have shown [90] that on iron, the presence of an adlayer of iodine inhibits the hydrogen evolution reaction (HER) but enhances the hydrogen absorption reaction (HAR). It is difficult to make a quantitative prediction about the surface processes taking place here other than to say that the ratios in each case point to limited desorption and readsorption of low mass/charge ratio species corresponding to the end of the negative sweep and the early portion of the positive-going sweep. For both features c5 and c6 the presence of solution-based reactions are indicated by the current density and depressed mass/charge ratio in the higher concentration case compared with the 0.2 mM iodate solution.

6.3 Iodine adlayer removal

Continuing after feature c6, Fig. 6.1 shows that at both concentrations of iodate, the positive sweeps are relatively featureless until the potential reaches $\simeq 0.6 - 0.7$ V. Correspondingly, the frequency response shows only a small decreasing (loading) response over this range for both systems. The 1 mM system exhibits considerable current that appears to be diffusion-limited over this range as well. Coupled with the small mass response, this again points to the predominance of a continued solution-based reduction reaction. This reduction current is also evident in the lower concentration solution but to a much lesser extent. Feature a1 in both systems is characterised by a slow cessation of reduction current and a crossover into oxidation current ($\simeq 5$ μA cm^{-2} at both concentrations). However, this region of potential marks a considerable decrease in the resonant frequency of the electrode. Note that for processes involving no direct charge transfer (e.g. physisorption), the mass/charge ratio is infinite and results in a completely vertical portion of a frequency vs. charge density curve. The a1 region in both solutions exhibits this type of behaviour. The value of the mass/charge ratio measured for this feature is highly susceptible to error. However, it appears clear that this frequency change signals considerable reincorporation of physisorbed molecules onto the electrode surface. This feature perhaps provides the best evidence for the adsorption of I_2. I_2 is no longer reduced above 0.7 V, corresponding very closely with the mass gain at the electrode in both systems.

The differences in the absolute frequency changes (Fig. 6.4) during the positive sweep give an indication of the differences between the iodine films formed at lower and higher concentrations. In the 0.2 mM system, the decrease in frequency occurs slowly while it is an abrupt change in the 1 mM case. This indicates that the iodine film formed at low concentration may be much less complete than the one formed at 1 mM. Reintegration of electrolyte molecules takes place more easily perhaps owing to a greater availability of surface sites; however, there may be relatively fewer sites

for I_2 adsorption due to the less complete layer. In contrast, the higher concentration case points to a more compact film of iodine that provides many adsorption sites for stabilised I_2. This may explain the abrupt change so close to the reversible potential for I_2 reduction. The frequency drop in the 0.2 mM solution is followed only by a small change in the mass/charge ratio (Fig. 6.2) whereas at the higher concentration the downward shift is followed immediately by a steep, positively-sloped section of the mass/charge ratio (see Fig. 6.3 and the $1 - 1.15$ V section of the 1 mM solution in Fig. 6.4). This is likely indicative of oxidation of the film and the accompanying loss of adsorbed surface species.

Features a2 and a3 fall at potentials corresponding to the oxidation of iodine back to iodate. The presence of the iodine film is expected to suppress the oxidation of the Pt surface [76, 107, 108]. These two processes (the reverse reactions of 6.1 and 6.2) couple to result in minimal mass/charge ratios as shown previously. This accounts for the observed ratios of 1.2 ± 0.2 and $\simeq 0$ g mol^{-1} (a2) and 3.2 ± 1.7 and 1.7 g mol^{-1} (a3) observed in 0.2 mM and 1 mM solutions respectively. As before, the higher concentration case shows depressed values of the mass/charge ratio compared with the 0.2 mM case. In this case it is likely due to the oxidation of solution-based iodine species. There is an interesting feature in the absolute frequency change (Fig. 6.4) that corresponds to the first stages of oxidation (a2). The feature is evident in both solutions but is much more pronounced at higher concentration. The feature does not correspond to a significant change in charge density and could point to a slight but specific rearrangement of the film involving physisorbed species prior to complete oxidation. It could, however, also be due to competing reaction rates between electrode and film oxidation.

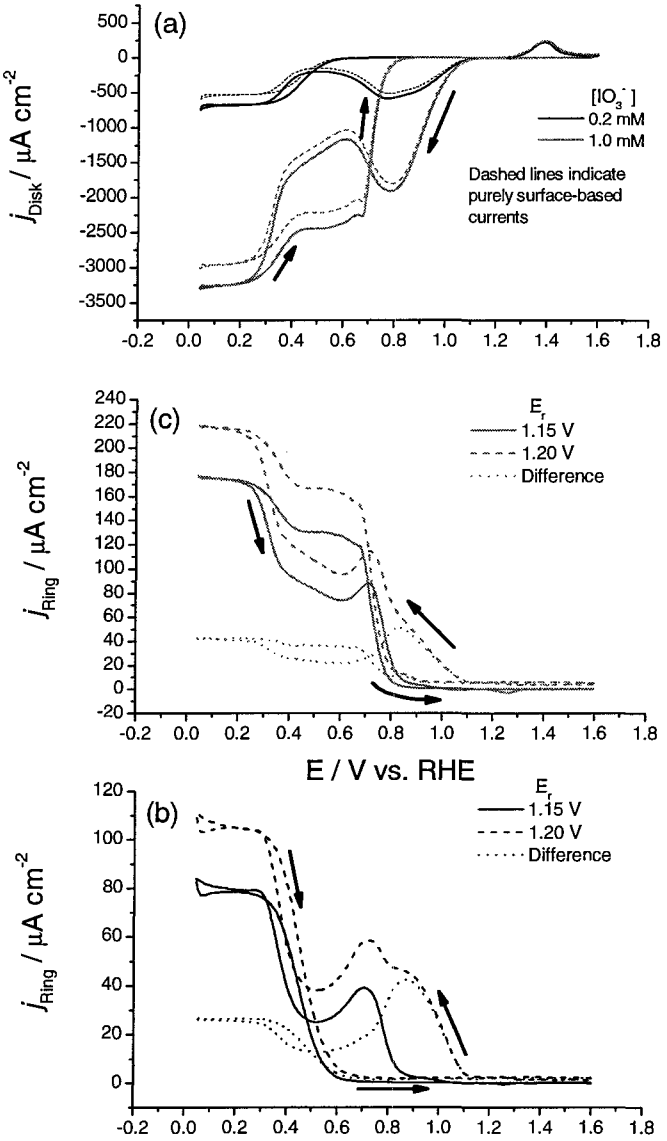

Figure 6.6: RRDE responses for iodate reduction in 0.5 M $HClO_4$. f_{RRDE} = 1000 RPM. a) Disk current density for 0.2 mM and 1.0 mM solutions, ν_{Disk}= 0.020 V s^{-1}. Dashed lines for each trace correspond to current densities of purely surface-based (deposition) reactions. b) Ring current densities corresponding to 0.2 mM IO_3^- solution. c) Ring current densities corresponding to 1.0 mM IO_3^- solution. Ring potentials (E_r) are given in the legends.

6.4 RRDE experiments

Many of the preceding arguments have relied heavily upon the existence of solution-based charge transfer to explain the mass changes observed with the EQCM. To corroborate these findings, RRDE experiments were performed under the same solution conditions discussed above. Wels *et al.* have previously undertaken a comprehensive RRDE study in a very similar system [108] so the results presented here are not exhaustively recounted. Fig. 6.6 shows the RRDE data at both concentrations (0.2 and 1 mM) at a rotation rate of 1000 RPM in all cases. Fig. 6.6a shows the disk current at both concentrations. The features correspond well with the findings of Wels *et al.* Current from solution-based processes is enhanced under the stirring conditions present in the RRDE experiment, which accounts for the discrepancies between these CVs and those shown in Fig. 6.1. Using the nominal collection efficiency of the electrode (22.0%), the current densities due to surface based (deposition) reactions have been determined (using $E_r = 1.20$) and are shown as dashed lines in the figure. The larger difference between the surface-based and 'total' ring currents in the 1 mM solution indicates a greater contribution from solution-based reactions at this concentration, as found using the EQCM.

Fig. 6.6b shows the ring currents recorded over a complete cycle with 0.2 mM iodate present. The traces shown are for ring potentials (E_r) of 1.15 V (solid), 1.20 V (dashed) and for the difference between these two signals (1.20 V − 1.15 V, dotted). The ring potentials employed by Wels *et al.* were 0.52 V and 0.92 V (converted from their SCE reference). In general, the responses of the $E_r = 1.15$ V trace shown here correspond well with the 0.92 V results in [108].

The figure shows that for $E_r = 1.15$ in 0.2 mM IO_3^-, significant current is measured beginning at a disk potential (E_d) of 0.8 V. This corresponds with feature c2 discussed in the EQCM results and interestingly begins as the first cathodic peak in Fig. 6.6a is reaching a maximum. The choice of ring potential here (1.15 V) essentially ensures

that all solution species that have been considered in the analysis would be oxidised back to iodate (see the quoted potentials for reactions 6.2 - 6.4, the closely-spaced oxidation potentials of these processes makes excluding one over another difficult). The solution-based species evolved during c2 was attributed to I^- produced by the direct reduction of iodate. The current peaks at $\simeq 0.7$ V but begins to increase again until it plateaus near the end of the negative-going scan. Wels *et al.* found evidence for I_2(aq) (some of which was subsequently reduced to I^-) for all cathodic features in the CV. The signal for $E_r = 1.20$ V clearly shows a different response, most notably the onset of ring current at 1.1 V. This corresponds well with the first cathodic peak observed in the CV (and c1 in the EQCM studies). The presence of a ring current for this higher value of E_r is attributed to enhanced reaction at the ring due to the catalytic effect of surface oxide that should exist on the ring at this potential. This peak follows the reduction of the platinum oxide film and the beginning of both iodate reduction and iodine adlayer formation. Clearly solution products such as I^- or I_2(aq) are produced here and throughout the negative-going scan. While the presence of IO_2^- has been proposed as a reaction intermediate for iodate reduction [108, 113], it seems unlikely that oxidation of this species makes up a significant amount of the observed ring current due to its instability in acidic solutions [118].

Fig. 6.6c shows the ring current density in 1 mM iodate solution. Most of the features at both values of E_r are similar to those for the lower concentration case with the expected increase in current density associated with higher iodate concentration. There are a couple of notable exceptions. The magnitude of the 1.20 V – 1.15 V ring potential signal in the oxide reduction region (1.1 → 0.8 V) is very similar in magnitude to that for the 0.2 mM case (Fig. 6.6b) despite the increase in concentration. This confirms that the species (I^- and I_2(aq)) detected at this value of E_r are directly related to the process of oxide reduction. The concentration of these solution species appears to be directly related to the amount of oxide, which is surface limited. This explains why the ring currents are similar at both concentrations in

Feature	Predominant Reaction(s)	Remarks
c1	6.1 and 6.4	
c2	6.2 and 6.4 (minimal 6.3)	6.4 increased at 1 mM
c3	6.6, loss of adsorbed I_2	6.6 minimal
c4	6.6	6.6 enhanced
c5	Hydrogen adsorption	
c6	Hydrogen desorption	
a1	-6.6, readsorption of I_2	
a2	-6.2, -6.1	
a3	-6.4	

Table 6.2: Summary of predominant reactions occuring at the electrode surface as determined through EQCM and RRDE experiments. Note that reactions 6.3 and 6.4 are responsible for the reduced masses observed in the EQCM and are enhanced in the 1 mM solution. Negative signs indicate oxidation reactions.

the oxide reduction region. The response during the positive-going scan of E_d shows more structure than in Fig. 6.6b, where the current density quickly diminished by 0.6 V. Under 1 mM conditions there is significant current until 0.8 V, where it abruptly diminishes. This potential corresponds well with the proposed adsorption of I_2 that leads to a significant mass increase as shown with the EQCM results. The increased current preceding this drop may relate to the larger local amounts of I^- and IO_3^- that eventually recombine to form the adsorbed I_2.

6.5 Further discussion

Table 6.2 summarises the results determined in the previous sections. There are several points that require further analysis. The conclusions rely heavily upon the existence of solution-based reactions. Both the RRDE results and the EQCM findings clearly indicate that these processes are appreciable. It is very interesting that the production of I^- outlined in equation 6.4 does not appear to result in the direct interaction of I^- with the electrode surface. This conclusion is reached from two angles. For one, all of the currents observed during the negative-going sweep and for

a good portion of the positive-going sweep are reduction currents. The incorporation of I^- directly from solution implies oxidative adsorption and should produce oxidation currents that are not observed with iodate but have been observed using KI. Several studies [27,114,119] have shown that adsorbed iodine is fully discharged on the metal surface. Secondly, the observed mass/charge ratios are all very low. The mass/charge ratio for adsorption of I^- alone is equal to the molecular mass of I (127 g mol^{-1}). Reduction from oxoiodine species such as IO_3^- involves more electrons and therefore greatly reduces the mass/charge ratios to values much closer to those observed in this study. It has been shown that I_2(aq) and adsorbed I_2 appear to play a significant role in the chemistry near the surface. These species may effectively be acting as sinks for the I^- produced very near to the surface while other I^- ions diffuse away.

The frequency increase observed corresponding to feature c4 might possibly be attributed to the removal of the iodine adlayer instead of the reduction of adsorbed I_2 or the desorption of perchlorate anions as has been presented. The calculated reversible potential for reaction 6.7 is $\simeq -0.005$ V in this electrolyte.

$$I(ads) + e^- \rightarrow I^- \tag{6.7}$$

This is well negative of the potential at which the c4 feature is observed. Furthermore, in separate experiments the desorption of a preadsorbed iodine adlayer has been probed at negative potentials. These studies confirmed that the increase in resonant frequency and reduction current begin approximately at 0 V. For this reason it is clear that the positive shift observed at feature c4 is the result of the loss of relatively massive physisorbed species coupled with the continued adsorption of iodine.

The completeness of the iodine adlayer formed during cycling at both concentrations has been examined. Podlovchenko [117] reported a value of -130 to -140 μC cm^{-2} for a complete iodine adlayer on Pt using I_2 and KI solutions. The total oxidation charges measured in both systems in this work are 2300 and 7500 μC cm^{-2} for

0.2 and 1 mM respectively. Subtracting off the typical oxidation charge associated with Pt oxidation alone (shown in Fig. 2.3, 740 μC cm^{-2}) leaves 1560 μC cm^{-2} anodic charge in the 0.2 mM solution and 6760 μC cm^{-2} in the 1 mM system. These charges are predominantly due to oxidation of the adlayer and solution-based oxidation reactions. The reverse of reaction 6.2 implies 5 μC of charge passed for every μC of I on the surface. So the removal of a complete layer by oxidation to IO_3^- requires $\simeq$ 700 μC cm^{-2}. Close to ten times this amount of charge is passed in the higher concentration case while a little more than two times is passed at lower concentration. It has been shown clearly that solution-based processes play a significant role throughout the deposition and removal of the iodine adlayer. It is reasonable to conclude that since a large portion of the current observed is due to solution-based reactions, the iodine adlayer may be incomplete at lower concentrations while it appears complete after the negative sweep at higher concentrations.

6.6 Conclusions

The behaviour of iodate ions in acidic solution has been studied using the EQCM. Comparison of results using 0.2 and 1mM iodate solutions reveal significant contributions from solution-based reactions throughout the formation and dissolution of the iodine adlayer. Low mass/charge ratios under both conditions indicate formation of I^- or I_2(aq) directly from the iodate anion with no evidence found for direct oxidative adsorption of the I^- ion. Lower mass/charge ratios observed in 1 mM solutions are attributed to the increased rate of solution reactions and the effect of these processes on the EQCM response has been presented. Formation of the iodine adlayer actually causes a net mass loss over the negative sweep. This is explained by a loss of specifically adsorbed water, perchlorate and iodine molecules during formation of the iodine adlayer. The perchlorate ions are likely affected by a shift in the PZTC brought on by the formation of the iodine adlayer.

Chapter 7

Silver iodide films and layered structures

7.1 Introduction

Interest in the production of layered materials by electrodeposition has been intense for many years. In this time, different approaches have been used that can be loosely grouped into two categories: multiple-bath and single-bath processes. Single-bath processes are desirable because they streamline the apparatus and time required to produce the materials. However, control over the chemistry in these systems is also more complicated than in the multiple-bath methods. Early electrodeposited modulated structures focused on alternating metal components. Yahalom and Zadok [120, 121] developed a method of depositing copper-nickel structures from one bath with minimal codeposition by setting unfavourable diffusion conditions for the more noble element. Other groups expanded on this idea [122–124] and incorporated other factors such as galvanostatic techniques [125], electroless displacement [126], altered solution chemistry and pulsing schemes [127]. Several other combinations of metals have also been deposited with these techniques [128, 129].

The past decades have also seen considerable interest in the electrodeposition of compound semiconductors using one-bath and 'two-stage' methods [130]. Films of CdSe [131], CdTe [132,133], and indium compounds [134–136], have all been successfully produced using these approaches. A superlattice composed of CdSe/ZnSe layers was produced by Wei and Rajeshwar using a dual bath method [137]. This followed work from the same group attempting to produce the material from a single bath. In that work it was found that both Cd and Zn were incorporated in all layers [138]. The work presented in this chapter examines the coreduction of silver and iodate to form films of AgI_x ($x < 1$). Application of a pulsed potential sequence is utilised to alter the iodide incorporation over time to produce layered materials of the form AgI_x/AgI_y.

Recently El-Kouedi *et al.* have used a template synthesis method to produce AgI nanorods and AgI/Au heterojunction materials within porous alumina channels [139]. The AgI films produced in their work involved electrodeposition of Ag followed by oxidation of the film in the presence of 1 M KI. Switzer *et al.* have successfully probed the electrodeposition of superlattices incorporating non-metallic constituent layers [140–143]. They successfully created ceramic superlattices based on thallium(III) oxide using both potentiostatic and galvanostatic control in alkaline solution. The structures were modulated based on defect chemistry. Higher overpotentials favoured oxygen vacancies while low overpotentials favoured cation interstitials. Their studies of thallium and lead oxide structures indicated that the abruptness of the interface between layers was heightened under potentiostatic as opposed to galvanostatic conditions [140]. The goal here is to understand the types of silver iodide films that can be formed under different conditions. The different solution conditions and potentials that lead to the largest differences in film structure are exploited to create a superlattice with the desired result being to create a metal/compound superlattice structure.

In situ characterisation of electrodeposited superlattice structures formed from a

single bath is non-trivial. Charge measurements [144] offer one parameter that can be equated with layer characteristics. Here the EQCM is utilised to incorporate mass gain as another parameter to determine the characteristics of both electrodeposited thin films and superlattice structures. The EQCM was used previously to monitor the changes in a galvanostatically formed Cu/Cu_2O superlattice that was produced through spontaneous oscillation [145]. The system presented here demonstrates the usefulness of the EQCM method in monitoring compound thin film and superlattice materials produced potentiostatically. As well, many of the factors that must be considered using this sensitive characterisation technique are demonstrated and discussed.

7.2 Cyclic voltammetry

The salts utilised in the production of AgI_x films were KIO_3 and $AgClO_4$. This choice suppresses the presence of I^- in the silver solution and the inevitable formation of AgI precipitate ($K_{sp} = 8.52 \times 10^{-17}$). The K_{sp} of $AgIO_3$ is 3.17×10^{-8} [112] and the formation of this precipitate in solution can be avoided while still maintaining appreciable concentrations of both Ag^+ and IO_3^-. The majority of experiments reported here showed no signs of precipitate formation (where evident, it is noted in the text). The vanishingly small K_{sp} of AgI ensures the formation of this precipitate for even the smallest traces of I^- in the presence of silver ions. Chapter 6 examined the electrochemistry of iodate alone on platinum EQCM electrodes and showed no evidence of I^- in direct reaction with the surface based on the mass changes observed. Table 7.1 outlines the reactions considered here in the production of AgI_x films. Reactions 7.6 and 7.7 involve I^- and are shown simply as a reference to indicate when the AgI_x films might be destabilised.

Three sets of conditions were explored in terms of the relative concentrations of Ag^+ and IO_3^- for the production of the films: very low (< 0.3 mM) IO_3^- concentration

Reaction	$\Delta_r G^\circ$ (kJ mol^{-1})	E_r (V)	Mass/Charge (g mol^{-1})
7.1. $Ag^+ + I(ads) + e^- \rightleftarrows AgI(s)$	-138	1.20 - 1.25	108
7.2. $Ag^+ + IO_3^- + 6H^+ + 6e^- \rightleftarrows AgI(s) + 3H_2O$	-727	1.16 - 1.17	39
7.3. $IO_3^- + 6H^+ + 5e^- \rightleftarrows I(ads) + 3H_2O$	-588	1.14 - 1.15	25
7.4. $IO_3^- + 6H^+ + 6e^- \rightleftarrows I^- + 3H_2O$	-619	1.07	NA
7.5. $Ag^+ + e^- \rightleftarrows Ag(s)$	-77.1	0.57 - 0.62	108
7.6. $I(ads) + e^- \rightleftarrows I^-$	-4.82	-0.05	-127
7.7. $AgI(s) + e^- \rightleftarrows Ag(s) + I^-$	14.6	-0.15	-127

Table 7.1: Relevant reactions, free energies of reaction, reversible potentials and expected EQCM mass changes for the electrochemical production of AgI_x films. Reversible potential ranges for reactions 7.1 - 7.3 and 7.5 reflect experimental concentrations.

and constant (1 mM) Ag^+ concentration, low ($\leq$ 0.6 mM) Ag^+ concentration and constant (1 mM) IO_3^- concentration, and nearly equal or equal concentrations ($\leq$ 0.6 mM) of both ions. Each of these regimes displayed unique characteristics. Note that each trace for each set of CVs was obtained after several potential cycles under the given conditions. Fig. 7.1a shows the changes in the cyclic voltammetry of a 1 mM Ag^+ solution with increasing IO_3^- concentration (0.06 $\rightarrow$ 0.29 mM). The solid black trace corresponds to silver in the absence of iodate and shows features corresponding to UPD ($\simeq$ 0.7 V) followed by bulk deposition at $\simeq$ 0.6 V during the negative-going sweep. Both of these potential values correspond well with the expected reduction potentials in 1 mM solution. There is an oxidation peak in the positive going sweep starting around 0.5 V.

The CV changes significantly when even a small amount of IO_3^- is present. The trace for 0.06 mM IO_3^- shows a reduction peak at 0.95 V (c1) during the negative going sweep. The peak grows with increasing IO_3^- concentration. This reflects reaction 7.3 (that should be immediately followed by reaction 7.1 in this solution) coupled with the removal of the platinum oxide as has been shown in Chapter 6. The peak at 0.7 V (c2) increases in magnitude in the presence of IO_3^- while the subsequent peak (c3) increases in magnitude and shifts slightly in the positive direction. The nature of

the currents observed here (surface vs. solution-based charge transfer) are discussed shortly. With I adsorbed on the surface via reaction 7.3, reaction 7.1 can take place under a large driving force at this potential. As well, both reactions 7.2 and 7.5 are likely proceeding. During the positive-going sweep, the oxidation peak (a1) shifts slightly negative with increasing IO_3^- concentration. The slight tail observed for this peak with silver alone vanishes at even the lowest iodate concentrations. This could be the result of differences between oxidising silver alone (bulk) versus oxidation of an Ag film with iodine content. Note that the broad peak attributed to Ag UPD film oxidation/oxide formation ($\simeq$ 1.1 V, Chapter 5) also vanishes with iodate present. The peak magnitude initially increases for lower IO_3^- concentrations but at the higher concentrations it returns to a similar magnitude to the baseline silver CV. This sort of behaviour is also observed with the overall peak breadth of a1, which increases initially but decreases at higher IO_3^- values. An oxidation peak (a2) is observed beginning at 1.2 V with iodate present that is not evident with silver alone. The peak grows in with 0.06 mM iodate present and shows a relatively constant magnitude and position at all higher concentrations.

Fig. 7.1b shows the frequency response of the electrode during the negative-going potential sweep. The baseline silver case exhibits relatively simple behaviour (the details are explored in Chapter 5). The frequency begins to decrease corresponding to the onset of UPD silver. The slope of the frequency change increases once the potential corresponding to bulk deposition is reached indicating a more rapid mass gain at the electrode. This mass increase corresponding to silver film formation continues for the remainder of the negative-going sweep. The presence of iodate in the solution significantly affects the mass changes observed at the surface. At the potential corresponding to the iodate peak observed in the CV, the frequency decrease begins. The magnitude of this frequency shift increases with increasing IO_3^-. The frequency decrease continues through the silver UPD region and becomes more rapid at potentials corresponding to bulk silver deposition. Note that in all

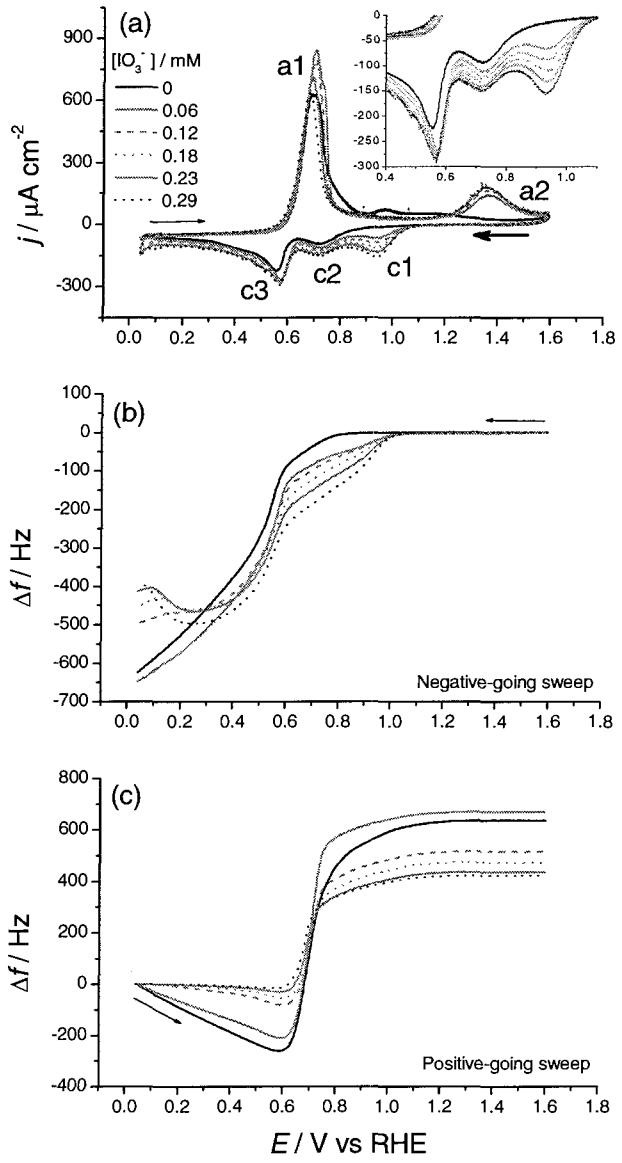

Figure 7.1: Pt EQCM response for silver deposition with varying iodate concentration. a) Cyclic voltammetry in a 1 mM Ag^+ solution with increasing IO_3^- concentration. Concentrations shown in legend correspond to $[Ag^+]$:$[IO_3^-]$ ratios of: 1:0, 16.6:1, 8.3:1, 5.6:1, 4.3:1 and 3.4:1 respectively. $\nu = 0.020$ V s^{-1}. The inset shows peaks c1 - c3 in greater detail. b) Frequency response of the electrode during the negative-going sweep. c) Frequency response of the electrode during the positive-going sweep.

cases the frequency decrease is larger (indicating more material deposited) with iodate present up until $\simeq$ 0.3 V. Negative of 0.3 V, the 0.06 mM iodate solution results in a heavier film through the end of the sweep. In all the other cases, the mass gain at the electrode begins to decrease at more negative potentials and in some cases (0.18 mM and greater), the electrode loses mass near the end of the sweep, indicated by the increase in Δf at negative potentials. This mass loss shouldn't correspond to either reactions 7.5 or 7.6. It is possible that the response indicates the formation of AgI_2^- [146]. The I^- necessary for this product could be produced by reaction 7.4, although a significant amount of iodide would likely be required to produce appreciable amounts of AgI_2^-.

The corresponding frequency shift vs. potential relations for the positive-going sweeps are shown in Fig. 7.1c. The responses are straightforward for all IO_3^- concentrations. At zero concentration, the silver film continues to deposit during the positive-going sweep until the potential reaches 0.6 V. At this point, the frequency rapidly increases and reflects the loss of the silver film from the surface. With the film removed, the frequency remains constant on this scale until the end of the sweep. A concentration of 0.06 mM iodate shows similar behaviour although the magnitude of the frequency increase is slightly lower compared with the baseline silver case At higher iodate concentrations, the mass increase observed during the initial stages of the positive sweep is minimal. The loss of the film from the surface results in a relatively sharp transition in all cases; however, there is a correlation between higher iodate concentrations and earlier onset of film loss. At zero iodate concentration, the minimum of the frequency corresponds exactly with the transition from reduction to oxidation current. As the concentration of iodate increases, film formation continues for a very short duration after the current has become positive. At potentials positive of the major frequency shift attributed to film loss, the frequency shows little change on this scale. This indicates that the oxidation process observed at 1.2 V is largely solution-based and does not reflect significant changes in mass on the elec-

trode surface. The mass response does not indicate the loss of AgI from the reversal of reaction 7.2. Iodine incorporated into the film is apparently predominantly lost along with the silver oxidation peak (a1). This serves as a good indication that the level of iodine incorporation is quite low under these solution conditions. Note that for this positive-going sweep, the total mass lost from the surface is greatest for the combination of 0.06 mM iodate and 1 mM silver. Additionally, the potential window for deposition under these conditions is quite wide, ranging from 0.040 V to 0.600 V.

Fig. 7.2a shows the voltammograms for solutions with a constant concentration of IO_3^- (1 mM) and varied Ag^+ concentration (0.2 $\rightarrow$ 0.6 mM). Again the solid black trace represents the baseline condition in this system corresponding to iodate alone. The features of the baseline case have been discussed in Chapter 6. In brief, the main reduction peak (c1) at 0.95 V is due to reaction 7.3 (coupled with platinum oxide reduction), and is the start of iodine adsorption. The data obtained with the microbalance (Fig. 7.2b and c) suggest that this process continues as the potential is made more negative and apparently involves displacement of physisorbed species from the surface as the film forms (in the potential region of c2 and more negative). The microbalance results also indicate a significant amount of solution-based reaction occurring that does not affect the mass of the electrode (reaction 7.4). During the positive-going sweep, there is a rapid increase in mass at the surface corresponding to the cessation of reduction current at 0.8 V. This has been attributed to the readsorption of water and anions coupled with the removal of the I adlayer. The oxidation features (a1 and a2) beginning at 1.2 V are due to both solution-based oxidation of iodine species back to iodate and the oxidation of the substrate.

Significant changes in the CV are not noticeable until a substantial amount of silver is added to the iodate solution (0.2 mM). This is in contrast to the conditions outlined in Fig. 7.1a. Up to a silver concentration of 0.4 mM, the reduction features remain very similar to the iodate baseline and there is actually a reduction in the current flowing throughout the negative-going scan. The positive-going scan exhibits similar

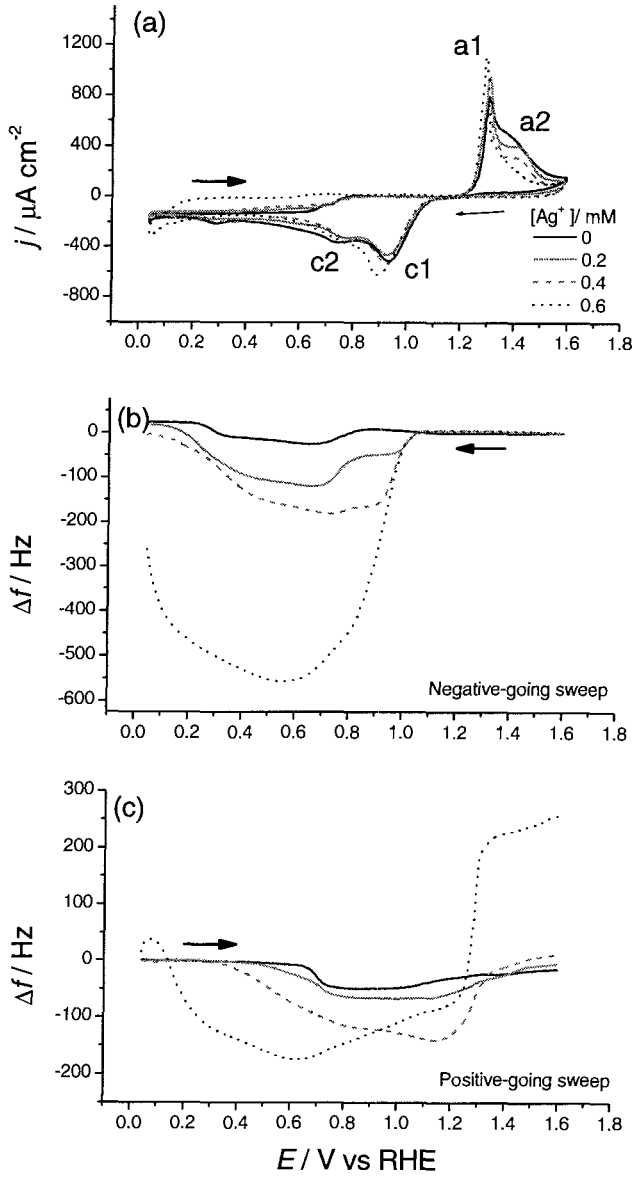

Figure 7.2: Pt EQCM response for iodate reduction with varying silver concentration. a) Cyclic voltammetry in a 1 mM IO_3^- solution with increasing Ag^+ concentration. Concentrations shown in legend correspond to $[Ag^+]$:$[IO_3^-]$ ratios of: 0:1, 1:5, 1:2.5 and 1:1.6 respectively. $\nu = 0.020$ V s^{-1}. b) Frequency response of the electrode during the negative-going sweep. c) Frequency response of the electrode during the positive-going sweep.

behaviour to the baseline case again with a slightly lower current observed from the sweep reversal until 0.7 V. A noticeable change occurs in the oxidation features with silver present. With increased silver concentration, the main oxidation peak (a1) becomes sharper and the tail of the peak (a2, very broad in the baseline case) becomes more defined while diminishing in magnitude. The CV for 1 mM IO_3^- and 0.6 mM Ag^+ shows the largest change. The peak position of the largest reduction peak (c1) shifts in the negative direction, increases in magnitude and becomes asymmetric. During the remainder of the sweep, the current magnitude is reduced except for the most negative potentials where the reduction current increases. The positive-going sweep shows minimal current in the 0.2 to 1.2 V region and the oxidation feature at 1.3 V (a1) is sharpest under these conditions.

Fig. 7.2b shows the frequency changes observed during the negative sweep. For concentrations of silver up to 0.4 mM, the general features of the frequency changes are similar to the baseline case but the magnitude is increased. A mass gain occurs at the electrode surface at 1.0 V. This is not observed in the baseline case and the mass would indicate that silver is deposited on the surface, likely the result of reaction 7.1. This is also demonstrated by the increase in frequency shift with increased Ag^+ concentration. The mass gain ceases at 0.7 V and during the remainder of the sweep the frequency increases, indicating a mass loss from the surface. This is similar to the baseline case and indicates that silver deposition is limited at these concentrations. This is interesting because silver deposition onto iodine-covered electrodes (from either KI solutions or using iodine vapour) is not hindered by the presence of the I layer and can result in frequency reductions far greater than those observed here. Note that even for diffusion-limited processes, the frequency drop would still be expected to increase, unlike the current response for such processes, which levels off. This finding could indicate that the film formed at features c1 and c2 is in fact AgI as a result of reaction 7.1. This film could act as a passivating layer as discussed shortly. At the highest silver concentration (0.6 mM) the frequency

shift at 1.0 V is much larger but ceases at 0.6 V and begins to show mass loss that continues through the remainder of the sweep.

The frequency shifts accompanying the positive-going sweeps are shown in Fig. 7.2c. Again the 0.2 and 0.4 mM traces show very similar behaviour to the baseline case; however, the magnitudes of the frequency shifts are larger. As well, mass gain occurs earlier in the sweep at higher silver concentrations. Mass is lost from the surface corresponding to the sharper oxidation feature (a1) observed with silver present. The 0.6 mM silver case demonstrates similar behaviour throughout the sweep although the changes are larger, much like the negative-going sweep. The mass loss continues right until the end of the sweep indicating a relatively slow process at work. This feature is observed in all cases involving silver with a similar shift in frequency over the same potential range. The fact that no mass is apparently lost at the characteristic stripping potential for silver ($\simeq$ 0.7 V), yet is lost near the reversible potential for reaction 7.2, provides further indication of an AgI film formed at the electrode. At higher concentrations of silver, precipitate formation was observed that was attributed to $AgIO_3$. The formation was barely visible at 0.4 and 0.6 mM, but was clearly evident at all higher concentrations.

Formation of silver iodate on the surface (shown in reaction 7.1) was ruled out due to the fact that no oxidation current was observed with the high mass to charge ratio (175 g mol^{-1}) that would accompany this reaction.

$$Ag(s) + IO_3^- \rightarrow AgIO_3(s) + e^- \tag{7.1}$$

In general, this system displays a relatively short deposition window (400 mV at the highest silver concentration). As well, the relatively high concentration of IO_3^- leads to significant solution-based charge transfer processes that complicate the analysis of the frequency shifts observed. It appears that films deposited in this system are limited in thickness at all concentrations of silver below the solubility limit.

Fig. 7.3a demonstrates the changes in the cyclic voltammetry when silver and iodate ions are present at equal or nearly equal concentrations. As might be expected, the system shows features evident in the two systems already discussed. Features such as the reduction peak (c1) beginning at 1.1 V and the c2 peak at 0.7 V, attributed to IO_3^- and Ag^+ (UPD) reduction respectively, both grow in as the concentrations are raised. However, there is only minimal evidence of a c3 peak resulting from bulk silver reduction observed at 0.6 V in Fig. 7.1a. This feature is best resolved at $[Ag^+] = 0.61$ mM, $[IO_3^-] = 0.40$ mM. Some of this difference can be attributed to the lower silver concentration compared with Fig. 7.1a. Negative of 0.6 V, increasing concentrations lead to higher current densities toward the end of the negative-going sweep. At the highest concentrations, an increase in current is observed below 0.1 V. The positive sweep shows a peak (a1) at 0.65 V. This peak is observed with only silver present but is suppressed initially when the iodate concentration is raised to 0.21 mM. As both concentrations are subsequently raised, the peak is again evident and grows with increasing Ag^+ concentration. This would again indicate that at certain concentrations, the formation of AgI via reaction 7.2 is favoured, and oxidation of the surface film is shifted significantly positive, reflecting the presences of AgI. With more silver present, the film formed is evidently composed of a greater amount of silver (reaction 7.5), which is stripped at the characteristic oxidation potential during the positive sweep. In all systems with IO_3^- present, a peak (a2) beginning near 1.2 V is observed and the magnitude of the peak is largely independent of the iodate concentration.

The negative-going sweeps for the different concentrations in the system (Fig. 7.3b) show that in all cases but for silver alone, the mass gain at the electrode commences at 1.15 V (driven by reactions 7.1– 7.3). However, likewise in all cases but the purely silver solution, deposition ceases during the course of the negative-going scan. The point at which the frequency begins to significantly increase (indicating mass loss) shifts from about 0.3 V with 0.21 mM IO_3^- present to 0.2 V at the highest

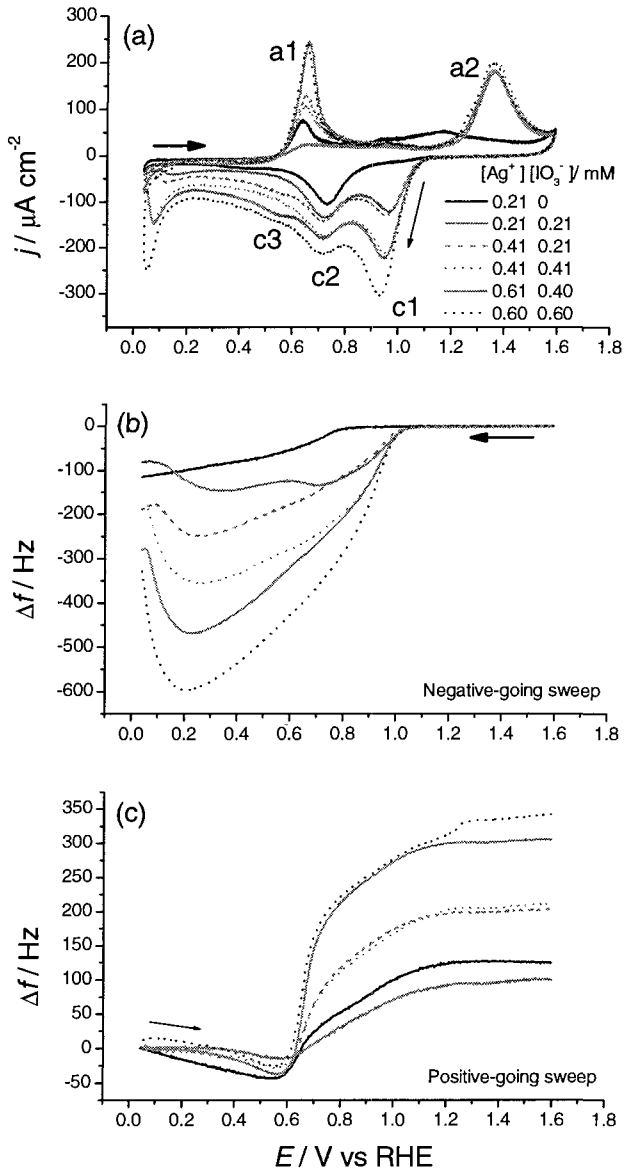

Figure 7.3: Pt EQCM response for iodate and silver codeposition at equal or nearly equal concentrations. a) Cyclic voltammetry. Concentrations shown in legend correspond to $[Ag^+]$:$[IO_3^-]$ ratios of: 1:0, 1:1, 1:0.5, 1:1, 1:0.7 and 1:1 respectively. $\nu = 0.020$ V s^{-1}. b) Frequency response of the electrode during the negative-going sweep. c) Frequency response of the electrode during the positive-going sweep.

concentration of both Ag^+ and IO_3^-. In the case where $[Ag^+] = [IO_3^-] = 0.21$ mM, it appears that the film production ceases early on in the scan (0.65 V) and ultimately when mass is lost near the end of the scan, the electrode is left with a lighter film than with silver present alone. The largest mass depletions observed at the higher concentrations correspond to the increase in reduction current in the solution.

The positive-going sweep (Fig. 7.3c) shows that when the scan is reversed, the electrode gains a small amount of mass in all cases. The removal of most of the deposited mass begins at 0.6 V and continues over a relatively large potential window of 0.60 V with significant frequency change ceasing by $\simeq$ 1.2 V. As with the cases shown in Figs. 7.1 and 7.2, the peak corresponding to oxidation of iodate (a2) has a minimal change of frequency associated with it, indicating a solution-based process.

Figs. 7.1, 7.2 and 7.3 indicate the most favourable conditions for further study. Very low concentrations of IO_3^- in the presence of 1 mM Ag^+ (Fig. 7.1) lead to thicker films and display increased mass compared with silver alone. The potential window for deposition is large (0.60 V to at least 0.040 V) and the relatively low concentration of IO_3^- should keep the solution-based processes involving this ion to a minimum. Conversely, Figs. 7.2 and 7.3 both indicate the formation of a film that reaches a maximum thickness and in most cases begins to lose mass at lower potentials. This could be indicative of the production of solution-species containing either Ag, I or both. This could also be an indication of loss of the film due to factors such as porosity. This is apparently coupled to a reduction reaction that is particularly evident when the constituents are at or near equal concentrations. The formation of these films that behave like passivating layers may yet indicate the production of AgI films. AgI is a semiconductor with a bandgap of 2.22 eV (sphalerite) or 2.63 eV (wurtzite) [147]. It is likely that a film formed of this material may inhibit further electrodeposition on the surface. With this in mind, it would follow that the films formed at low concentrations of IO_3^- have the form AgI_x with $x < 1$. The following sections explore these types of films and their applicability to single-solution layered

Feature	Predominant Reaction(s)	Remarks
c1	7.3 (followed by 7.1)	Along with PtO reduction
c2	7.3 (followed by 7.1)	Minimal AgI formation
c3	7.5	
a1	-7.5	Along with some loss of I
a2	-7.4	

Table 7.2: Predominant reactions taking place in 1 mM Ag^+ solutions with very low iodate concentration. See Fig. 7.1 and discussion. Negative signs indicate oxidation reactions.

materials.

7.3 Sweep-hold and RRDE experiments with very low ($\leq$ 0.12 mM) IO_3^- concentration

The CVs shown in Fig. 7.1a display three peaks during the negative-going sweep. The predominant reactions responsible for the features shown in the CV are given in Table 7.2. The corresponding frequency change indicates that at all potentials negative of 1.1 V, the electrode is gaining mass, indicating the formation of a film. Fig. 7.4 shows the relation between the accumulated charge density and the frequency shift at four potentials during the negative-going sweep in 1 mM Ag^+ solution with two concentrations of iodate present (0.06 and 0.12 mM). For each of these potentials during the negative-going scan, the sweep was halted for 60 s and 700 data points were collected. In Fig. 7.4, the data were collected by stopping at each potential indicated during the course of one negative-going sweep. Previous results presented in Chapter 5 showed changes in the slope of the frequency vs. charge density curves when analysing chronoamperometry data for a single process. These changes in slope were attributed to changes in the surface roughness brought about by film development. As the film develops in the early stages, the surface of the unpolished electrode becomes smoother and effectively decreases the mass loading on the electrode due

to interactions with the surrounding solution [59, 60]. Chapter 5 showed that, for silver films, holding the potential and analysing the latter portions of the frequency vs. charge density trace minimises the slope change due to surface smoothing because the roughness factor approaches a constant value over time. The data presented in Fig. 7.4 show this type of behaviour. The beginning portion of each trace corresponding to a specific potential shows a shallower slope than the latter portions of the trace (this effect is minimised at more negative potentials, where the film is thicker). For this reason, the last 300 points collected (26 s) have been analysed in all cases to formulate values of the mass/charge ratio at each potential (analysed sections are emphasised).

The mass/charge ratios (or 'masses') for the reactions considered in this system are shown in Table 7.1. Note that for all of the reactions except reactions 7.2 and 7.3, the expected mass gain or loss corresponds to the molar mass of Ag or I alone (108 and 127 g mol^{-1} respectively). The mass changes corresponding to reactions 7.2 and 7.3 are significantly lower (39 and 25 g mol^{-1} respectively) due to the higher number of electrons involved in these processes. The potentials selected in Fig. 7.4 correspond to potentials early on in each of the three reduction peaks observed in Fig. 7.1a and to the potential beyond the peaks where significant reduction current is observed and appears to be diffusion-limited. Most of the measured masses are well below those expected for Ag or I alone, but none are as low as those expected for reactions 7.2 or 7.3. These results coupled with the findings from the previous section indicate the production of AgI_x films where $x < 1$. A simple equation for x can be generated to reflect the contribution of reactions 7.3 (reduction of iodate) and 7.5 (reduction of silver) necessary to result in the observed mass for a specific process.

$$x = \frac{108 - (mass\ measured)}{5\,(mass\ measured) - 127} \tag{7.2}$$

This equation holds true for any combination of these reactions.

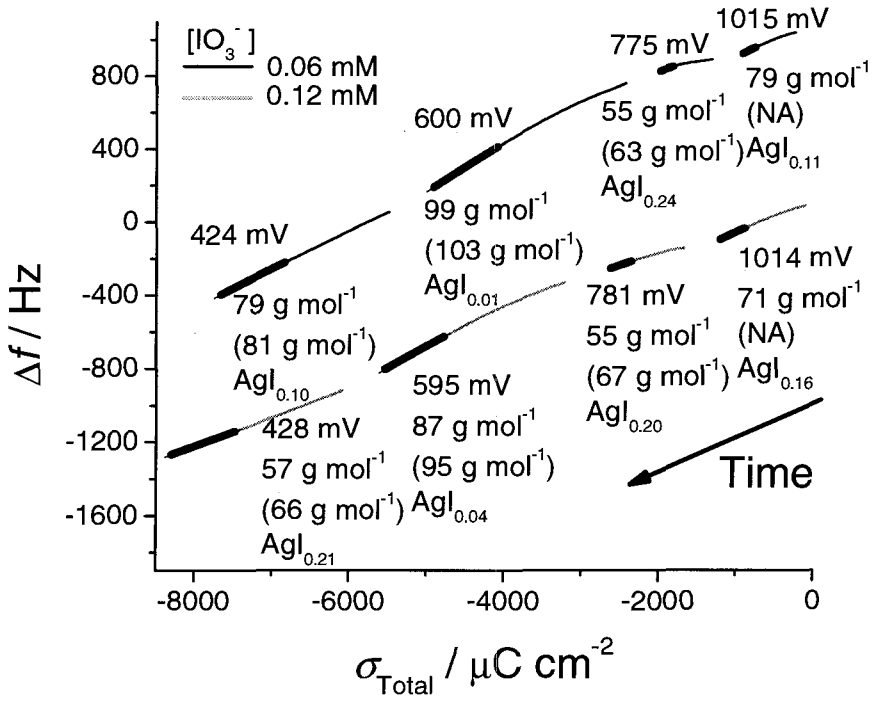

Figure 7.4: Results from sweep-hold experiments in 1 mM Ag^+ solutions with very low concentrations of IO_3^-. The data were obtained in the course of 1 sweep (ν = 0.020 V s^{-1}). The hold potentials correspond approximately to features in Fig. 7.1. Fitted data are emphasised (see text). Masses in brackets correspond to corrected charge densities. Ag/I ratios determined using equation 7.2.

	$[IO_3^-] = 0.06$ mM		$[IO_3^-] = 0.12$ mM	
Neg. Limit (V)	Charge imbal.(μC cm^{-2})	%	Charge imbal.(μC cm^{-2})	%
0.78	-49	12	-78	18
0.60	-53	4	-113	8
0.42	-108	3	-231	6
0.04	-150 $\pm$ 106	3	-719 $\pm$ 93	13
Max. at 0.04	-244	4	-809	14

Table 7.3: Charge imbalances for cycles of a Pt electrode to various negative potential limits. Values are shown for low concentrations of iodate (and 1 mM Ag^+) and are also expressed as percentages of the total anodic charge of the scan. Cycles to 0.04 V represent full scale CVs and are shown with uncertainties and maximum imbalances noted.

The choice of reactions 7.3 and 7.5 favours a kinetic argument over a thermodynamic argument (represented by reaction 7.2). Equation 7.2 is simplistic in that it is based on the assumption that all of the observed current leads to film formation. With iodate present in solution, significant contributions to current from solution-based reactions have been observed that do not contribute to film formation (Chapter 6). This complicates analysis of the mass/charge ratio. To attempt to discern the contribution from these solution-based processes, the charge imbalances over electrode cycles to similar negative potential limits were measured. The percentage of charge lost to solution-based processes was determined by comparing the charge imbalance over the cycle with the total anodic charge measured during the positive-going sweep. Table 7.3 contains the results of these experiments.

The results in Table 7.3 indicate that the amount of charge lost to solution-based processes is relatively low under cycling conditions, especially in the 0.06 mM case. The percentages of solution-based charge were used to adjust the mass values in Fig. 7.4 (the adjusted numbers are shown in brackets). These mass values, to a better approximation, reflect the mass/charge ratio of the surface film being formed. Assumptions are still being made here. One is that the total anodic current stems entirely from film stripping processes when in actuality other solution-based oxidation reactions may be taking place. With the film already formed on the electrode, it is

likely that the contributions from these reactions during the positive sweep would be small in comparison. A second assumption is that the percentage of solution-based current is equal over the entire scan when it could in fact be associated with a specific potential range. For the EQCM technique, there is no obvious calibration reaction that could be used that would allow for a more accurate determination of surface vs. solution charge transfer processes to be made. Finally, the use of cyclic voltammetry does not mimic the sweep-hold process exactly, especially over time. With these considerations in mind, this series of experiments shows a reasonable trend. The percentage of solution-based charge is largest at potentials more positive of those corresponding to UPD or bulk silver deposition. As the iodate concentration is raised, the amount of solution-based current increases, as would be expected based on studies of IO_3^- alone.

The (adjusted) masses in Fig. 7.4 can be used to determine the value of x in equation 7.2. Note that for the most positive potential ($\simeq$ 1.01 V), the ratio has been calculated based on the raw, uncorrected mass. The reduction of the surface oxide near this potential made determination of the correction factor problematic. Note that even well positive of the expected onset of UPD silver, there is apparently silver deposition/AgI formation. This is likely driven by the favourable $\Delta_r G^\circ$ of reaction 1 once iodate is reduced to I(ads) on the electrode surface. The mass corresponding to iodate reduction alone is only 25 g mol^{-1}. The effect of reduction of the platinum surface oxide has also not been included in the calculation. This process accounts for a mass loss of 8 g mol^{-1}. In the 0.06 mM case, films formed during the negative-going sweep showed predicted empirical formulae of $AgI_{0.11}$, $AgI_{0.24}$, $AgI_{0.01}$, and $AgI_{0.10}$ according to equation 7.2. This indicates that iodide incorporation in the silver film is highest before the onset of bulk silver deposition. During bulk deposition, the film is predominantly silver and as this deposition reaches diffusion limitation, the relative amount of iodine increases. This can be viewed as a relative increase in contribution from reaction 3. Similar behaviour is observed when the

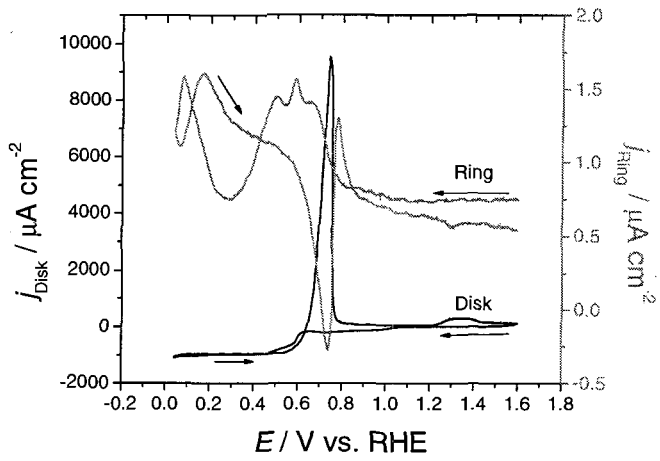

Figure 7.5: Disk and ring current responses of a Pt/Pt RRDE in 1mm Ag^+, 0.06 mM IO_3^-, $\nu_{Disk} = 0.020$ V s^{-1}, ring potential: 1.20 V, $f_{RRDE} = 1000$ RPM. The black trace corresponds to the disk current (left axis) and the grey trace corresponds to the ring current (right axis).

iodate concentration is doubled (Fig. 7.4, lower traces). Here the mass responses indicate films with $AgI_{0.16}$, $AgI_{0.20}$, $AgI_{0.04}$ and $AgI_{0.21}$ formulae and generally reflect a higher level of iodide incorporation in the films. With both species (Ag^+ and IO_3^-) under diffusion-limited conditions, the ratio of their respective concentrations might indicate an estimate for the expected ratio of Ag to I in the films. Under this assumption the expected values would be $AgI_{0.06}$ and $AgI_{0.13}$ for the 0.06 and 0.12 mM cases respectively, comparable to those observed.

To confirm the proposition that the solution-based currents are minimal at low IO_3^- concentration, a rotating ring-disk experiment was carried out under 0.06 mM IO_3^- and 1 mM Ag^+ solution conditions. The results for one cycle are shown in Fig. 7.5. The current response of the disk electrode appears somewhat different than that observed in Fig. 7.1a. The bulk deposition currents were much larger in the RRDE experiment; however, the surface features attributed to AgI deposition at potentials more positive than 0.6 V are evident under magnification. The ring potential (E_r)

was set to 1.20 V to oxidise I^- (created via solution-based charge transfer at the disk) back to IO_3^- (reverse of reaction 7.4). .Note that the ring current magnitude is very low for the entirety of the cycle. The ring current increases when the disk is at 0.8 V corresponding to the formation of the first layers of AgI (and a small amount of solution-based species) prior to more rapid silver deposition. Some reproducible fluctuations in the ring current occur concomitant with the onset of the higher disk currents. As the potential becomes more negative the ring current decreases indicating a drop in solution-based species being produced. This corresponds well with the values of I incorporation determined above. Nearing the end of the negative sweep there is an increase in ring current that again agrees well with the findings indicating increased rate of iodate solution reactions at this potential extreme. During the positive-going sweep, the ring current remains relatively stable until it dips significantly just prior to anodic stripping of the film formed on the disk electrode. The ring current response increases sharply as the bulk of the film is stripped, pointing to release of iodine species with film dissolution. The nominal collection efficiency of the RRDE (22.0%) was used to separate the solution-based current from the deposition current at the disk. On the scale shown in the figure, the current from solution-based processes was imperceptible compared to the deposition current. These data confirm that the increased currents observed with increasing iodate concentration during the early stages of AgI film formation (1.0 V $\rightarrow$ 0.6 V, Fig. 7.1a) are due predominantly to the increased surface charge transfer associated with film formation and not excess solution-based reaction.

A similar set of sweep-hold experiments was conducted in which the potential holds were not applied subsequently during the same sweep. That is, between potential holds at one value, the electrode potential was cycled over the full potential scale until the steady-state voltammogram was observed. This experiment was performed in an effort to discern what effect (if any) the thickness and structure of the underlying film has on subsequent deposition. The results from these experiments are shown in

Fig. 7.6.

A comparison of Figs. 7.6a and b with their counterpart potentials and iodate concentrations in Fig. 7.4 reveals that at the more positive potentials (1.01 and 0.78 V), there is little difference in the calculated x values. This indicates that early stages of film development at the surface do not appear to be greatly affected by the iodate concentration nor to the prior conditioning of the electrode. At the more negative potentials greater differences are observed. Under 'steady state' conditions prior to the potential hold (Fig. 7.6a) the predicted formulae in 0.06 mM IO_3^- at 0.60 and 0.42 V were $AgI_{0.06}$ and $AgI_{0.45}$ respectively. Compared with the results from Fig. 7.4 ($AgI_{0.01}$ and $AgI_{0.10}$ at similar potentials) this shows that the iodide incorporation appears to be much higher when the pre-existing film on the electrode is thinner. This behaviour is also observed in the 0.12 mM case. At the lowest potentials the results show films of $AgI_{0.08}$ and $AgI_{1.72}$ compared with $AgI_{0.04}$ and $AgI_{0.21}$ when the holds were applied in the same sweep.

7.4 Anodic stripping of thicker films

To further examine the role of solution-based charge transfer reactions over longer periods and the role of film thickness on the deposition of AgI_x, films were deposited at 0.40 V for different amounts of time and were then stripped from the surface by applying a positive potential sweep. To amplify the effect of the iodate, the solution contained 1 mM Ag^+ and 0.18 mM IO_3^-. The results of these experiments are shown in Fig. 7.7.

The figure shows the anodic stripping electrochemical data (a) and the corresponding frequency vs. charge density traces (b). The films were formed over 120, 300 and 540 s. The positive sweep began from 0.40 V (the deposition potential). Anodic current began just before 0.60 V in all three cases. The magnitude of the peaks follows the expected trend of thicker films for longer deposition time; however

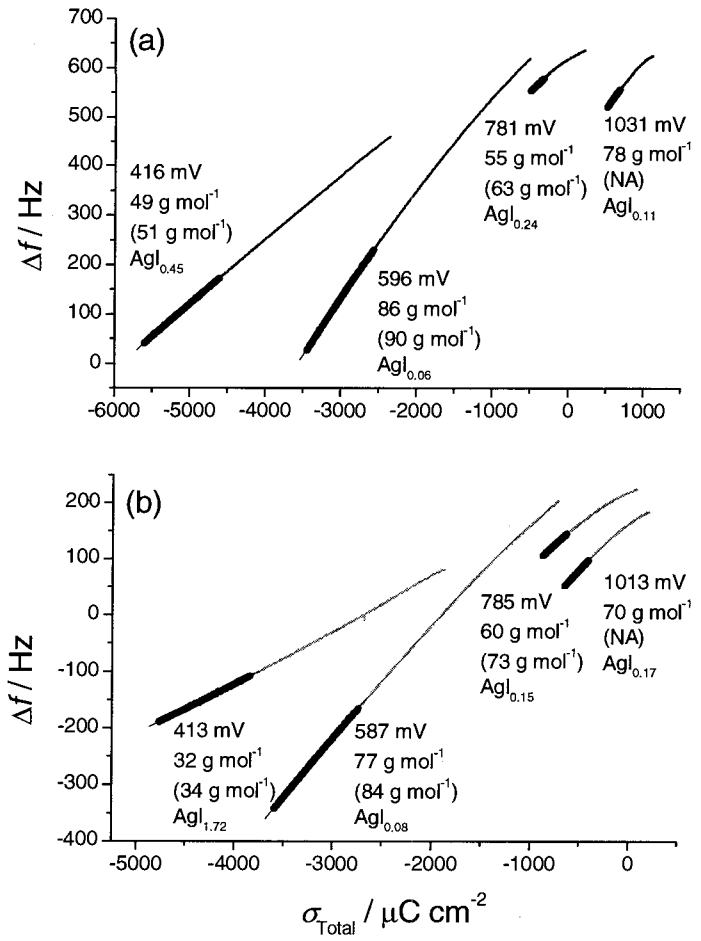

Figure 7.6: Results from sweep-hold experiments (ν = 0.020 V s^{-1}) in 1 mM Ag^+ solutions with very low concentrations of IO_3^-. The concentration of IO3- in (a) is 0.06 mM, and in (b) is 0.12 mM. The data were obtained in separate sweeps. The hold potentials correspond approximately to values of features in Fig. 7.1. Fitted data are emphasised (see text). Masses in brackets correspond to corrected charge densities. Ag/I ratios were determined using equation 7.2. Individual traces have been shifted for clarity to avoid overlap (markers on the x-axis shown for magnitude only).

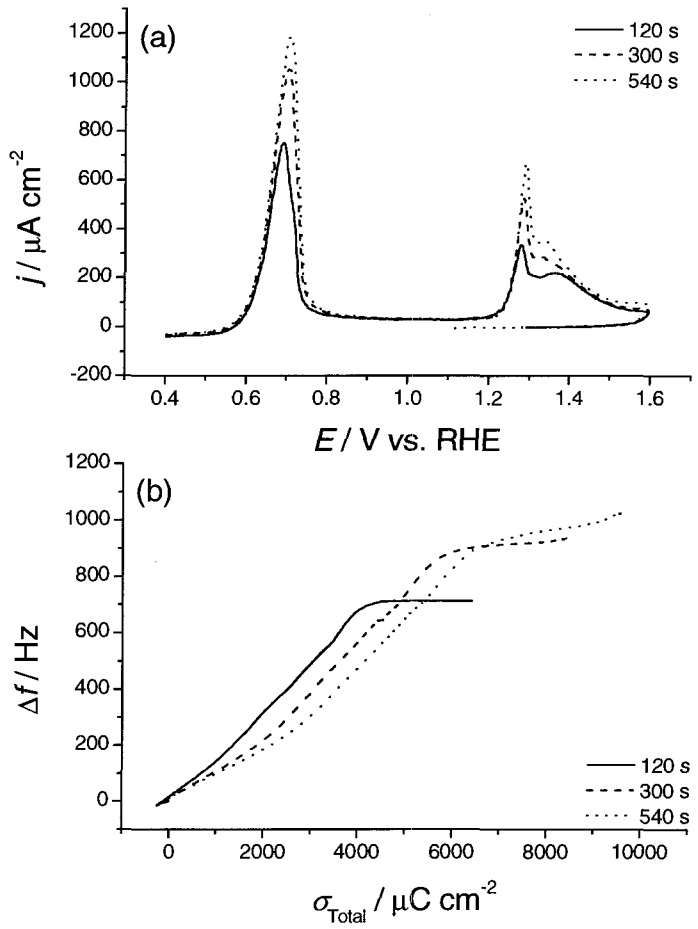

Figure 7.7: Current density and frequency response during stripping of AgI_x films. Concentration of Ag^+ = 1 mM, concentration of IO_3^- = 0.18 mM. $\nu = 0.020$ V s^{-1}. a) Voltammetry for the positive sweep to strip films of AgI_x from the Pt surface. b) Frequency vs. charge density response during film removal.

Dep. time (s)	Dep. Mass ($g\ mol^{-1}$) First 20 s	Last 20 s	Strip. Mass ($g\ mol^{-1}$) Change over peak
120	19	15	58 → 78
300	22	11	45 → 81
540	22	8	40 → 74

Table 7.4: Masses observed during the deposition (at 0.40 V) and stripping of 120 s, 300 s and 540 s films in 1 mM Ag^+ and 0.18 mM IO_3^-.

it is clear that the anodic charge is not linearly related to the deposition time. A similar trend is observed concerning the absolute mass changes of both the deposition and stripping processes. The current drops sharply by 0.8 V and is minimal until the potential reaches 1.2 V. A sharp feature that becomes accentuated for the thicker films is observed at 1.28 V and this is followed by a broader feature that tails off by the end of the scan. This feature is very similar to the oxidative features observed in Fig. 7.2. The frequency vs. charge density responses for the three films (Fig. 7.7b) all show a change in slope at potentials corresponding to the peak potential near 0.7 V. This effect is more pronounced for the thicker films. The masses observed during the deposition of these films also changed over time although not as markedly as during the stripping. A comparison of the masses observed during the deposition with those observed during dissolution of the film provides some insight into the charge lost to solution-based processes. The data are summarised in Table 7.4.

During deposition, the mass observed in all three cases is very similar during the first 20 s of film development. As the deposition proceeds for longer durations, the apparent mass of the film is reduced by 50% and is quite low. During stripping of these films, the initial mass is lower for thicker films but shifts to a relatively constant higher value as the stripping proceeds. These results clearly indicate some key characteristics of the films. The very low mass suggested during deposition indicates in general that there is a significant amount of charge transfer due to solution-based reactions that significantly decreases the apparent masses of the films. This fact is corroborated by the higher masses observed during stripping that are likely less

susceptible to this effect. The heightened solution-based charge transfer reflects the higher concentration of iodate used in these trials. The apparent reduction in observed mass over longer deposition periods suggests that either the iodide incorporation increases or that the solution-based charge transfer processes play a larger role after prolonged deposition. The stripping data indicate that both of these processes play a role. The shift from lower to higher apparent masses for the stripping process for all three films suggests a change in structure as more of the film is stripped away. For longer durations of deposition, the film exposed to solution appears higher in iodine concentration (reactions 7.2 and 7.3, Table 7.1); however, as noted, the charge observed during stripping does not increase linearly with deposition time. This may indicate that migration of iodine into the film occurs with prolonged deposition time. This is also indicated by the fact that in all cases, the stripping process eventually reveals a similar mass stripped from the surface, suggesting similarly structured films closest to the electrode.

The total frequency shift observed over the course of the main stripping peak can be utilised to attempt to approximate the thickness of each film since the majority of the total shift occurs over this feature. Combining the sensitivity of the electrode (0.188 Hz ng^{-1} cm^{-2}) with the area of the electrode and the frequency shift results in a mass change in nanograms stripped. The thickness determination depends on the structure of the film, which is discussed in more detail shortly. To provide the most likely limits to the film thickness, the calculation was performed using the density of pure silver (10490 kg m^{-3}) and pure silver iodide (5683 kg m^{-3}) [112]. The results are summarised in Table 7.5.

The masses for the features observed positive of 1.2 V indicate that a predominantly silver film is stripped corresponding to the sharp feature (masses of 95, 97 and 91 g mol^{-1} for 120s, 300 s and 540 s films respectively). This oxidation potential corresponds well with the reversal of reaction 7.2; however, it is very interesting that the mass signal is much higher than what would be expected for this process (39 g

Dep. time (s)	Thickness 'Ag' (nm)	Thickness 'AgI' (nm)
120	4	7
300	5	9
540	6	10

Table 7.5: Thickness limits based on anodic stripping of films deposited at 0.40 V for 120 s, 300 s and 540 s in 1 mM Ag^+ and 0.18 mM IO_3^-. Calculations based on pure Ag and AgI densities.

mol^{-1}). It appears that a small amount of iodine present in the film may significantly shift the oxidation potential to a value closer to AgI oxidation. This sharp feature is overlaid onto a broad peak that reflects predominantly solution-based processes (masses of 2, 7 and 13 g mol^{-1} for the films respectively, with the higher masses for the thicker films likely an artifact of the greater overlap with the previous feature).

7.5 Layered materials: AgI_x/AgI_y (x, $y < 1$)

The changes in reaction rate and apparent mass deposited at the electrode have been probed as the foundation for producing layered materials in a single solution. By applying a pulsed potential sequence in a solution containing an excess of silver ions and a minimal concentration of iodate ions it appears possible, (based on the results presented in the previous sections), that a layered material of the form AgI_x/AgI_y can be created. Ideally, a structure in which $x \simeq 0$ and $y \neq 0$ can be created, which is essentially a metal/compound superlattice material. However, complete exclusion of the iodide is likely difficult. With this in mind, optimising the contrast between x and y is a more achievable goal. Fig. 7.8 outlines the process of applying a diagnostic pulse sequence to the electrode under various solution conditions (Figs. 7.8b-d correspond to the solution conditions outlined in Figs. 7.1-7.3 respectively).

Fig. 7.8a outlines the potential sequence applied in all cases for the traces shown in Figs. 7.8b-d. The sequence begins at 0.400 V for 10 s and switches to 0.375

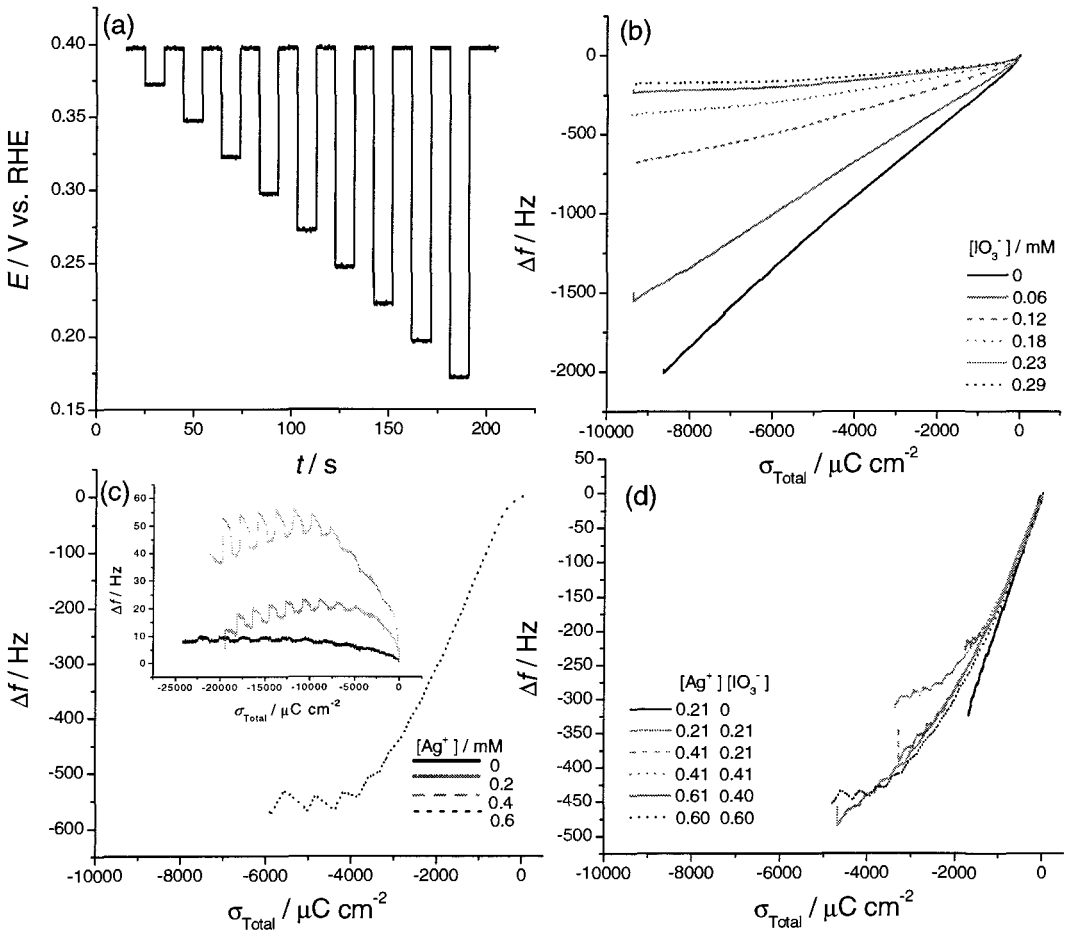

Figure 7.8: Diagnostic pulse sequences to probe production of layered materials. a) Potential sequence applied throughout b-d. Frequency vs. charge density response under b) 1 mM Ag^+, very low (< 0.3 mM) IO_3^- conditions, c) 1 mM IO_3^-, low (≤ 0.6 mM) Ag^+ conditions and d) equal or nearly equal concentrations (≤ 0.6 mM) of Ag^+ and IO_3^-.

V for 10 s before returning to 0.40 V. The next pulse applied was 0.350 V and this sequence was continued, a decrease of 0.025 V and a return to 0.400 V, until the potential range from 0.400 V to 0.175 V was covered. Fig. 7.8b shows the frequency vs. charge density traces for the solution containing 1 mM Ag^+ and very low concentrations ($0 \rightarrow 0.29$ mM) of iodate. As the pulse sequence was applied the frequency steadily decreased while significant reduction charge was passed at the electrode, indicating the formation of a film. As the amount of iodate in the solution was increased, the magnitude of the frequency change decreased (producing a thinner film) while the accumulated charge remained relatively constant. This is due to the increased charge transfer from solution-based processes. Changes in the slope of the transient indicate a change in the surface process taking place. Changes in the slopes in Fig. 7.8b are subtle but become more pronounced as the potential interval of the applied pulses is widened. These changes are explored in the remainder of the chapter. For comparative purposes, Figs. 7.8c and d show the effect of the pulse sequence when IO_3^- is dominant in solution and when Ag^+ and IO_3^- are present in equal concentrations. In both cases the conditions are less than optimal. With iodate present in abundance (Fig. 7.8c) no film is formed until the concentration of silver reaches 0.6 mM. At this point, significant changes in the slope are evident; however, the excursions to lower potentials quickly indicate film loss. As well, the effect of charge transfer due to solution-based processes makes accurate determination of the structure most difficult in this solution. Fig. 7.8d shows similar behaviour to Fig. 7.8c with some apparent mass loss occurring at the most negative potentials. In both of these latter cases also note that the amount of reduction charge accumulated during the pulse sequence (when films are formed) is significantly reduced compared with the solution conditions used in Fig. 7.8b.

The results from Fig. 7.8b appear favourable provided that the change in slope (frequency vs. charge density) with a change in potential is significant. Fig. 7.9 shows the results of the apparent masses for the pulse sequence outlined in Fig. 7.8b

with $[Ag^+] = 1$ mM and $[IO_3^-] = 0.06$ mM. The figure shows a clear change in the mass of each layer as the potential gap of the applied pulses is increased. Ideally, the structure of a superlattice of this nature (each superlattice layer contains two layers of differing structure, AgI_x/AgI_y) would show significant differences in iodide incorporation between the layers. To a large extent, this should be reflected by the calculated molar mass for each individual layer. Note that the term 'superlattice' is used loosely here, as the properties of the subsequent layers change over time.

Each of the molar masses in Fig. 7.9 was determined by fitting the final 100 points in each 10 s pulse. This was done to minimise the contribution from double layer charging that occurs as the potential is changed between pulses (see Fig. 7.10 for an example). Removing the contribution from double layer charging only required the removal of 11 points from the 111 point data set for each pulse. Note that particularly for the larger differences in applied potentials between layers, the change in the frequency vs. charge density slope appears very distinct. This points to an abrupt interface between the layers of differing structure. The largest difference between layer molar masses occurred for the pulse interval of 0.400 to 0.200 V. The molar masses of these adjacent layers were determined to be 82 g mol^{-1} during the 10 s 0.400 V pulse and 46 g mol^{-1} during the 0.200 V pulse. This equates to layers with a $AgI_{0.09}/AgI_{0.60}$ structure if all of the charge passed is treated as contributing to forming the film. This assumption is likely not completely accurate; however, as has been shown, the charge attributed to solution-based processes is minimal for this low concentration of iodate. The masses determined for the 0.400 V pulses are relatively stable over the sequence, shifting higher by 12 g mol^{-1} as the pulses proceed. This indicates a greater contribution from Ag deposition in these layers. The data for the pulse sequence applied in the presence of 1 mM silver and 0.12 mM iodate was analysed as well. The sequence displayed the same general characteristics but demonstrated consistently lower measured masses at all potentials and showed a reduced contrast between the structure of adjacent layers.

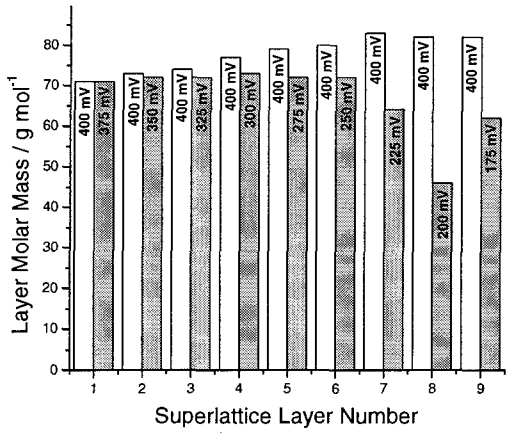

Figure 7.9: Measured molar masses corresponding to the analysis of the frequency vs. charge density transient shown in Fig. 7.8b with 0.06 mM IO_3^- present.

The continuous downward frequency shift during the entire pulse sequence (Fig. 7.8b) indicates that film production proceeds throughout. However, this also means that the structure recorded at pulse number 8 in Fig. 7.9 was deposited atop a film already apparently containing silver iodide layers produced in pulses 1 through 7. Experiments performed in which the potential interval of the pulses remained constant showed that the optimal pulse potentials for 1 mM Ag^+ and 0.06 mM IO_3^- was 0.500 $\rightarrow$ 0.150 V. The behaviour of a superlattice structure containing many layers (100) formed using this constant potential window is shown in Fig. 7.10.

Fig. 7.10a shows the frequency and current density response of the electrode during the formation of the first 10 superlattice layers. The frequency shows a steady downward shift and the current density clearly shows different magnitudes corresponding to the two applied potentials. The current density value is higher during the 0.150 V portion of the superlattice layer pulse as compared with the 0.500 V portion. Both of these current densities are significantly lower than those found in Fig. 7.1a and this is likely due to differences between steady-state and cycling behaviour. Over the course of the first 4-5 layers, the changes in the current density

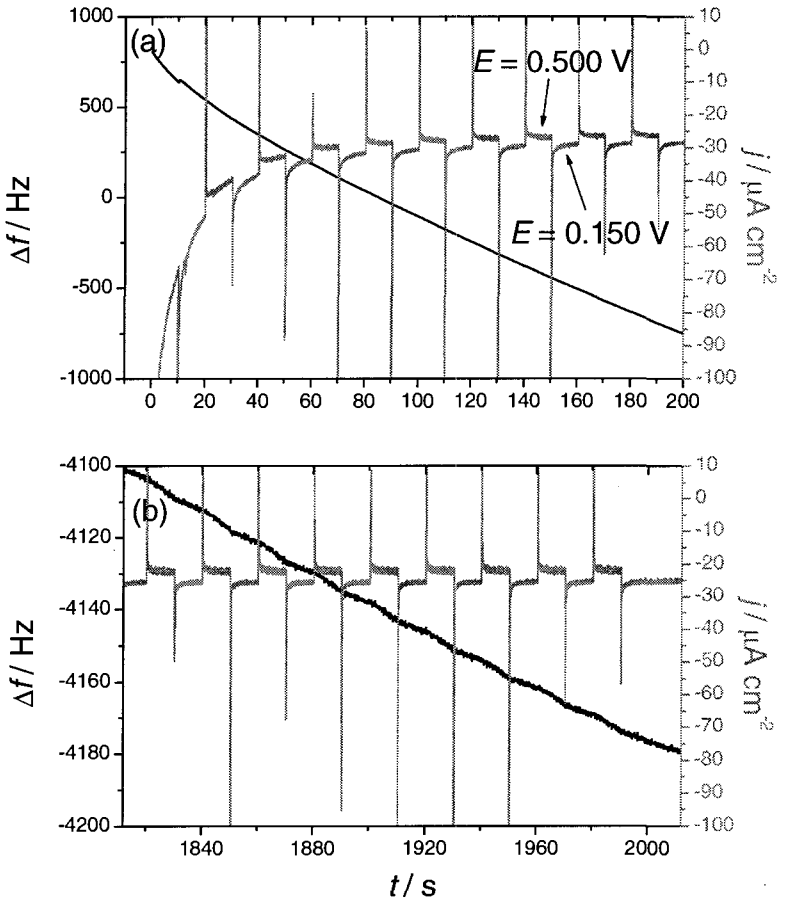

Figure 7.10: Frequency and current density response vs. time for a 100 superlattice layer film. (100 bilayers). The black trace corresponds to the left axis (frequency), the grey trace corresponds to the right axis (current density). Potentials applied = 0.500 and 0.150 V. a) First 10 layers. b) Last 10 layers. 1 mM Ag^+, 0.06 mM IO_3^-.

appear superimposed on a larger decaying function. This likely represents an overall decrease in electrode conductivity that arises due to the formation of the first few superlattice layers. This complicates the analysis to some degree and may indicate that the true masses of the individual layers are more accurately reflected over time (at 10 or 20 superlattice layers for example) Fig. 7.10b shows the frequency and current density response of the electrode for the last 10 superlattice layers. At this point, the frequency continues to decrease over time; however, the magnitude of the change between layers is significantly reduced compared to the first 10 layers. This allows for a clearer view of the distinct changes in frequency response between layers. The current density shows very similar behaviour to that shown in part a, with the magnitude of the signal continuing to change at each potential shift.

The data concerning the structure of the 100 superlattice layer film are summarised in Fig. 7.11. Fig. 7.11a shows the change in the observed layer molar mass with increasing superlattice layer number. The masses for the earlier layers show significant contribution from silver evidenced by higher molar masses than those observed in Fig. 7.9. However, there is a contrast between the layers of the superlattice that amounts to 15 - 20% or greater for all but the very first layer. These data represent a best case scenario and have not been corrected for any charge lost to solution-based processes. It is possible that the low masses measured after long periods could be more greatly affected by an increase in solution-based processes. The greatest contrasts between the layers formed at 0.500 and 0.150 V were found at lower layer numbers. At layer 3, the contrast is measured as $AgI_{0.04}/AgI_{0.10}$ while at the 30th superlattice layer the contrast has dropped to $AgI_{0.5}/AgI$.

Fig. 7.11b shows the increase in mass of the individual layers for the entire superlattice. This follows the same general trend over the course of the film formation as observed for the molar mass. The mass increase was used to determine an approximate thickness of each individual layer comprising a superlattice layer. The thicknesses were determined using the densities of Ag (pure) and AgI (pure). The

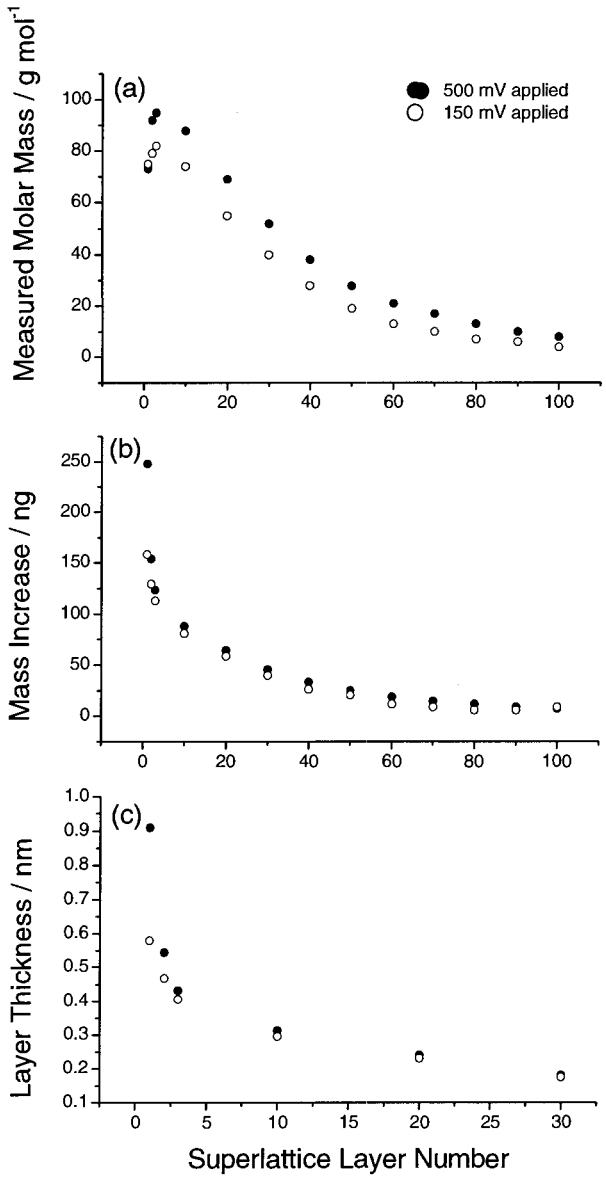

Figure 7.11: Structural analysis of the 100 superlattice layer film created in Fig. 7.10. a) Layer molar mass of each component of each superlattice layer. b) Mass increase per superlattice layer. c) Calculated thicknesses for the first 30 superlattice layers.

relative amounts of Ag in each layer (calculated using equation 7.2) were used as a means of weighting the average density (thickness) between Ag and AgI. These values are therefore only approximate. However, the results indicate that the individual layer thicknesses are very small and this thickness becomes smaller as the film grows. Very thin layers (below 10 nm) are desirable in nanolaminate materials in order to exploit effects that are not observed in bulk samples of the layering materials. Note that the data are only presented here out to the 30th superlattice layer given that the approximation of equation 7.2 becomes poor once the observed mass drops below 39 g mol^{-1}, which is likely a consequence of increased charge due to solution-based reactions or to an increase in the relative contribution of reaction 3 that may ultimately inhibit further film formation. Other researchers [130] have observed a decrease in layer thickness associated with a thickening film prepared using Electrochemical Atomic Layer Epitaxy (EC-ALE)

One concern regarding the structural determination of the multilayer film with the EQCM is that the apparent changes in layer structure actually simply reflect changes in the amount of solution-based charge transfer taking place. In an attempt to determine the relative contribution of solution-based processes during multilayer formation, the potential sequence was applied to a rotating ring-disk electrode under the same solution conditions. The results are shown in Fig. 7.12. The ring potential was set to detect the oxidation of I^- to IO_3^- (reverse of reaction 7.4). Fig. 7.12a shows the disk and ring current responses during multilayer formation. The response of the disk current is similar in structure to that observed in Fig. 7.10, although the convection present in the stirred solution results in much larger currents observed. The smaller changes here appear to be overlaid on a larger increasing reduction current. The film formed on the disk appeared to be nodular in nature and was likely affected by the different conditions set up by the electrode rotation. The overall reduction current is likely brought about by nucleation and growth associated with the more nodular film formation using this technique. The ring current observed

during multilayer formation is very low and fluctuates in general by less than 1 μA cm^{-2} during multilayer formation. It is evident that the ring current experiences a slight increase during the 0.150 V portion of each superlattice layer deposition. This agrees well with previous observations of increases in solution-based charge transfer at lower potentials. However, the data clearly indicate that solution-based charge transfer is minimal during the multilayer formation. Again, as with Fig. 7.5, the purely solution-based current was determined from the collection efficiency of the ring. On the scale of the disk current, the subtraction of the solution-based current was imperceptible. This provides good evidence that the structural changes related to iodine incorporation inferred from the EQCM data reflect real changes in the film structure. As further evidence of iodide incorporation into the multilayer film, the ring current was monitored during multilayer film dissolution. Fig. 7.12b shows that the ring current exhibits the characteristic dip in magnitude just before film stripping (see Fig. 7.5). However, here the ring current exhibits a very large relative increase (off instrument scale) during film stripping, indicating the release of a large (relative) amount of iodine species as the film dissolves.

7.6 Further discussion

The preceding structural analysis of the EQCM films is founded on the assumption that the electrodeposition forms a film that maintains a relatively constant roughness. The possibility exists that the deposition is uneven and may form a nodular or highly-defective film or may contain many grain boundaries that function as preferential nucleation sites for one species or another. It has been shown previously that the EQCM can be used as a sensitive tool in determining changes in the surface roughness of a deposit forming on the electrode surface (Chapter 5). The results from Figs. 7.4 and 7.6 indicate a similar behaviour to that observed when silver alone was deposited onto the electrode. The frequency vs. charge density traces for more

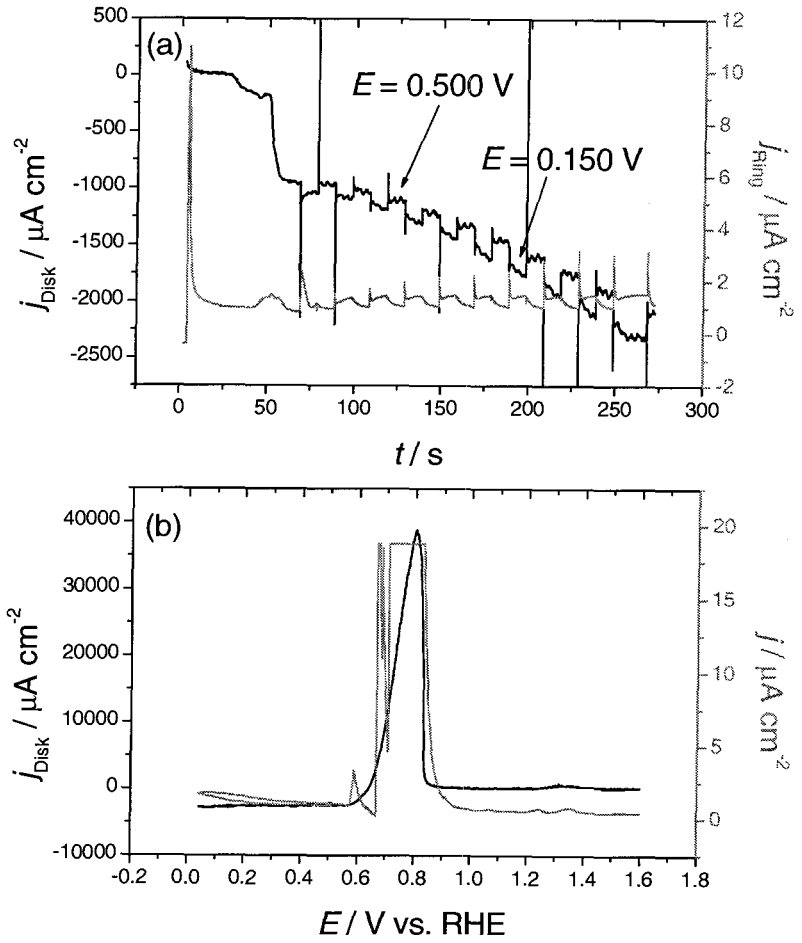

Figure 7.12: Ring-disk current response during multilayer film formation. The black trace corresponds to the left axis (frequency), the grey trace corresponds to the right axis (current density). a) Response during 10 superlattice layer (0.500 V $\rightarrow$ 0.150 V) formation. b) Response during film dissolution (ring current offscale). 1 mM Ag^+, 0.06 mM IO_3^-, E_r = 1.20 V, f_{RRDE} = 1000 RPM, ν_{Disk} = 0.020 V s^{-1}.

positive potentials (early film development) show slopes that become steeper over time. This indicates that the initial deposit begins to smooth the surface. However, this smoothing likely has a much greater effect on the surface micro or nanostructure as opposed to larger surface features/roughness. For this reason it is possible that the films formed consist of many different grains (on the scale of hundreds of nanometres) and may be more amorphous in nature. On the nanoscale, the features likely possess compositional modulation based on the findings presented here. It should be clarified, however, that the thicknesses calculated in the chapter are average values. In actuality, the films may be uneven due to nucleation and growth factors. Note that the films formed at more negative potentials (closer to those used in the superlattice pulse sequences) show minimal changes in slope over time. This suggests that at these potentials, films formed on the underlying deposit (created earlier in the sweep) do not exhibit significant changes in surface roughness (on any scale), suggesting that large changes in surface structure have ceased by this point.

In general, many trials involving superlattice deposition showed similar behaviour including reduction in observed mass per layer and thickness per layer with increasing superlattice layer number. One factor that was very sensitive was the initial value of the observed mass for earlier layers. In the case shown in Fig. 7.10, the masses of the first layers were relatively high. In other trials, under similar conditions, the same applied potential sequence produced lower masses in the initial layers. These fluctuations are likely the product of the underlying film present before the superlattice pulse sequence begins. As has been shown, the presence of films of silver and silver iodide effectively reduce the observed mass of subsequent layers. Small differences in the underlying film thickness, affected by cycling conditions or duration or overall electrode roughness, appear to play a significant role in this respect.

The pulse sequences applied during the formation of superlattice structures were very basic. Other researchers [144] have encountered reduction in film thickness with layer number and other dissimilarities between superlattice layers. A logical next

step to compensate for the uneven thicknesses of the layers would be to apply a more tailored pulsed potential sequence. Fig. 7.13 shows a comparison of layer thicknesses (first five layers) between the film formed in Fig. 7.10 and a film formed by lengthening the deposition time for each superlattice layer by 4 s compared with the previous layer. The results show that the estimated layer thickness can be substantially stabilised even through this minor adjustment. To probe the possibility of increasing the deposition rate per layer, another pulse sequence was applied in which the deposition potential of each superlattice layer was lowered by 0.050 V. This quickly led to destabilisation of the film and to the onset of significant hydrogen evolution current.

The use of iodate in the solutions resulted in the complicating factor of determining the role of solution-based charge transfer reactions. Several different systems have been studied to illustrate the magnitude of this factor as a function of iodate concentration. At low concentrations the effect is minimal so these conditions have been employed in attempts to form layered materials. Efforts have been made to be as quantitative as possible in assigning accurate structures to the deposited films. It would be desirable to apply these ideas and techniques in a system less susceptible to solution-based processes. Studies of codeposition of semiconductor materials CdTe [148] and CdSe [149] have been carried out with the EQCM and would be strong candidates for future studies in this area.

7.7 Conclusions

The electrochemical formation of silver iodide films has been explored using coreduction of silver and iodate ions onto Pt EQCM electrodes. The concentration of iodate appears crucial in determining the rate of film formation and in allowing continued electrodeposition. Higher concentrations show evidence of solution-based charge transfer reactions that complicate analysis of the film structure using the microbalance. At these higher concentrations, film thickness is limited and excursions

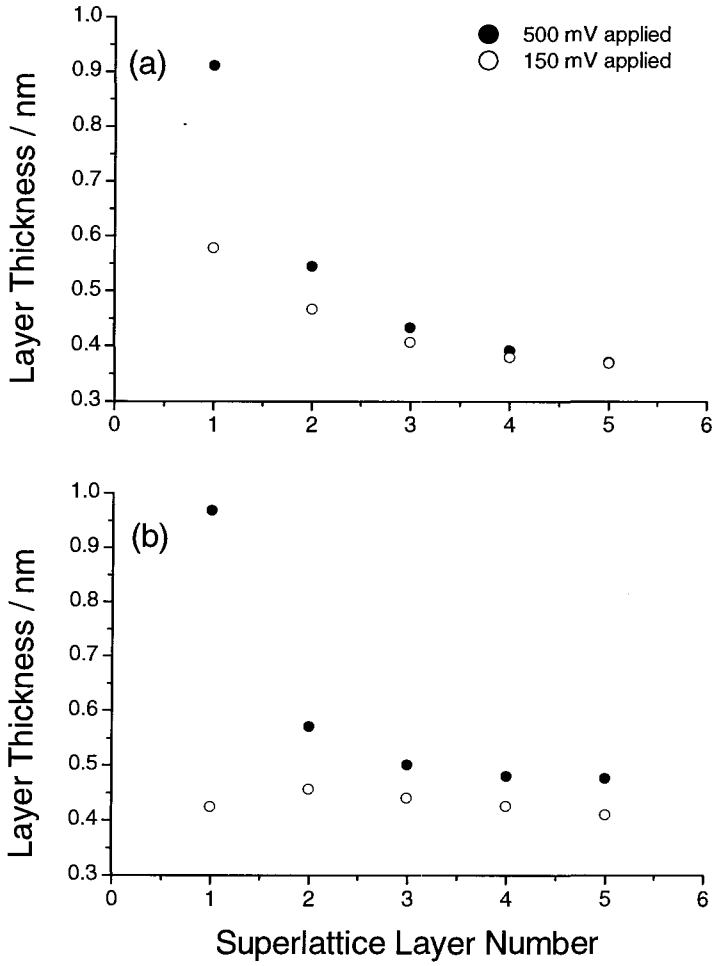

Figure 7.13: Comparison of estimated superlattice layer thicknesses for the first five layers of a film formed by a) equal (10 s) deposition times for all layers (Fig. 7.10), b) increasing each superlattice layer deposition time by 4 s compared with the previous layer.

to sufficiently negative potentials result in mass loss from the electrode. Sweep-hold experiments using very low relative concentrations of iodate show that deposition of thin films of silver and iodide at more positive potentials smooth the EQCM surface and allow for more uniform deposition at negative potentials. Films formed at these more negative potentials exhibit an AgI_x ($x < 1$) structure based on a simple model. The relative amount of solution-based charge transfer in solutions with low iodate concentration has been estimated and shown to be minimal. The effect of iodate incorporation in the growing films has been illustrated through analysis of thicker films in solutions of higher iodate concentration. A scheme has been developed and applied to utilise the differential incorporation of iodide at different applied potentials to create a layered material of the form AgI_x/AgI_y in a single solution. The results of the attempted formation of a 100 superlattice layer film show that structural contrast exists between layers; however, this contrast diminishes as the layer number increases. In general, uniformity between the layers is difficult to obtain using a basic pulse sequence but can be stabilised using increased deposition times for subsequent layers.

Chapter 8

Conclusions

8.1 Summary

This dissertation has presented work describing some general approaches to creating nanostructured and thin films using electrodeposition and several characterisation techniques including probe microscopy, X-ray characterisation, the electrochemical quartz-crystal microbalance and the rotating ring-disk electrode. The results range from fundamental details of film formation through to unique applications of film characteristics. From a practical point of view, the usefulness and application of the EQCM has been shown in analysing the details of film deposition and in the production of unique structures.

The deposition of Bi on Au(111) has been imaged with STM in both the UPD and OPD regions. Evidence has been provided suggesting that the reconstruction of Au(111) is lifted by the adsorbed bismuth, leading to the formation of gold islands on the surface only when the Bi UPD coverage is close to its maximum value. X-ray analysis of OPD Bi films has revealed the epitaxial growth of (012) surfaces of Bi atop the underlying structure of the Au(111) substrate. Pole figure analysis of the electrodeposited films has enabled modelling of the detailed atomic structure and epitaxy

of these films. Two unique epitaxial arrangements have been identified. The large coincidence lattices observed between the film and the substrate support previous findings of the predominance of the Bi(012) plane on a variety of substrates. The three-dimensional structure of the films has also been modelled and provides structural evidence for the anisotropic growth observed experimentally. The differences between the surface structures and the modelled structures have been explained in terms of enhanced surface corrugation and concomitant compression.

Electrodeposition of metal cations has been shown to be significantly affected by interactions between the surface and the solution brought about by changes in surface roughness accompanying the film deposition. This has been shown through a comparison of silver and copper deposition onto both bare and iodine-coated electrodes. For silver, the cyclic voltammogram of the coated electrode in supporting electrolyte is very simple, showing one deposition and one stripping process in the negative- and positive-going sweeps respectively. In addition, the mass change observed corresponds very well to the mass of silver in both cases. In contrast, in the absence of the iodine layer, four distinct features have been observed in both sweep directions. The mass changes observed for the bare electrode indicate significant smoothing of micro or nanostructural features during the negative-going sweep, giving way to a more uniform deposit (in terms of overall roughness) as the film grows. The presence of the iodine layer dramatically simplifies the interactions at the platinum surface, promoting layer-by-layer growth and maintaining a constant level of surface roughness. This system is therefore an excellent system for *in situ* calibration of the quartz-crystal microbalance. Comparison with the analogous copper system showed that the presence of the iodine layer mediates interactions between the analyte and the electrolyte to a lesser extent. Discrepancies are attributed to both the formation of copper islands on the surface and the interaction between the copper and the halogen film.

The behaviour of iodate ions in acidic solution has also been studied using the EQCM and a rotating ring-disk electrochemistry. Comparison of results using 0.2

and 1 mM solutions reveal significant contributions from solution-based reactions throughout the formation and dissolution of the iodine adlayer. Low mass/charge ratios under both conditions indicate formation of I^- and I_2(aq) products near the electrode surface with no evidence found for direct oxidative adsorption of the I^- ion. Suppressed mass/charge ratios observed in 1 mM solutions are attributed to the increased rate of solution reactions and the effect of these processes on the EQCM response has been presented. Formation of the iodine adlayer actually causes a net mass loss over the negative sweep. This is explained by a loss of adsorbed molecular iodine from the iodine adlayer and may also involve specifically adsorbed water and perchlorate ions. The latter are likely affected by a shift in the PZTC brought on by the formation of the iodine adlayer. RRDE findings corroborate the EQCM results.

The electrochemical formation of silver iodide films has been explored using coreduction of silver and iodate ions onto Pt EQCM electrodes. Iodate concentration plays a crucial role in determining the rate of film formation and in allowing continued electrodeposition. Higher concentrations show evidence of solution-based charge transfer reactions that complicate analysis of the film structure using the microbalance. Films formed at different potentials exhibit an AgI_x ($x < 1$) structure with varying values of x based on a simple model. The effect of iodate incorporation in the growing films has been illustrated through analysis of thicker films produced under higher iodate conditions. A scheme has been developed and applied to utilise the differential incorporation of iodide at different applied potentials to create a layered material of the form AgI_x/AgI_y in a single solution.

8.2 Future Work

There are several areas of the dissertation that point to interesting research opportunities. The ability to produce well-ordered Bi films is desirable because of the interesting properties of the material. These bismuth films can serve as a basis to

produce high quality Bi oxide thin films that have shown great promise for technological applications. Significant work has already been accomplished in this area that has not been reported in this dissertation and the results are very encouraging. It will be interesting and informative to measure the electrical properties of both the bismuth and bismuth oxide films. Work towards these goals is ongoing in the Morin laboratory at York University. The structure of films grown on Au(111) by slowly proceeding into the OPD potential region is inherently different than the films analysed as part of this work. The early stages of this 'slow' film growth show different and interesting morphology. Modeling of the growth characteristics of these films would be instructive in understanding other mechanisms by which Bi can be created.

The effects of surface roughness on thin film deposition has been well explored in the dissertation. It would be interesting to further examine the hypotheses presented by carrying out work exploring nucleation and growth behaviour and how this is related to the roughness argument. Developing systems to explore the interplay between roughness changes and ion desorption would also be quite interesting.

Many aspects of AgI_x project would be interesting to explore further. Microscopy (electron or scanning probe techniques) could be used to examine the surfaces at different stages of deposition to answer questions related to the uniformity of the deposits. Starting with a single crystal surface would likely promote more even deposits or more precise control over the reactions occurring at a given potential. Using these substrates, It might also be possible to utilise the microscopy techniques mentioned to examine the layered structure of the films. The composition of the films could be examined using techniques such as Energy Dispersive X-ray (EDX) analysis to compare with the values estimated from the EQCM response. This in general would be useful in determining the effectiveness of the EQCM as an *in situ* tool for advanced materials preparation. Finally, it would be interesting to explore the use of different chemistries using the approach outlined. Cadmium and

tellurium should behave similarly to silver and iodate but may be more susceptible to codeposition. CdTe is an interesting semiconducting material and the production of Cd/CdTe structures would be interesting to explore.

Appendix A

Analysis of X-ray Pole Figure Data

This section outlines the process of producing the atomic models of bismuth on gold presented in Chapter 4. In general terms this program demonstrates how to define two crystal geometries and use this information to generate two surfaces. With accompanying pole figure data, the program could be augmented to work out the epitaxial relationship in any system. Maple inputs appear in small font and are preceded by a '>'. Some basic Maple outputs (definitions) are not shown explicitly. Maple output is preceded by '**Output**' when it is required for clarity.

```
>restart;with(plots):with(plottools):with(linalg):
```

The first section sets up the coordinate systems that are required for all three structures of interest in this problem: rhombohedral (for Bi), hexagonal (for Au and a representation of Bi) and Cartesian (which is the underlying coordinate system for both - Maple transposes everything to this system). The coordinate systems here are all right-handed so that the vector math (cross-products in particular) is clear. This version of the program also uses the 'obverse' relationship between the hexagonal and rhombohedral coordinate systems.

Define the origin

```
>o:=[0,0,0];
```

Rhombohedral lattice parameters for Bismuth. Values from Wyckoff (25 degrees) [5], Angle between axes in degrees and radians

```
>alpha:=(57+14.2/60)*degrees;degrees:=Pi/180.:evalf(alpha);
```

Length of Bi unit cell in Angstroms

```
>a0Bi:=4.7459;
```

Radius of a Bi atom in Angstroms

```
>rBi:=1.55;
```

Bi atoms are at fractional coordinates (u,u,u) and (-u,-u,-u) [5]

```
>u := 0.237
```

Set up unit cell with body diagonal along the z axis (pointing up). Ends of the a, b and c axes end in an equilateral triangle normal to the z-axis and with the z axis passing through the centre. The edges of this triangle have the same length w as the edge of the hexagonal unit cell. w can be determined from the triangle cosine rule:

```
>w:=evalf(sqrt(a0Bi^2+a0Bi^2-2.*a0Bi*a0Bi*cos(alpha)));
```

The distance from the z axis (centre of the triangle) to one corner of the triangle is v=w/sqrt(3). By aligning this vector of length v with the x axis, the x and y coordinates of the three unit vectors are easily found. The height h of the triangle about the x-y plane may also be calculated. The long axis of the hexagonal unit cell is three times this.

```
>v:=w/sqrt(3.);h:=sqrt(a0Bi^2-v^2);`3h`:=3*h;
```

```
>a:=[v,0,h];b:=[-v/2,w/2,h];c:=[-v/2,-w/2,h];
```

Set up three basis vectors of the hexagonal unit cell using previously defined vectors.

```
>ahex:=[(3/2)*v,(-1/2)*w,0];bhex:=[0,w,0];chex:=[0,0,3*h];
```

Combine the three basis vectors

>hexaxs:=line(o,ahex,color=red),line(o,bhex,color=green),line(o,chex,color=black):

Complete the rest of the Bi hexagonal unit cell box

>hexbox1:=hexaxs,line(ahex,ahex+bhex),line(bhex,bhex+ahex),

line(ahex,ahex+chex),line(bhex,bhex+chex),line(ahex+bhex,ahex+bhex+chex),

line(chex,chex+ahex),line(chex,chex+bhex),line(chex+ahex,chex+ahex+bhex),

line(chex+bhex,chex+ahex+bhex):

The vectors 'a','b' and 'c' define three basis vectors on a rhombohedral Bi cell, the other lines on this cell are defined after these

>axs:=line(o,a,color=red),line(o,b,color=green),line(o,c,color=yellow):

edges:=line(a,a+b,color=blue),line(b,b+a,color=blue),line(c,c+a,color=blue),

line(c,c+b,color=blue),line(c+a,c+a+b,color=blue),

line(c+b,c+b+a,color=blue),line(a,a+c,color=blue),

line(b,b+c,color=blue),line(a+b,a+b+c,color=blue):

>rhombobox1:=(axs,edges):

The next plot is oriented to be looking down on the systems from above - and the orientation corresponds to that of the obverse relationship

>display(hexbox1,rhombobox1,orientation=[0,0]); (Shown in Fig. A.1).

This ends the section on the coordinate systems. The next section develops some basic data for the Au(111) surface so that a more extensive surface can be created with all of the appropriate rotations etc. applied to these first few elements (atoms and vectors). Vectors are developed first.

Development of the vectors for a cubic system is not too difficult. A combination of vectors such as $\mathbf{a}h + \mathbf{b}k + \mathbf{c}l$ ($|a| = |b| = |c|$) creates a vector normal to the (h,k,l) plane. From the pole figure data for gold, the vectors of interest are the normals to

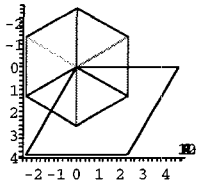

Figure A.1: Top view of the relationship between the rhombohedral and hexagonal Bi coordinate systems. Axes in Å.

the (111) surface, the (220) surface, the (022) surface and the (202) surface. First the coordinates of the cubic gold lattice are input.

```
>aAu:=[4.078,0,0]; bAu:=[0,4.078,0]; cAu:=[0,0,4.078];

>normvecAu111:=aAu+bAu+cAu;

>normvecAu220:=2*aAu+2*bAu+0*cAu;

>normvecAu022:=0*aAu+2*bAu+2*cAu;

>normvecAu202:=2*aAu+0*bAu+2*cAu;
```

For plotting, these vectors need to be turned into plot structures (making them into lines that can be shown on a plot). This is done for one of these vectors below (these are labelled 'normal' as opposed to 'norm*vec*'). The other vectors are changed in the same way.

```
>normalAu111:=line(o,convert(normvecAu111,list));
```

For plotting (and rotating) the entire set of 4 vectors of interest for the gold surface, they are grouped together.

```
>Aunormals:=display(normalAu111,normalAu220,normalAu202,normalAu022):
```

For plotting the Au(111) surface, a hexagonal gold coordinate system is created from the cubic coordinates

```
>ahexAu:=(1/2)*bAu-(1/2)*aAu; bhexAu:=-(1/2)*bAu+(1/2)*cAu;
```

The radius of Au atoms is defined

```
>rAu:=1.35;
```

Four Au atoms are defined below

```
>Auatom1:=sphere(o,rAu):Auatom2:=sphere(ahexAu,rAu):
 Auatom3:=sphere(bhexAu,rAu):Auatom4:=sphere(ahexAu+bhexAu,rAu):
```

Eventually it will be desirable to orient the Au(111) surface and the Bi(012) surfaces with both of their surface normals pointing along the Cartesian z axis. These commands calculate what the angle is for the Au(111) normal and about which axis this rotation must be applied. Finding the angle is not difficult. The rotation axis is determined by using the fact that the cross-product between the two vectors to be mapped onto each other (here the Au(111) normal and the Cartesian z-axis) generates a vector about which the rotation should be applied.

```
>Aurotateangle:=evalf(angle(normvecAu111,zaxis));
>Aurotateaxis:=crossprod(normvecAu111,zaxis);
```

The above information would allow for the Aunormals and the test Au surface atoms to be rotated so that the atoms lie in the xy plane and the normal points directly along the z Cartesian axis. Eventually however, another rotation will be required to rotate the gold surface with respect to the Bi surface so that the pole figure normals show the correct relation to each other. This can't be determined before the Bi normals are determined, so to avoid backtracking and in the interest of making this program as straightforward as possible, the normals for the Bi surface are worked out next.

As opposed to the cubic (Au) system, determining the surface normals to the planes for Bi in the hexagonal system is *not* trivial. It can either be worked out geometrically (by determining vectors that lie in the planes of interest and taking their cross-product) or it can be worked out in a more elegant manner by determining the 'reciprocal lattice vectors' for this lattice (see [150]). The number of commands below represents a very long-handed way of applying a simpler formula. As an additional note, the normals of interest for the Bi pole figure are 012 (the surface normal), and the normals to the planes (202) and ($\bar{2}22$), which are equivalent (but rotated by 180 degrees from each other) as determined in another Maple worksheet 'spacegp2.mws' written by Dr. D.A. Harrington

```
>ahexstarnum:=(crossprod(bhex,chex));

>ahexstardenom:=(dotprod(ahex,(crossprod(bhex,chex))));

>ahexstar:=scalarmul(ahexstarnum,(1/ahexstardenom));
```

Other reciprocal vectors are defined similarly. With these reciprocal lattice vectors determined, an analogous method can now be applied as in the cubic case, to find the normal to the plane of interest, the indices of the plane are multiplied by the reciprocal lattice vectors. The commands below do this and also multiply the result by a scalar simply to make the vectors longer for ease of display when plotting (they come out quite short using this method).

```
>normvecBi012:=scalarmul(evalm(scalarmul(bhexstar,1)+scalarmul(chexstar,2)),50);

>normvecBi202:=scalarmul(evalm(scalarmul(ahexstar,2)+scalarmul(chexstar,2)),20);

>normvecBi2bar22:=scalarmul(evalm(scalarmul(ahexstar,-2)+

 scalarmul(bhexstar,2)+scalarmul(chexstar,2)),20);
```

These vectors can be turned into lines for plotting as shown previously.

Since the underlying Au(111) surface has three-fold symmetry, the two vectors (202 and $\bar{2}22$) can each be rotated by 120 and 240 degrees to produce symmetrically

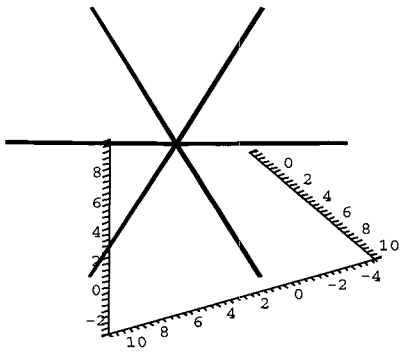

Figure A.2: Set of 7 normals corresponding to the Bi crystal. The Bi(012) surface normal points directly out of page, the Bi(202) and Bi($\bar{2}$22) normals are located 180° from each other. The other normals are their respective 120° and 240° rotations. Axes in Å.

equivalent orientations with respect to the gold surface, this turns the initial set of 2 vectors into a set of 6 vectors that are all separated from each other by 60 degrees

```
>set1Binormals:=display(normalBi012,normalBi202,normalBi2bar22,
rotate(normalBi202,2*Pi/3,[o,convert(normvecBi012,list)]),
rotate(normalBi202,4*Pi/3,[o,convert(normvecBi012,list)]),
rotate(normalBi2bar22,2*Pi/3,[o,convert(normvecBi012,list)]),
rotate(normalBi2bar22,4*Pi/3,[o,convert(normvecBi012,list)])):
>display(set1Binormals,orientation=[60,57]); (Shown in Fig. A.2).
```

This next section defines the Bi(012) plane to plot it with the hexagonal system and to show that the defined Bi(012) normal is normal to this plane (not shown explicitly here).

```
>hexplaneBi012:=polygon([bhex,ahex+bhex,ahex+((1/2)*chex),1/2*chex]):
```

The next step is to determine the angle and rotation axis necessary to map the

Bi(012) normal onto the z Cartesian axis (exactly as was done for the gold data)

```
>Birotateaxis:=crossprod(normvecBi012,zaxis);

>Birotateangle:=evalf(angle(normvecBi012,zaxis));
```

The Bi and Au normals can now be plotted, each rotated so that the 111 and 012 normals both point in the direction of the z axis. This will allow for the comparison of this theoretical plot with the pole figure results. This will determine how much the system of Au normals (and the entire Au surface) must be rotated with respect to the Bi normals to agree with the experimental results.

```
>rotatenormalsAu1:=

 display(rotate(Aunormals,Aurotateangle,[o,convert(Aurotateaxis,list)])):

>rotatenormalsBi:=

 display(rotate(allBinormals,Birotateangle,[o,convert(Birotateaxis,list)])):
```

For the purposes of plotting singular orientations of the normals later, this next command creates a plot structure with just the two normals associated with a single orientation (along with the 012 surface normal).

```
>onesetrotatenormalsBi:=

 display(rotate(normalBi012,Birotateangle,[o,convert(Birotateaxis,list)]),

  rotate(normalBi202,Birotateangle,[o,convert(Birotateaxis,list)]),

rotate(normalBi2bar22,Birotateangle,[o,convert(Birotateaxis,list)])):
```

To eventually determine the placement of the 'strong' signals in the pole figure with respect to the Au normals, define a rotated set of Bi normals that includes the basic Bi(202) and Bi($\bar{2}22$) normals

```
>rotatesetof6Binormals:=

 display(rotate(normalBi012,Birotateangle,[o,convert(Birotateaxis,list)]),
```

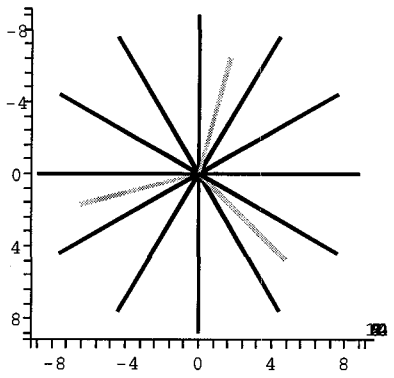

Figure A.3: Combined Bi (black) and Au normals (gray) for comparison with pole figure results. Axes in Å.

rotate(set1Binormals,Birotateangle,[o,convert(Birotateaxis,list)])):

>initialcombinednormals:=

display(rotatenormalsAu1,rotatenormalsBi,orientation=[0,0]):

> display(initialcombinednormals); (Shown in Fig. A.3).

To determine the rotation of one set of normals with respect to the other (to match with the pole figure results), one normal is selected from each group (Au and Bi) and the angle that each makes with a fixed axis (here the positive x axis, which in Fig. A.3 is pointing directly downward) is determined. The easiest way to do this is simply to look at the first two coordinates of the rotated normals (which give their projected coordinates in the xy plane). With these coordinates, the value of the angle with respect to the x axis can be determined by evaluating the arctangent.

>normalBi202;

Output: CURVES([[0., 0., 0.], [10.15944442, 0., 3.372134774]])

```
>rotatednormalBi202:=rotate(normalBi202,Birotateangle,[o,convert(Birotateaxis,list)]);
```

Output:

```
CURVES([[0., 0., 0.], [7.619583314, -4.399168479, 6.097119867]])
```

This produces the coordinates of the ends of one of the vectors in the rotated set of axes (above), the next step is to assign this as a vector to do vector math on it.

```
>rotatednormlistBi202:=[7.619583314, -4.399168479, 6.097119867];

>tanthetaBi202norm:=(4.399168479/7.619583314);
```

The numerator was made positive in the previous command so that the calculation would yield a real answer, the angle determined here is going clockwise from the positive x axis (axis pointing downward in Fig. A.3).

```
>thetaBi202norm2:=evalf(arctan(tanthetaBi202norm))*180/Pi;

>evalf(thetaBi202norm2);
```

Output: 30.0000000

This normal for the Bi(202) plane, when projected onto the xy plane, makes an angle of 30 c.w. degrees with the positive x axis. Next the same procedure is performed for one of the Au normals. (commands not shown here, next output is the angle for one of the gold normals).

```
>evalf(thetaAu220norm2);
```

Output: 44.99999998

This angle is taken to be 45 degrees c.c.w. from the positive x axis (in Fig. A.3 it's the one pointing diagonally downward to the right).

Now a comparison is made with the actual experimental pole figures to check the relations. On the pole figures, angular measurements were made from the positive x axis as well. For Bi the strong signal that's rotated c.c.w. from this axis by 17 degrees has been selected. For the gold, the signal corresponding to a 105 degree

c.c.w. rotation from the positive x axis has been selected. On the pole figure, the difference in angle between these two points is 105 - 17 = 88 degrees. In Maple it's been determined that the difference between these equivalent normals is 45 + 30 = 75. Therefore, to make the Maple data correspond to that observed in the pole figure, the Au vectors (and surfaces) need to be rotated by 75 - 88 = -13 degrees (c.w., to make the angle between them smaller as it is on the pole figure).

```
>planesrotate:=evalf(-13*(Pi/180));
```

This is the value in radians that the set of Au normals must be rotated by (and the rest of the Au structures will be rotated by) to make them agree with the pole figure results. The '0,0,planesrotate' part of the next command denotes to apply the rotation about the z axis.

```
>rotatenormalsAufinal:=display(rotate(rotatenormalsAu1,0,0,planesrotate)):
```

The next commands output the final correct orientation of the Au normals with respect to the Bi normals. This exactly mimics the orientation produced by the pole figures (see Figs. 4.3a and b. Fig. A.4 is a superposition of both experimental pole figure plots and has been oriented to correlate well with experimental pole figures as displayed).

```
>finalcombinednormals:=display(rotatenormalsAufinal,rotatenormalsBi,
 orientation=[-15,0]):
> display(finalcombinednormals);(shown in Fig. A.4)
```

With these rotations worked out, it is now possible to build the gold plane by performing the appropriate rotations on three of the gold atoms generated above (to put them in the right plane with the right rotation) and then determine the Cartesian lattice vectors between these rotated atoms to generate the rest of the surface. It is easiest to think of the atoms as points at the ends of vectors for now. These can then be rotated in this Maple package to generate the new coordinates. One atom (Auatom1) is set fixed at the origin.

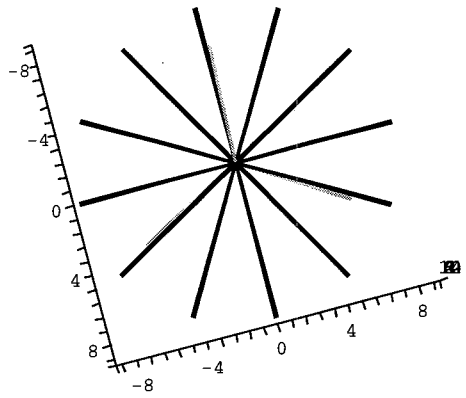

Figure A.4: Accurate orientation of the Au and Bi normals as determined through experimental pole figure results.

>Auatom2line:=line(o,ahexAu);

>Auatom3line:=line(o,bhexAu);

>firstrotateAuatom2line:=

rotate(Auatom2line,Aurotateangle,[o,convert(Aurotateaxis,list)]);

>firstrotateAuatom3line:=

rotate(Auatom3line,Aurotateangle,[o,convert(Aurotateaxis,list)]);

>secondrotateAuatom2line:=rotate(firstrotateAuatom2line,0,0,planesrotate);

Output:CURVES([[0., 0., 0.], [-2.445415763, 1.528065363, 0.]])

>secondrotateAuatom3line:=rotate(firstrotateAuatom3line,0,0,planesrotate);

Output:CURVES([[0., 0., 0.], [-.1006355412, -2.881824854, -0.]])

The ends of these lines (given by the second set of coordinates in the 'CURVES' formulae above represent the 'point' at which the final Auatom2 and 3 will lie. The

vector differences between these points and the origin (Auatom1) represent the new vectors for making up the plane in the final format. In other words, these are the new ahexAu and bhexAu in the final rotated system.

```
>ahexAufinal:=[-2.445415763, 1.528065363, 0.];

>bhexAufinal:=[-.1006355412, -2.881824854, -0.];
```

Any number of gold atoms can now be defined using these vectors, three examples are shown below

```
>Auatom1final:=sphere(o,rAu):

>Auatom2final:=sphere(ahexAufinal,rAu):

>Auatom4final:=sphere(ahexAufinal+bhexAufinal,rAu):
```

The gold surface is now completely done and attention is turned back to the Bi surface. The methodology for making the Bi surface is exactly the same as for the gold surface, however, locating the appropriate atoms on the 012 plane is a little more complex. The atoms that comprise a unit mesh that falls on the Bi(012) plane were worked out in a separate but similar program. Their coordinates are given below.

```
>Biatom9:=sphere((a+a)-(u*a+u*b+u*c),rBi):

>Biatom11:=sphere((a+b)-(u*a+u*b+u*c),rBi):

>Biatom2:=sphere((a)+(u*a+u*b+u*c),rBi):

>Biatom19:=sphere((a+a+c)-(u*a+u*b+u*c),rBi):

>Biatom18:=sphere((a+b+c)-(u*a+u*b+u*c),rBi):
```

An identical set of calculations is carried out as was shown with the gold atoms to rotate the coordinates of these atoms onto a plane parallel with the xy plane (now parallel with the modelled gold surface). As with the gold, the new coordinates of these atoms are used to determine unit mesh vectors for the Bi surface that can be used to plot out as many Bi atoms as desired. An example of three of these coordinates are shown below.

```
>Biatom5final:=sphere(transBiatom9+Bivecshort,rBi):

>Biatom6final:=sphere(transBiatom9-Bivecshort+Biveclong,rBi):

>Biatom7final:=sphere(transBiatom9+Bivecshort+Biveclong,rBi):
```

With both the bismuth and gold atoms defined, and in the correct orientation with each other based on the pole figure data, the final step is to define two surfaces and plot them. This plot then gives an exact account of the epitaxial relationship between electrodeposited Bi and the underlying Au(111) surface. Further manipulations to create other figures utilised the coordinates generated in Maple that were transposed into a graphics program.

```
>Bisurface:=display(Biatom1final,Biatom2final,Biatom3final,Biatom4final,
 Biatom5final,Biatom6final,Biatom7final,Biatom8final,Biatom9final,Biatom10final,
 Biatom11final,Biatom12final,Biatom13final):
>Ausurfacenorot:=display(Auatom1final,Auatom2final,Auatom3final,Auatom4final,
 Auatom5final,Auatom6final,Auatom7final,Auatom8final,Auatom9final,Auatom10final,
 Auatom11final,Auatom12final,Auatom13final,Auatom14final,Auatom15final,
 Auatom16final,Auatom17final,Auatom18final,Auatom19final,Auatom20final,
 Auatom21final):
>display(Bisurface,onesetrotatenormalsBi,Biunitmeshoutline,
 rotatenormalsAufinal,Ausurfacenorot,orientation=[0,0]); (Shown in Fig. A.5).
```

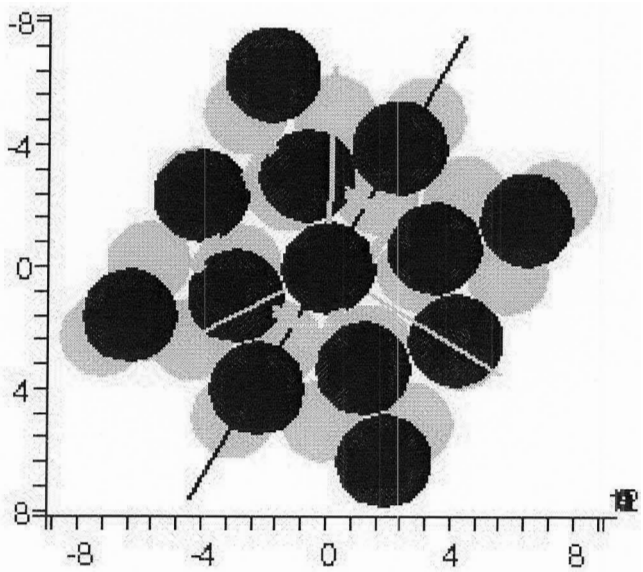

Figure A.5: Epitaxial arrangement of the Bi(012) plane on Au(111) as determined through X-ray pole figure analysis and Maple software modeling. Axes in Å.

References

[1] C. A. Jeffrey, D. A. Harrington, S. Morin, Surface Science 512 (2002) L367.

[2] C. A. Jeffrey, W. M. Storr, D. A. Harrington, Journal of Electroanalytical Chemistry 569 (2004) 61.

[3] K. Engelsman, W. J. Lorenz, E. Schmidt, Journal of Electroanalytical Chemistry 114 (1980) 1.

[4] J. Clavilier, R. Faure, G. Guinet, R. Durand, Journal of Electroanalytical Chemistry 107 (1980) 205.

[5] R. Wyckoff, Crystal Structures, 2nd Edition, Vol. 1, Interscience, New York, 1963, p. 32.

[6] G. Jerkiewicz, G. Vatankhah, A. Zolfaghari, J. Lessard, Electrochemical Communications 1 (1999) 1295.

[7] G. Sauerbrey, Zeitschrift fur Physik 155 (1959) 206.

[8] D. A. Buttry, in: H. Abruña (Ed.), Electrochemical Interfaces, VCH, New York, 1991, p. 531.

[9] J. H. Mangez, J. P. Issi, J. Heremans, Physical Review B 14 (1976) 4381.

[10] F. Y. Yang, G. J. Strijkers, K. Hong, D. H. Reich, P. C. Searson, C. L. Chien, Journal of Applied Physics 89 (2001) 7206.

[11] K. Hong, F. Y. Yang, K. Liu, D. H. Reich, P. C. Searson, C. L. Chien, F. F. Balakirev, G. S. Boebinger, Journal of Applied Physics 85 (1999) 6184.

[12] F. Y. Yang, K. Liu, C. L.Chien, P. C. Searson, Physical Review Letters 82 (1999) 3328.

[13] J. P. Ziegler, Solar Energy Materials 56 (1999) 477.

[14] E. W. Bohannan, C. C. Jaynes, M. G. Shumsky, J. K. Barton, J. A. Switzer, Solid State Ionics 131 (2000) 97.

[15] M. Metikos-Hukovic, Electrochimica Acta 26 (1981) 989.

[16] P. M. Vereecken, S. Ren, L. Sun, P. C. Searson, Journal of the Electrochemical Society 150 (2003) C131.

[17] F. Besse, C. Boulanger, J. M. Lecuire, Journal of Applied Electrochemistry 30 (2000) 385.

[18] P. Magri, C. Boulanger, J. M. Lecuire, Journal of Materials Chemistry 6 (1996) 773.

[19] C.-H. Chen, A. A. Gewirth, Journal of the American Chemical Society 114 (1992) 5439.

[20] C.-H. Chen, K. D. Kepler, A. A. Gewirth, B. M. Ocko, J. Wang, Journal of Physical Chemistry 97 (1993) 7290.

[21] K. Tamura, B. M. Ocko, J. X. Wang, R. R. Adzic, Journal of Physical Chemistry B 106 (2002) 3896.

[22] J. W. Schultze, D. Dickertmann, Surface Science 54 (1976) 489.

[23] J. W. Schultze, K. J. Vetter, Journal of Electroanalytical Chemistry 44 (1973) 63.

[24] R. R. Adzic, V. Jovancicevic, M. Podlavicky, Electrochimica Acta 25 (1980) 1143.

[25] J. P. Ganon, J. Clavilier, Surface Science 145 (1984) 487.

[26] B. K. Niece, A. A. Gewirth, Langmuir 12 (1996) 4909.

[27] M. R. Deakin, O. Melroy, Journal of Electroanalytical Chemistry 239 (1988) 321.

[28] J. Clavilier, J. M. Feliu, A. Aldaz, Journal of Electroanalytical Chemistry 243 (1988) 419.

[29] R. W. Evans, G. A. Attard, Journal of Electroanalytical Chemistry 345 (1993) 337.

[30] S. P. E. Smith, K. F. Ben-Dor, H. D. Abruña, Langmuir 16 (2000) 787.

[31] T. J. Schmidt, R. J. Behm, B. N. Grgur, N. M. Markovic, P. N. R. Jr, Langmuir 16 (2000) 8159.

[32] M. D. Macià, E. Herrero, J. M. Feliu, A. Aldaz, Journal of Electroanalytical Chemistry 500 (2001) 498.

[33] J. Lee, J. Christoph, P. Strasser, M. Eiswirth, G. Ertl, Journal of Chemical Physics 115 (2001) 1485.

[34] R. Gomez, A. Fernandez-Vega, J. M. Feliu, A. Aldaz, Journal of Physical Chemistry 97 (1993) 4769.

[35] S. M. Sayed, K. Juttner, Electrochimica Acta 28 (1983) 1635.

[36] S. P. E. Smith, H. A. Abruna, Journal of Physical Chemistry B 103 (1999) 6764.

[37] S. P. E. Smith, H. A. Abruna, Journal of Physical Chemistry B 102 (1998) 3506.

[38] N. J. Tao, S. M. Lindsay, Surface Science 274 (1992) L546.

[39] D. M. Kolb, Progress in Surface Science 51 (1996) 109.

[40] F. Möller, O. M. Magnussen, R. J. Behm, Physical Review Letters 77 (1996) 3165.

[41] K. Liu, C. L. Chien, P. C. Searson, Physical Review B 58 (1998) R14681.

[42] C. L. Chien, F. Y. Yang, K. Liu, D. H. Reich, P. C. Searson, Journal of Applied Physics 87 (2000) 4659.

[43] F. Y. Yang, K. Liu, K. Hong, D. H. Reich, P. C. Searson, C. L. Chien, Science 284 (1999) 1335.

[44] C. G. Jin, G. W. Jiang, W. F. Liu, W. L. Cai, L. Z. Yao, Z. Yao, X. G. Li, Journal of Materials Chemistry 13 (2003) 1743.

[45] M. A. Elmorsi, K. Juettner, Electrochimica Acta 31 (1986) 211.

[46] P. M. Vereecken, L. Sun, P. C. Searson, M. Tanase, D. H. Reich, C. L. Chien, Journal of Applied Physics 88 (2000) 6529.

[47] J. A. Switzer, H. M. Kothari, P. Poizot, S. Nakanishi, E. W. Bohannan, Nature 425 (2003) 490.

[48] H. M. Kothari, A. A.Vertegel, E. W. Bohannan, Chemistry of Materials 14 (2002) 2750.

[49] M. P. Nikiforov, A. A. Vertegel, M. G. Shumsky, J. A. Switzer, Advanced Materials 12 (2000) 1351.

[50] J. K. Barton, A. A. Vertegel, E. W. Bohannan, J. A. Switzer, Chemistry of Materials 13 (2001) 952.

[51] T. Hahn (Ed.), International Tables for Crystallography, Vol. 4, D. Reidel Pub. Co., Boston, 1983, p. 79.

[52] M. Hepel, in: A. Wieckowski (Ed.), Interfacial Electrochemistry, Marcel Dekker, New York, 1999, p. 599.

[53] S. Bruckenstein, M. Shay, Electrochimica Acta 30 (1985) 1295.

[54] G. Zilberman, V. Tsionsky, E. Gileadi, Electrochimica Acta 45 (2000) 3473.

[55] V. Tsionsky, L. Daikhin, G. Zilberman, E. Gileadi, Faraday Discussions 107 (1997) 337.

[56] V. Daujotis, E. Gaidamauskas, Journal of Electroanalytical Chemistry 446 (1998) 151.

[57] M. C. Santos, D. W. Miwa, S. A. S. Machado, Electrochemical Communications 2 (2000) 692.

[58] C. Gabrielli, M. Keddam, R. Torresi, Journal of the Electrochemical Society 138 (1991) 2657.

[59] M. Urbakh, L. Daikhin, Langmuir 10 (1994) 2836.

[60] M. Urbakh, L. Daikhin, Physical Review B 49 (1994) 4866.

[61] E. Gileadi, V. Tsionsky, Journal of the Electrochemical Society 147 (2000) 567.

[62] A. Bund, G. Schwitzgebel, Electrochimica Acta 45 (2000) 3703.

[63] G. Vatankhah, J. Lessard, G. Jerkiewicz, A. Zolfaghari, B. E. Conway, Electrochimica Acta 48 (2003) 1613.

[64] A. T. Hubbard, J. L. Stickney, S. D. Rosasco, M. P. Soriaga, D. Song, Journal of Electroanalytical Chemistry 150 (1983) 165.

[65] J. L. Stickney, S. D. Rosasco, D. Song, M. P. Soriaga, A. T. Hubbard, Surface Science 130 (1983) 326.

[66] M. Labayen, D. A. Harrington, M. Saidy, K. A. R. Mitchell, Surface Science 490 (2001) 256.

[67] T. Solomun, B. C. Schardt, S. D. Rosasco, A. Wieckowski, J. L. Stickney, A. T. Hubbard, Journal of Electroanalytical Chemistry 176 (1984) 309.

[68] M. Labayen, E. Herrero, J. M. Feliu, D. A. Harrington, Journal of Electroanalytical Chemistry 488 (2000) 32.

[69] J. L. Stickney, S. D. Rosasco, B. C. Schardt, A. T. Hubbard, Journal of Physical Chemistry 88 (1984) 251.

[70] J. L. Stickney, S. D. Rosasco, A. T. Hubbard, Journal of the Electrochemical Society 131 (1984) 260.

[71] J. Inukai, Y. Osawa, M. Wakisaka, K. Sashikata, Y. G. Kim, K. Itaya, Journal of Physical Chemistry B 102 (1998) 3498.

[72] J. H. White, H. D. Abruña, Journal of Electroanalytical Chemistry 274 (1989) 185.

[73] G. M. Bommarito, D. Acevedo, J. F. Rodriguez, H. D. Abruña, Journal of Electroanalytical Chemistry 379 (1994) 135.

[74] H. Baltruschat, U. Bringemeier, R. Vogel, Faraday Discussions 94 (1992) 317.

[75] M. E. Martins, R. C. Salvarezza, J. M. Vara, A. J. Arvia, Journal of the Electrochemical Society 138 (1991) 2509.

[76] V. I. Birss, M. Chang, J. Segal, Journal of Electroanalytical Chemistry 355 (1993) 181.

[77] M. Yang, M. Thompson, W. C. Duncan-Hewitt, Langmuir 9 (1993) 802.

[78] R. Schumacher, G. Borges, K. K. Kanazawa, Surface Science 163 (1985) L621.

[79] N. M. Markovic, H. A. Gasteiger, P. N. Ross, Langmuir 11 (1995) 4098.

[80] G. W. Anderson, M. C. Hanf, P. R. Norton, Physical Review Letters 74 (1995) 2764.

[81] K. Itaya, S. Sugawara, K. Sashikata, Journal of Vacuum Science and Technology A 8 (1990) 515.

[82] K. Sashikata, N. Furuya, K. Itaya, Journal of Vacuum Science and Technology B 9 (1991) 457.

[83] P. A. Thiel, T. E. Madey, Surface Science Reports 7 (1987) 211.

[84] K. Shimazu, H. Kita, Journal of Electroanalytical Chemistry 341 (1992) 361.

[85] H. Ibach, S. Lehwald, Surface Science 91 (1980) 187.

[86] G. B. Fisher, J. L. Gland, Surface Science 94 (1980) 446.

[87] M. Klaua, T. E. Madey, Surface Science 136 (1984) L42.

[88] K. Bange, T. E. Madey, J. K. Sass, E. M. Stuve, Surface Science 183 (1987) 334.

[89] J. N. Glosli, M. R. Philpott, Journal of Physical Chemistry 98 (1993) 9995.

[90] F. M. Al-Faqeer, K. G. Weil, H. W. Pickering, Electrochimica Acta 48 (2003) 1331.

[91] A. T. Hubbard, Chemical Reviews 88 (1998) 633.

[92] X. Gao, M. J. Weaver, Journal of the American Chemical Society 114 (1992) 8544.

[93] C. C. Chang, S. L. Yau, J. W. Tu, J. S. Yang, Surface Science 523 (2003) 59.

[94] K. Ueno, M. Seo, Journal of the Electrochemical Society 146 (1999) 1496.

[95] A. Chen, Z. Shi, D. Bizzotto, J. Lipkowski, B. Pettinger, C. Bilger, Journal of Electroanalytical Chemistry 467 (1999) 342.

[96] K. Arai, F. Kusu, K. Ohe, K. Takamura, Electrochimica Acta 42 (1997) 2493.

[97] M. A. Tadayyoni, P. Gao, M. J. Weaver, Journal of Electroanalytical Chemistry 198 (1986) 125.

[98] P. H. Qi, J. B. Hiskey, Hydrometallurgy 32 (1993) 161.

[99] B. G. Bravo, S. L. Michelhaugh, M. P. Soriaga, I. Villegas, D. W. Suggs, J. L. Stickney, Journal of Physical Chemistry 95 (1991) 5245.

[100] D. G. Frank, N. Batina, T. Golden, F. Lu, A. T. Hubbard, Science 247 (1990) 182.

[101] Z. L. Li, Z. J. Niu, T. H. Wu, H. D. Nie, X. M. Xiao, Electrochemical Communications 5 (2003) 297.

[102] F. Galliano, C. O. A. Olsson, D. Landolt, Journal of the Electrochemical Society 150 (2003) B504.

[103] M. R. Deakin, T. T. Li, O. R. Melroy, Journal of Electroanalytical Chemistry 243 (1988) 343.

[104] H. W. Lei, H. Uchida, M. Watanabe, Journal of Electroanalytical Chemistry 413 (1996) 131.

[105] T. Nomura, T. Mimatsu, Analytica Chimica Acta 143 (1982) 237.

[106] Z. X. Shu, S. Bruckenstein, Journal of Electroanalytical Chemistry 317 (1991) 263.

[107] F. C. Anson, Journal of the American Chemical Society 81 (1959) 1554.

[108] B. R. Wels, D. S. Austin-Harrison, D. C. Johnson, Langmuir 7 (1991) 559.

[109] N. Gu, L. Niu, S. Dong, Electrochemical Communications 2 (2000) 48.

[110] Q. Luo, Langmuir 16 (2000) 5154.

[111] Z. L. Li, B. Ren, X. M. Xiao, Y. Zeng, X. Chu, Z. Q. Tian, Journal of Physical Chemistry A 106 (2002) 6570.

[112] CRC Handbook of Chemistry and Physics, CRC Press, Boca Raton, Florida, 2003.

[113] L. Muller, Journal of Electroanalytical Chemistry and Interfacial Electrochemistry 16 (1968) 67.

[114] R. P. Akkermans, Q. Fulian, S. L. Roberts, M. F. Suárez, R. G. Compton, Journal of Physical Chemistry B 103 (1999) 8319.

[115] Z. Jusys, S. Bruckenstein, Electrochemical Communications 2 (2000) 412.

[116] D. C. Johnson, Journal of the Electrochemical Society 119 (1972) 331.

[117] B. I. Podlovchenko, E. A. Kolyadko, Russian Journal of Electrochemistry 36 (2000) 1268.

[118] F. A. Cotton, G. Wilkinson, Advance Inorganic Chemistry, 4th Edition, Wiley Interscience, New York, New York, 1980, p. 558.

[119] G. Chumanov, M. S. Sibbald, T. M. Cotton, Journal of Physical Chemistry B 102 (1998) 10836.

[120] J. Yahalom, O. Zadok, Journal of Materials Science 22 (1987) 499.

[121] J. Yahalom, D. F. Tessier, R. S. Timsit, A. M. Rosenfeld, D. F. Mitchell, P. T. Robinson, Journal of Materials Research 4 (1989) 755.

[122] A. S. M. A. Haseeb, J. P. Celis, J. R. Roos, Journal of the Electrochemical Society 141 (1994) 230.

[123] C. C. Yang, H. K. Cheh, Journal of the Electrochemical Society 142 (1995) 3040.

[124] T. P. Moffat, Journal of the Electrochemical Society 142 (1995) 3767.

[125] A. R. Despic, V. D. Jovic, Journal of the Electrochemical Society 134 (1987) 3004.

[126] D. M. Tench, J. T. White, Journal of the Electrochemical Society 139 (1992) 443.

[127] D. S. Lashmore, M. P. Dariel, Journal of the Electrochemical Society 135 (1988) 1218.

[128] R. Intrater, J. Yahalom, Journal of Materials Science Letters 12 (1993) 1549.

[129] Y. Jyoko, S. Kashiwabara, Y. Hayashi, Journal of the Electrochemical Society 144 (1997) L5.

[130] J. L. Stickney, in: Electroanalytical Chemistry, Vol. 21, Marcel Dekker, London, 1999, p. 75.

[131] G. Hodes, J. Manassen, D. Cahen, Nature 261 (1976) 403.

[132] M. P. R. Panicker, M. Knaster, F. A. Kroger, Journal of the Electrochemical Society 125 (1978) 566.

[133] F. A. Kroger, Journal of the Electrochemical Society 125 (1978) 2028.

[134] G. Mengoli, M. M. Musiani, F. Paolucci, M. Gazzano, Journal of Applied Electrochemistry 21 (1991) 863.

[135] J. Ortega, J. Herrero, Journal of the Electrochemical Society 136 (1989) 3388.

[136] S. Massaccesi, S. Sanchez, J. Vedel, Journal of Electroanalytical Chemistry 412 (1996) 95.

[137] C. Wei, J. Rajeshwar, Journal of the Electrochemical Society 139 (1992) L40.

[138] V. Krishnan, D. Ham, K. K. Mishra, K. Rajeshwar, Journal of the Electrochemical Society 139 (1992) 23.

[139] M. El-Kouedi, C. A. Foss, S. A. Bodolosky-Bettis, R. E. Bachman, Journal of Physical Chemistry B 106 (2002) 7205.

[140] J. A. Switzer, R. P. Raffaelle, R. J. Phillips, C. J. Hung, T. D. Golden, Science 258 (1992) 1918.

[141] J. A. Switzer, K. G. Sheppard, The Electrochemical Society: Interface 4 (1995) 26.

[142] J. A. Switzer, M. J. Shane, R. J. Phillips, Science 247 (1990) 444.

[143] J. A. Switzer, H. C. J, B. E. Breyfogle, M. G. Shumsky, R. V. Leeuwen, T. D. Golden, Science 264 (1994) 1573.

[144] T. L. Wade, R. Vaidyanathan, U. Happek, J. L. Stickney, Journal of Electroanalytical Chemistry 500 (2001) 322.

[145] E. W. Bohannan, L. Y. Huang, F. S. Miller, M. G. Shumsky, J. A. Switzer, Langmuir 15 (1999) 813.

[146] F. Cotton, G. Wilkinson, Advanced Inorganic Chemistry, 4th Edition, Wiley Interscience, New York, New York, 1980, p. 970.

[147] L. I. Berger, B. R. Pamplin, CRC Handbook of Chemistry and Physics, 84th Edition, CRC Press, Boca Raton, Florida, 2003.

[148] J. G. N. Matias, J. F. Juliano, D. M. Soares, A. Gorenstein, Journal of Electroanalytical Chemistry 431 (1997) 163.

[149] N. Myung, J. H. Jun, H. B. Ku, H. K. Chung, K. Rajeshwar, Microchemical Journal 62 (1999) 15.

[150] D. Sands, Vectors and Tensors in Crystallography, Addison-Wesley, Reading, Mass., 1982.